

Thomas Seefeld, Tim Radel, Thorsten Mattulat (Eds.)

**LAF 2022:
Proceedings of the
12th Laser Applications
Forum**

November 23-24, 2022
Congress Centrum Bremen



LAF 2022:
Proceedings of the 12th Laser Applications Forum
November 23-24, 2022
Congress Centrum Bremen

Thomas Seefeld, Tim Radel, Thorsten Mattulat (Eds.)

Strahltechnik, Band 76, BIAS Verlag, 2022

Editor of the series: Ralf B. Bergmann

ISBN: 978-3-933762-70-2

<https://doi.org/10.26092/elib/1884>

© 2022 The Authors. Published under responsibility of BIAS - Bremer Institut für angewandte Strahltechnik GmbH. This work is licensed under the Creative Commons Attribution International License (CC BY 4.0). <http://creativecommons.org/licenses/by/4.0>

Back... and better

12th Laser Applications Forum LAF 2022 with focus on hydrogen technology

BIAS' bi-annual Laser Applications Forum is back in its 12th edition, bringing together old friends and new mates from the laser community. As a platform for exchange between users, developers, service providers, manufacturers, and researchers, LAF aims to support and increase the transfer between academia and business, and in particular business-to-business. The forum's character is shaped not only by the accompanying exhibition and plenty of opportunities for communication and discussion, but also by the warm familiarity of the many participants, creating open and inspiring discussions while developing new ideas and impetuses to take home. We are more than happy that it is time again for face-to-face networking.

So, let's see what is new at LAF 2022.

There is a keynote session focusing on "laser-based solutions for the hydrogen economy", highlighting today's challenges on the way towards zero emission flight and green hydrogen production at industrial scale. Hydrogen technology is at our doorstep and the headline topic is reliable, affordable, and sustainable energy supply. In this respect, industrialization of hydrogen technology has become a key issue for the years to come. Here, of course, the laser steps in, paving the path by welding thousands of meters of tight seams, producing functional surfaces for chemical reactions, or printing complex parts or completely new materials that can store hydrogen. To develop suitable laser processes that enable upscaling of the hydrogen technology, BIAS made significant investments into novel laser-oriented hydrogen research infrastructure and this year's BIAS Open House event provides the opportunity to experience current R&D live in the lab and peer some of the unparalleled equipment of state-of-the-art laser sources, multi-scanner processing systems, high-speed sensing systems, a unique laser multi-materials deposition facility with integrated heat treatment and process monitoring possibilities, and much more.

The hydrogen focus adds perfectly to the sessions on laser beam welding, process monitoring, micro structuring, and additive manufacturing. Beam shaping, scanner-based technologies, and multi-sensor monitoring are among the upcoming technologies, and hands-on experience is presented by experts from industrial application. Current R&D at BIAS is highlighted in a special session at LAF and a collection of respective short papers from BIAS is published in this proceedings volume, freely available via open access.

Many thanks and a very warm welcome to all speakers, exhibitors, sponsors, and participants. We look forward to meeting you again after a long time, for networking, and for discussing and promoting laser-based innovations for future energy solutions and a better future!

Thomas Seefeld, Tim Radel and Thorsten Mattulat

Contents

Influence of powder feed parameters on the powder stream in laser metal deposition (LMD) by high-speed and high-resolution imaging <i>Annika Bohlen, Dieter Tyralla, Thomas Seefeld</i>	1
High-speed laser melt injection for wear protection of skin-pass rolls <i>Philipp Warneke, Philipp Hildinger, Annika Bohlen, Thomas Seefeld</i>	7
515 nm wavelength laser for laser melt injection of high-quality MMC in Cu-ETP <i>Anika Langebeck, Annika Bohlen</i>	11
Materials Characterization at High Strain Rates <i>Tobias Valentino, Eric A. Jäggle, Tim Radel</i>	15
Tensile strength of Nitinol flanges fabricated by laser rod end melting and immediate flange processing <i>Yang Lu, Tim Radel</i>	18
On the combination of plasma nitrided surfaces and LIPSS <i>Lewin Rathmann, Henning Hasselbruch, Andreas Mehner, Tim Radel</i>	23
Laser micro structuring of multi-layer coatings on aircraft splines for optimization of the surface properties <i>Andreas Stephen, Bastian Lenz, Gerrit Hellenbrand</i>	28
Influence of electrolyte concentration on laser chemical machining <i>Marcel Simons, Tim Radel</i>	32
Macro-pore free sub-surface PBF-LB/M components through laser polishing <i>L. Rathmann, L.H. Beste, P.J. Faue, B. Richter, K. Klingbeil, F.E. Pfefferkorn, T. Radel</i>	37
Hybrid additive manufacturing with titanium powder and aluminum substrates via laser powder bed fusion <i>Sven Müller, Thorsten Mattulat, Peer Woizeschke</i>	41
Prevention of coating-induced agglomerations within the weld seam during laser beam deep penetration welding of aluminum-silicon coated press-hardened steel <i>Marcel Möbus, Peer Woizeschke, Thorsten Mattulat</i>	47
Industrial applicability of reflection-assisted laser beam brazing of ZM-coated steel sheets <i>Insa Henze, Ronald Pordzik, Philip Marben, Thorsten Mattulat</i>	52
Introducing an algorithm for the automatic detection of interface positions for flange joints based on laser triangulation measurements <i>Ronald Pordzik, Thorsten Mattulat</i>	58

Influence of powder feed parameters on the powder stream in laser metal deposition (LMD) by high-speed and high-resolution imaging

Annika Bohlen*¹ , Dieter Tyralla¹ , Thomas Seefeld¹ 

¹ BIAS – Bremer Institut für angewandte Strahltechnik GmbH, Klagenfurter Straße 5, 28359 Bremen, Germany

Abstract

Laser metal deposition (LMD) is a blown powder process used for the additive manufacturing of large components or the generation of functional geometries on semi-finished parts. In LMD laser intensity and powder mass flow distribution within the process zone must be precisely matched for a welding bead of predefined shape and a consistent layer quality. Therefore, the present work analyses the powder stream of a single injector that is commonly used for discrete coaxial nozzles in LMD. Several powder size classes are investigated in a range of 45 μm and 106 μm . The influence of carrier gas flow rate and powder mass flow rate variations on powder stream characteristics like particle velocity and propagation were determined up to a distance of 10 mm from the nozzle by high-speed imaging at a frequency of 30 kHz with a high spatial resolution. It was found that particle velocity depends mainly on carrier gas flow rate and particle size. Additionally, the measurement shows that the divergence increases for higher distances and higher particle sizes.

Keywords: Laser Metal Deposition, Powder-Jet, High-Speed Imaging

1 Introduction

Additive manufacturing is a production technology with increasing importance for metallic component production. Not only prototypes can be additively built, also the number of additively built end products increases steadily. Laser metal deposition (LMD) utilizes blown powder, making it a freeform process. This brings advantages for the achievable size of components, compared to other laser additive processes. The achievable geometric resolution and build rate are highly dependent on the powder supply to the process zone. Due to the extensive developments in the past decades, numerous different system technologies for powder feeding and powder nozzles have been established on the market. In general, the powder feed systems are differentiated into lateral and coaxial systems.

The importance of the powder stream characteristics in LMD is already addressed in many studies. Prasad et al. showed that a powder stream that is well-focused to the melt pool does not only lead to a better catchment efficiency but can also lead to better geometrical tolerances [1]. A lower velocity of the particles, as well as lower particle size and higher bonding temperature are beneficial for a better catchment efficiency [2]. An increase in carrier gas flow rate leads to a higher divergence of the powder stream, as well as to a decrease of powder concentration [3]. Additionally, a high carrier gas flow rate can lead to an increased spatter generation during the deposition process [4]. Balu et al. showed that the density, shape, and diameter of powder particles play a key role for stable powder flows [5]. Smurov et al. investigated the influence of particle size on the divergence for annular gap nozzles. Their model shows a strong increase in divergence with a particle size increase from 20 μm to 80 μm [6].

Previous work took a detailed look at the influence of wall roughness on the simulation of particle propagation behavior [7], as well as at the powder propagation behavior on a macroscopic scale [8]. This paper presents a high-speed and high-resolution imaging technique to gain a detailed insight into powder stream be-

havior, with the ability to automatically trace thousands of particles and measure their velocity and divergence. Different particle fractions were examined to obtain a deeper understanding of the influence of particle size on the powder stream behavior.

2 Experimental

2.1 Material

Stainless steel 316L powder material was used with a powder size of 45 μm to 106 μm according to the manufacturer. The sieve analysis from the manufacturer can be found in Tab. 1. The powder was sieved before experiments using the following mesh sizes: 45 μm , 53 μm , 63 μm , 71 μm , 80 μm , 90 μm , 100 μm and 106 μm , resulting in nine different size fractions. Of the seven used fractions, a SEM picture was taken to evaluate fraction specific morphologies (see Fig. 1).

Tab. 1: Sieve analysis from powder manufacturer.

< 38 μm (%)	38 μm – 45 μm (%)	45 μm – 53 μm (%)	53 μm – 63 μm (%)	63 μm – 90 μm (%)	90 μm – 106 μm (%)	106 μm – 125 μm (%)	> 125 μm (%)
0.0	1.7	15.5	16.5	49.3	16.9	0.1	0.0

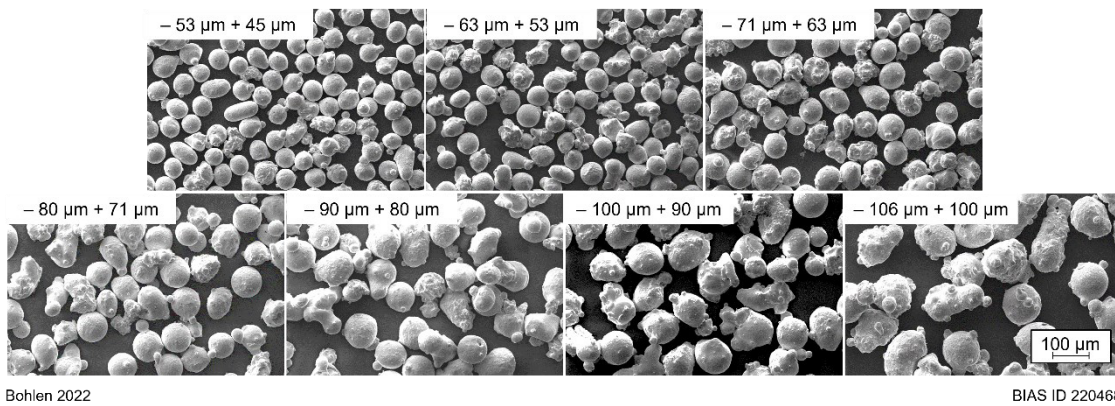
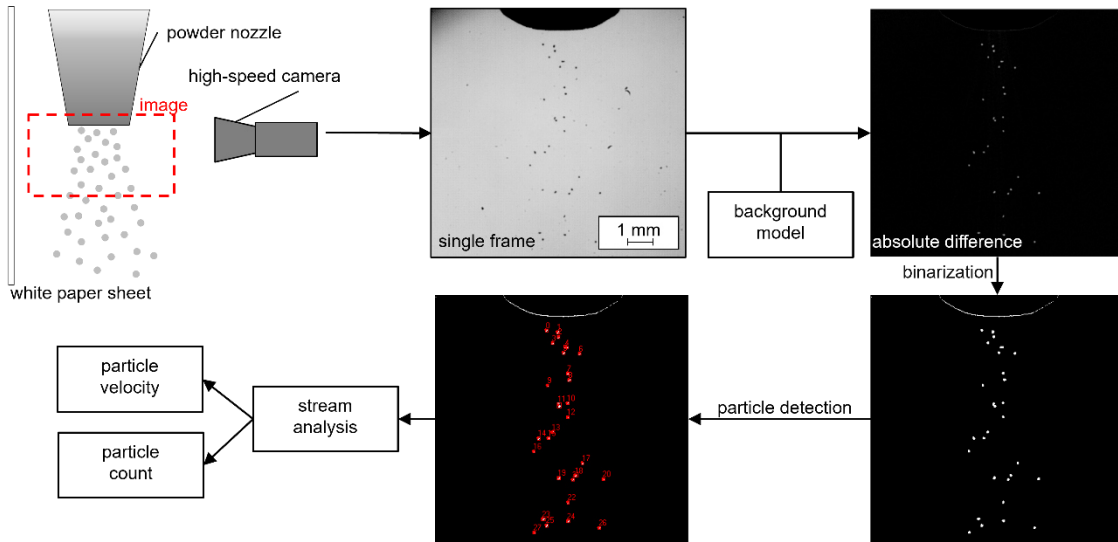


Fig. 1: SEM images of each sieved powder fraction.

2.2 Setup and Analysis Method

A powder feeder from Oerlikon Metco (type TWIN-150) was used. The powder was fed using Argon as carrier gas with variable gas flows. A single jet powder nozzle was used for these studies, which was vertically directed. The nozzle consists of a ceramic inner tube with a copper outer shielding. The opening has a diameter of 1.7 mm. The powder mass flow rate was varied between 1 g/min and 6 g/min with a constant carrier gas flow rate of 2.5 l/min. The carrier gas flow rate was varied between 1 l/min and 5 l/min with a constant powder mass flow rate of 3 g/min. A high-speed camera (Vision Phantom Research VEO410L) was used to observe the particle flow in combination with an illumination laser (Cavitar Cavilux HF). The illumination laser was directed at a white sheet of paper behind the powder flow to achieve a high contrast between powder particles and background, see Fig. 2.

All high-speed videos were recorded at 30 kHz with an image size of 384 px \times 376 px. One pixel width is equivalent to 26.27 μm . Each parameter set was recorded in at least 13,000 frames, this equals 433.3 ms. A LabView based program was used to analyze the obtained videos. From the first 5,000 frames a background model was created by calculating a mean frame. For each frame the background model was used to calculate the absolute difference. This image was then binarized and used for particle detection. Particles from each frame were then searched in the next frame. If they could be detected the distance between the particles in the frames was measured. Thus, particles were traced through multiple frames, making it possible to gain a mean velocity per particle and counting unique particles. See Fig. 2 for an exemplary analysis of one frame.



Bohlen 2022

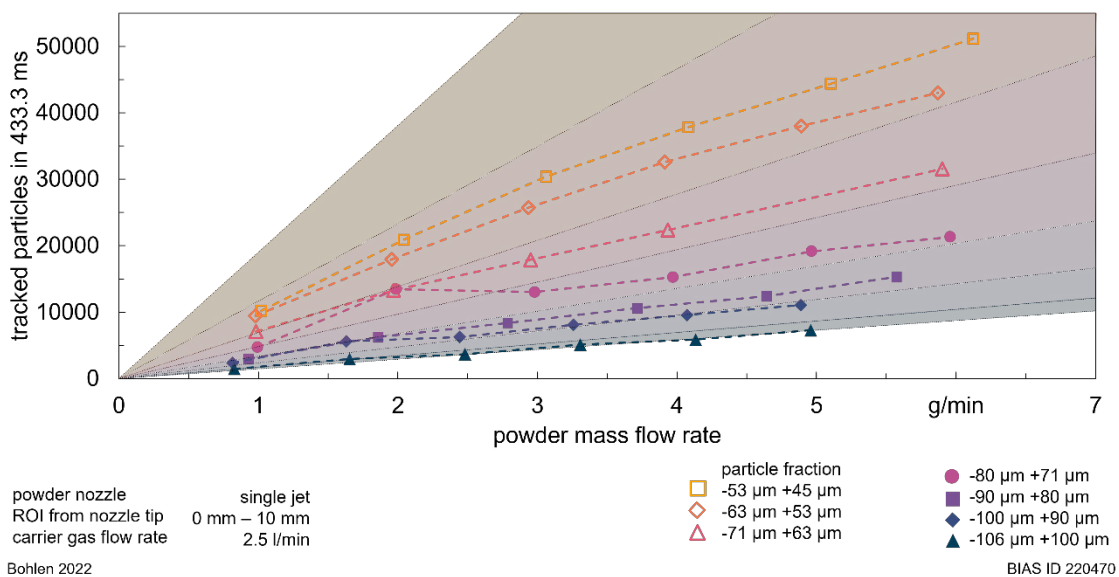
BIAS ID 220469

Fig. 2: Sketch of the experimental setup for high-speed imaging and exemplary analysis of one frame.

3 Results and Discussion

Fig. 3 shows the counted particles for the varied powder mass flow rate for each of the sieved particle fractions. The background coloration shows the theoretical number of particles for each fraction, calculated for ideal spheres, over a conveying time of 433.3 ms. The counted particles from the high-speed videos are in good accordance with the calculated amounts, except for the particle classes $45\ \mu\text{m} - 53\ \mu\text{m}$ and $100\ \mu\text{m} - 106\ \mu\text{m}$.

An explanation as to why the biggest fraction differs to calculated values can be found in the shape of the particles. Fig. 1 shows that the particles in the fraction from $100\ \mu\text{m}$ to $106\ \mu\text{m}$ show defects in respect to their shape being more elongated than in the other fractions. During sieving these elongated particles fit through meshes with their smaller side. This makes for bigger particles in this fraction and thus fewer particles. Smaller particles, on the other hand, appear lighter in the recordings. Due to this it could happen that not enough contrast is given to the background to safely track one particle through multiple consecutive frames.



Bohlen 2022

BIAS ID 220470

Fig. 3: Particles tracked in recordings for different powder mass flow rates.

Tracked particles for different carrier gas flow rates can be seen in Fig. 4. Overall, the particle fractions show an almost constant number of particles for different carrier gas flow rates. Exceptions are the values for the smallest amount of carrier gas (1 l/min) and for smaller particle fractions with higher carrier gas flow rates.

All particle fractions show a reduced number of particles with only 1 l/min carrier gas flow rate, this could be due to insufficient carrier gas flow. For the particle fractions $-106 \mu\text{m} +90 \mu\text{m}$ this carrier gas flow rate was not able to transport the particles. A reduced amount of smaller tracked particles ($-63 \mu\text{m} +45 \mu\text{m}$) for higher carrier gas flow rates can be traced back to the analysis method where particles need to be tracked through multiple consecutive frames to be taken into account.

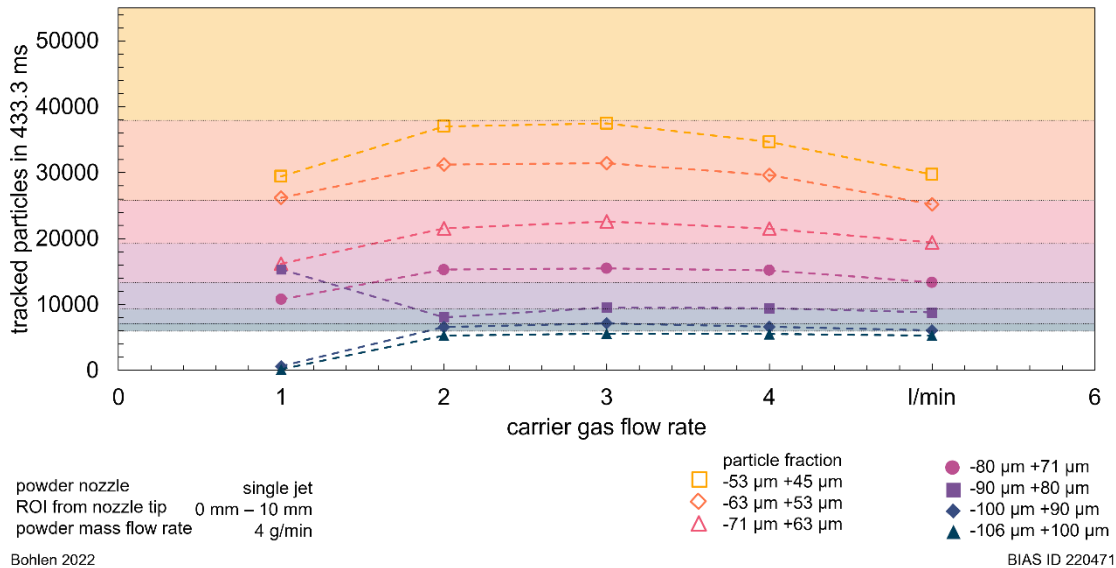


Fig. 4: Particles tracked in recordings for different carrier gas flow rates.

Calculated particle velocities for varied powder mass flow rates and varied carrier gas flow rates are shown in Fig. 5. The particle velocity remains nearly linear with an increase of powder mass flow rate. Smaller particles ($-63 \mu\text{m} +53 \mu\text{m}$) show a higher velocity than larger particles ($-106 \mu\text{m} +100 \mu\text{m}$). An increase in carrier gas flow rate leads to an increase in particle velocity for all particle fractions as well as for the as received powder ($-106 \mu\text{m} +45 \mu\text{m}$).

Since the amount of particles within the powder stream is very low [3] an increase in powder mass flow rate does not lead to collisions of particles which would slow them down, leading to constant particle velocities with increasing powder mass flow rates. With a constant tube diameter for the carrier gas an increase in flow rates leads to higher gas velocities and thus to higher particle velocities. Light particles will be more accelerated by the gas flow. For both, varied powder mass flow rate and carrier gas flow rate the velocities for the as received powder is close to the particle fraction $-80 \mu\text{m} +71 \mu\text{m}$. A possible reason for this is the high amount (49.3%) of particles in the as received powder in the range of $63 \mu\text{m} - 90 \mu\text{m}$.

The divergence angle (half angle with respect to center line) of the powder after the nozzle exit can be seen in Fig. 6. An increase in powder mass flow rate leads to a decrease of divergence for all particle fractions. Smaller particles lead to a smaller divergence. For an increase in carrier gas flow rate the divergence increases, again the divergence is smaller for smaller particles.

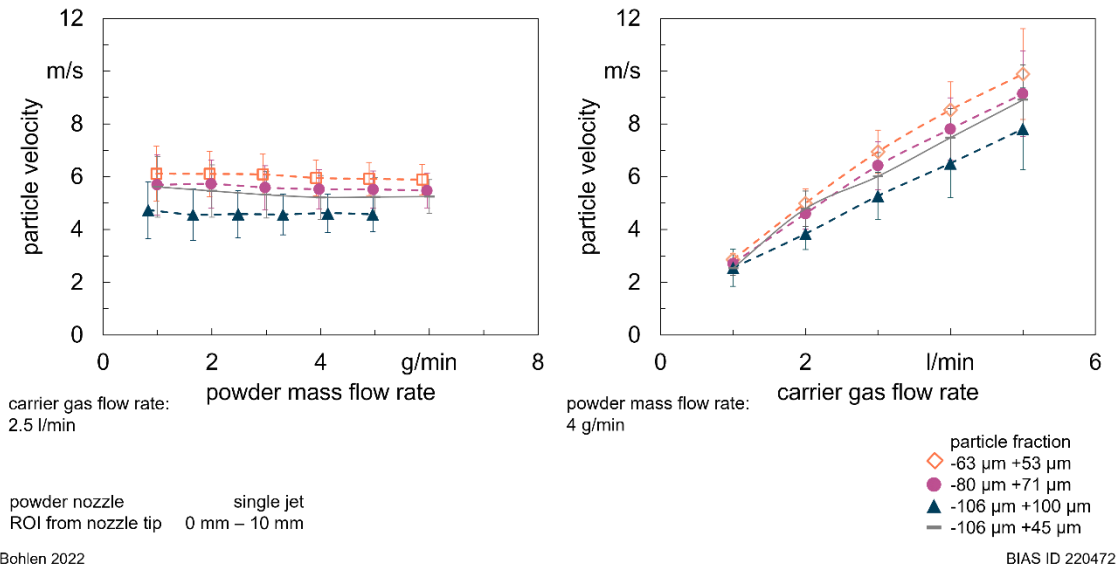


Fig. 5: Particle velocity for varied powder mass flow rate and varied carrier gas flow rates for selected particle fractions.

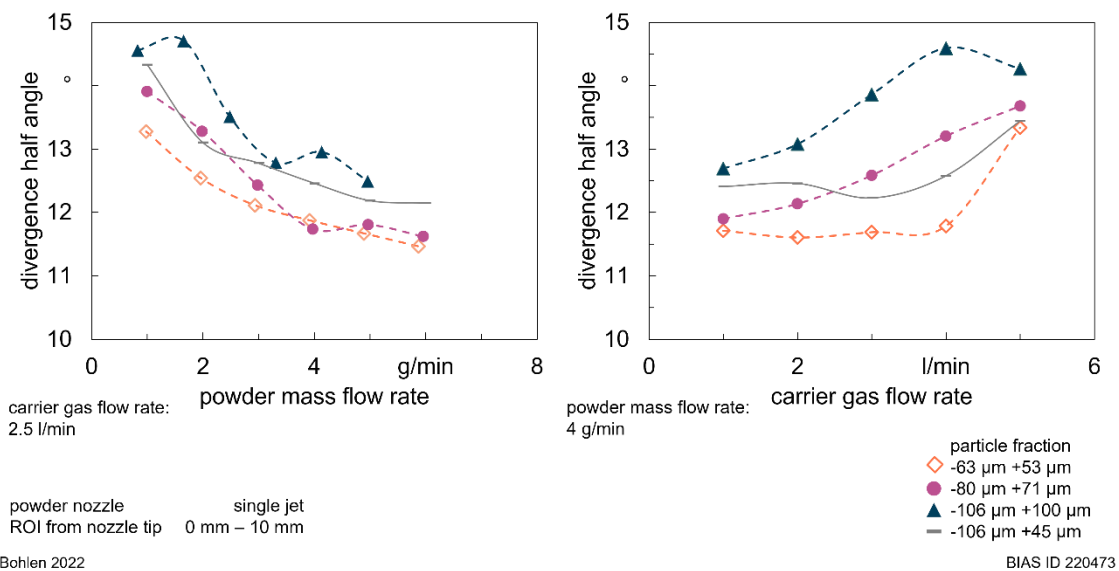


Fig. 6: Divergence angles (half angles with respect to center line) for varied powder mass flow rate and varied carrier gas flow rates for selected particle fractions.

4 Conclusion

High-speed and high-resolution imaging of the powder stream gives a detailed understanding of the influence parameters have on the powder stream. This is crucial to further improve laser metal deposition in regard to geometrical accuracy as well as improving the material utilization, making the process more economical. It is not only possible to measure the particles velocities and powder divergence but also to count single particles and tracking them through multiple frames.

Smaller particle fractions lead to an overall smaller divergence and higher particle velocities for all parameter variations.

Acknowledgements

Funded by the Deutsche Forschungsgemeinschaft (DFG, German Research Foundation) – project number 424886092 (Adaptive powder nozzle for additive manufacturing processes).

References

- [1] H. Siva Prasad, F. Brueckner, A.F.H. Kaplan: Powder catchment in laser metal deposition. *Journal of Laser Applications*, 31 (2) (2019) 22308.
- [2] J. Lin: A simple model of powder catchment in coaxial laser cladding. *Optics & Laser Technology*, 31 (3) (1999) 233–238.

- [3] H. Tan, F. Zhang, R. Wen, J. Chen, W. Huang: Experiment study of powder flow feed behavior of laser solid forming. *Optics and Lasers in Engineering*, 50 (3) (2012) 391–398.
- [4] S. Takemura, R. Koike, Y. Kakinuma, Y. Sato, Y. Oda: Design of powder nozzle for high resource efficiency in directed energy deposition based on computational fluid dynamics simulation. *Int J Adv Manuf Technol*, 105 (10) (2019) 4107–4121.
- [5] P. Balu, P. Leggett, R. Kovacevic: Parametric study on a coaxial multi-material powder flow in laser-based powder deposition process. *Journal of Materials Processing Technology*, 212 (7) (2012) 1598–1610.
- [6] I. Smurov, M. Doubenskaia, A. Zaitsev: Comprehensive analysis of laser cladding by means of optical diagnostics and numerical simulation. *Surface and Coatings Technology*, 220 (2013) 112–121.
- [7] A. Haghshenas, A. Bohlen, D. Tyralla, R. Groll: The relevance of wall roughness modeling for simulation of powder flows in laser metal deposition nozzles. *Int J Adv Manuf Technol* (2022).
- [8] A. Bohlen, T. Seefeld, A. Haghshenas, R. Groll: Characterization of the powder stream propagation behavior of a discrete coaxial nozzle for laser metal deposition. *J. Laser Appl.*, 34 (2022). (in print)

High-speed laser melt injection for wear protection of skin-pass rolls

Philipp Warneke*¹ , Philipp Hildinger¹ , Annika Bohlen¹ , Thomas Seefeld¹ 

¹ BIAS – Bremer Institut für angewandte Strahltechnik GmbH, Klagenfurter Straße 5, 28359 Bremen, Germany

Abstract

Laser melt injection (LMI) is a technology for producing metal matrix composite (MMC) layers on tools such as skin-pass rolls by injecting hard particles into a laser-induced weld pool. However, low process speeds prevent the application of laser melt injection on a large scale. To overcome this drawback, a new approach is presented: High-speed laser melt injection (HSLMI) is a promising method for generating highly wear-resistant MMC-layers on tools with high productivity.

For the first time, high process speeds of up to 100 m/min were reached with HSLMI of spherical fused tungsten carbide (SFTC) particles into the steel 1.2362 that is used for skin-pass rolls. It was found that both the crack susceptibility and the SFTC dissolution can be reduced significantly by increasing the process speed.

The wear behavior of the MMC layers was studied in a pin-on-plate test. It was found that the SFTC reinforcement leads to a significant improvement in wear resistance over the non-reinforced steel substrate. The wear volume was reduced from 3.6 mm³ to 0.1 mm³ to 0.3 mm³ by an SFTC particle-reinforcement.

Keywords: laser melt injection, metal matrix composite, wear protection

1 Introduction

Skin-pass rolling is the last process in a rolling line. In this process, the final sheet thickness and the surface properties are set. For improving the formability and the paint adhesion of rolled sheets, specific textures are formed into the sheets by textured skin-pass rolls [1]. Until now, there are at least six different technologies for texturing skin-pass rolls that can be divided into stochastic and deterministic technologies according to the resulting texture. Stochastic textures can be generated by shot blast texturing, electro discharge texturing and precision texturing [2]. Shot blast texturing and electro discharge texturing roughen the roll surface. In precision texturing, a chromium-based coating with spherical nubs is applied. Deterministic textures can be generated by laser texturing or electron beam texturing. With these technologies, usually, small craters are created by local melting of the roll surface. Another way of laser texturing is the generation of implants with titanium diboride [3]. Each implant is generated by laser melt injection (LMI) using titanium diboride powder with an average powder diameter of 4 µm as hard material. This two-step process consists of pre-depositing the titanium diboride powder with an organic binder and the laser-induced implantation. However, the deterministic generation of implants with LMI is a time-consuming process.

Therefore, high-speed laser melt injection (HSLMI) for generating near-net shape metal matrix composite (MMC) layers on rolls with high productivity has been developed. In this one-step process, wear-resistant MMC layers featuring a stochastic texture can be generated. Spherical fused tungsten carbide (SFTC) particles are injected into a 1.2362 substrate. In previous research, it was shown that an SFTC reinforcement reduces the wear of copper pistons by 69 % to 75 % [4]. Fig. 1 shows a schematic diagram of HSLMI. Experiments showed that a high SFTC particle velocity, which can be adjusted via the volume flow rate of the

powder feeding gas, is a key factor for enabling high process speeds. For HSLMI, laser powers of up to 10 kW and a volume flow rate of the powder feeding gas of 15 l/min are used.

2 Methods

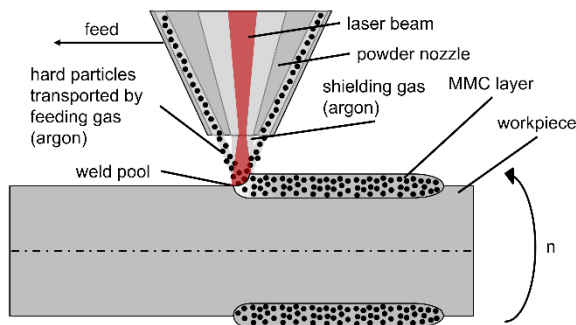
Characteristics of the MMC layer such as the layer thickness, the SFTC particle content and defects such as the porosity and the cumulated crack length were investigated as a function of the process speed. For this, a series of LMI experiments was carried out with a constant laser power of 6.7 kW and a constant powder feed rate of 90 g/min. The only varied parameter was the process speed. The MMC layer thickness, the SFTC particle content, the porosity and the cumulated crack length were measured on light microscope images of cross sections of the MMC layers. The cumulated crack length is the sum of all individual crack lengths within a region of interest (ROI) of 2 mm². Only cracks within the 1.2362 matrix were considered. For determining the wear resistance, sliding wear tests with MMC samples featuring a cylindrical surface were carried out. Pins made of 1.3505 with a spherical cap were used as counter bodies. For each test, a test force of 30 N was applied for four hours.

3 Results and Discussion

The process speed of LMI could be increased up to 70 m/min with a laser power of 6.7 kW. For reaching higher process speeds of up to 100 m/min, the laser power needed to be increased to 10 kW. A process speed of 100 m/min corresponds to a processed area per unit time of 1000 cm²/min. With HSLMI, near-net shape MMC layers featuring a small layer thickness and a small waviness can be generated, see Fig. 2. This reduces the effort for final machining of SFTC reinforced parts significantly. Due to a high difference in hardness between the SFTC particles and the 1.2362 matrix, the final machining is challenging and expensive. The interface between the SFTC particles and the 1.2362 matrix shows a good metallurgical bonding. Only a few particle deformations were detected. Furthermore, cracks within the 1.2362 matrix were detected that also run through SFTC particles. The cracks are mainly oriented vertically to the surface of the MMC layer.

The layer thickness and the SFTC particle content depending on the process speed are shown in Fig. 3. The layer thickness decreases degressively with increasing process speed from 1 mm at a process speed of 10 m/min to 0.1 mm at a process speed of 70 m/min. The SFTC particle content scatters between 14 vol% and 30 vol% with no clear correlation to the process speed. For explaining the degressive decrease of the layer thickness, two opposite influences need to be considered. On the one hand, the energy per unit length decreases with the process speed which has a reducing effect on the layer thickness. On the other hand, the process efficiency increases with the process speed since the thermal losses are reduced which has an increasing effect on the layer thickness [5].

Another advantage of HSLMI is the significant reduction of the cumulated crack length and the porosity. At high process speeds, a low energy per unit length leads to a reduction of the heat input and accordingly to temperature-related defects. Cracks and pores were detected at all investigated process speeds. However, both the porosity and the cumulated crack length decrease degressively with increasing process speed, see Fig. 4. The porosity can be reduced from 6 vol% to 1 vol% and the cumulated crack length from 6 mm to



Warneke 2022

BIAS ID 220456 Warneke 2022

Fig. 1: Schematic diagram of HSLMI.

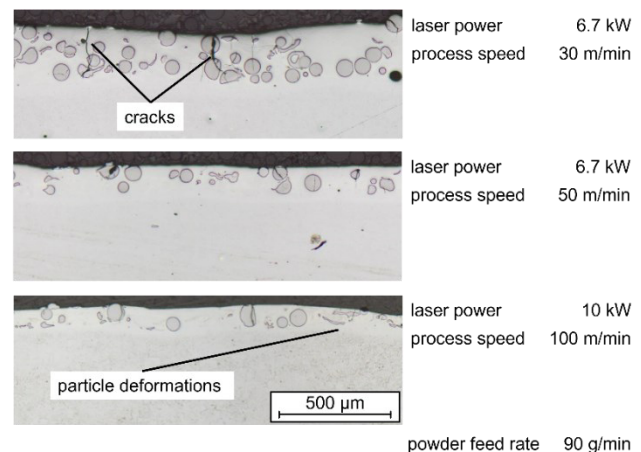
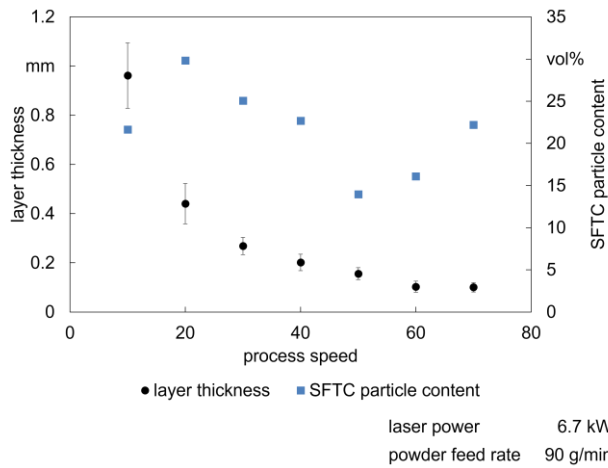
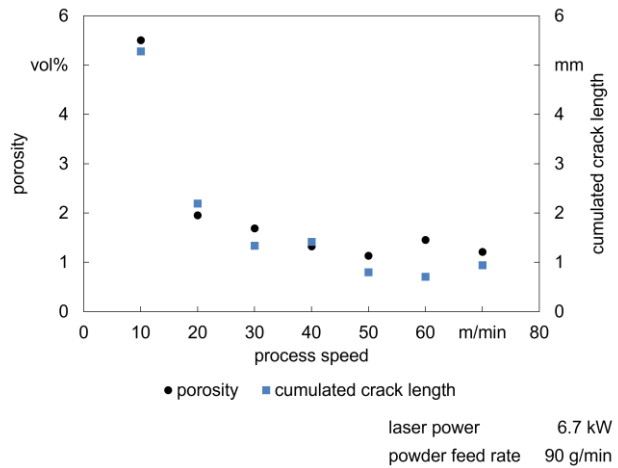


Fig. 2: Cross sections of SFTC particle reinforced 1.2362 obtained by HSLMI.



Warneke 2022

BIAS ID 220262 Warneke 2022



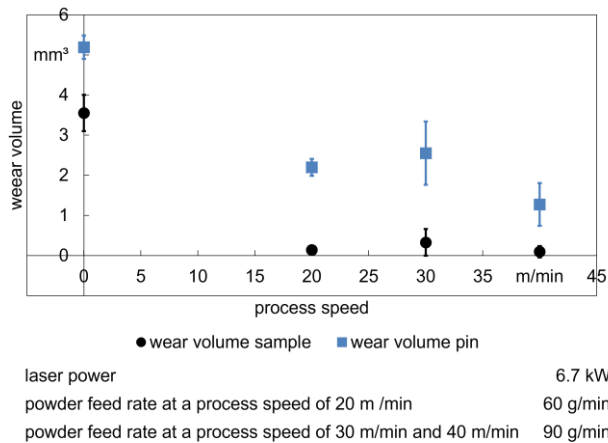
BIAS ID 220265

Fig. 3: MMC layer thickness and SFTC particle content as a function of the process speed.

Fig. 4: Porosity and cumulated crack length as a function of the process speed.

1 mm by increasing the process speed from 10 m/min to 70 m/min. At a process speed of 10 m/min, the porosity and the cumulated crack length are significantly higher than at higher process speeds.

For determining the wear resistance of the MMC layers, sliding wear tests were carried out. Fig. 5 shows the wear volume of non-reinforced and SFTC particle reinforced samples generated at different process speeds and the wear volume of the corresponding pins. The SFTC reinforcement of the samples lead to a reduction in wear volume from 3.6 mm³ to 0.1 mm³ to 0.3 mm³. The pins wore out stronger than the samples in all four configurations.



Warneke 2022

BIAS ID 220269

Fig. 5: Wear volume of non-reinforced 1.2362 (process speed = 0 m/min) and wear volume of SFTC reinforced 1.2362 as a function of the process speed.

4 Conclusions

HSLMI has been introduced. With HSLMI, process speeds of up to 100 m/min can be reached.

The process speed has a major influence on the MMC microstructure. The cumulated crack length and the porosity within the 1.2362 matrix decrease when increasing the process speed.

By reinforcing the steel 1.2362 with SFTC particles by HSLMI, the wear resistance is improved significantly. However, the influence of the process speed on the MMC microstructure has no decisive impact on the wear resistance.

Acknowledgements

The authors gratefully acknowledge the support of this work by Deutsche Forschungsgemeinschaft (DFG) within the project 424737129.

References

- [1] K. Hilgenberg, K. Steinhoff: Texturing of skin-pass rolls by pulsed laser dispersing. *Journal of Materials Processing Technology* 225 (2015) 84–92. <https://doi.org/10.1016/j.jmatprotec.2015.05.027>
- [2] F. Klocke: *Fertigungsverfahren 4* (2017) Springer Berlin Heidelberg. <https://doi.org/10.1007/978-3-662-54714-4>
- [3] K. Hilgenberg: Investigation of the self-organising behaviour of laser implanted tool surfaces (2014) Dissertation. Universität Kassel, Germany.
- [4] P. Warneke, A. Bohlen, T. Seefeld: Improving the wear resistance of copper tools for pressure die casting by laser melt injection. *Prod. Eng. Res. Devel.* (2022). <https://doi.org/10.1007/s11740-022-01164-5>
- [5] F. Dausinger: *Strahlwerkzeug Laser: Energieeinkopplung und Prozeßeffektivität* (1995) Habilitation. Universität Stuttgart, Germany.

515 nm wavelength laser for laser melt injection of high-quality MMC in Cu-ETP

Anika Langebeck*¹ , Annika Bohlen¹ 

¹ BIAS – Bremer Institut für angewandte Strahltechnik GmbH, Klagenfurter Str. 5, 28359 Bremen, Germany

Abstract

Laser melt injection (LMI) is used to improve abrasive wear resistance by building a metal matrix composite (MMC) layer in highly loaded tool surfaces. But LMI for highly conductive and highly reflective materials like copper can be very challenging. Nowadays high-power laser beam sources with visible wavelengths are available enabling LMI in these materials.

This paper shows a suitable process window for LMI with 515 nm wavelength laser in pure copper with spherical fused tungsten carbide as reinforcing phase. High-quality MMC can be manufactured by using laser power intensities in the range of 10^4 W/cm² and conduction heating of the matrix material between 300 °C and 400 °C. The microstructure exhibits only a few imperfections and has a high particle content of 44 %.

Keywords: laser melt injection, metal matrix composite, tungsten carbide, Cu-ETP, visible wavelength laser

1 Introduction

Laser melt injection (LMI) is used as a surface modification technology to improve the abrasive wear resistance of metallic surfaces. During LMI metal matrix composites (MMC) are generated by blowing hard particles into the laser induced melt pool. Different to laser metal deposition the powder is not melted during the process and remains in its initial shape forming a heterogenous MMC microstructure. These MMC are very beneficial to reduce abrasive wear volume of highly loaded tools, like injection molds, welding jaws, bearings etc. which are often steel-, aluminum- or copper-based [1]. As reinforcing phase chromium, tungsten and silicon carbide particles are often used [2].

Especially laser processing of materials with poor absorptivity for common laser wavelengths around 1 µm like pure copper (e.g., Cu-ETP) can be very challenging. This can be countered on the one hand by using very high intensities which lead to high quality results for deep-penetration weld seams [3]. And on the other hand, by using laser with a shorter wavelength, which are absorbed better by copper surfaces and show good results as well [4]. The latter option is beneficial for LMI since high intensities during LMI can lead to agglomeration of the reinforcing hard particles [5]. Within the last few years frequency-doubled disk lasers emitting a wavelength of 515 nm are commercially available and can reach a maximum output power of > 1 kW, which is very advantageous for LMI in pure copper. Besides the laser beam source additional preheating can improve the welding quality in copper by compensating for the high thermal conductivity [6].

This paper addresses a process window for a stable LMI process yielding high-quality MMC made of Cu-ETP reinforced with spherical fused tungsten carbide (sFTC). Microstructural analyses were conducted to determine the effect of the process parameters on the MMC quality.

2 Experimental set-up

For laser melt injection a 2 kW Trumpf laser with 515 nm wavelength (TruDisk 2021) was used. The laser beam was guided via a 0.6 mm core diameter laser light cable to the processing head. The processing head was

made of an optical unit, Trumpf BEO D70 with 200 mm collimation length and focal length, equipped with a coaxial three-jet powder nozzle (Ixun) with 16 mm working distance. The laser beam was defocused to a spot diameter of 1.9 mm during LMI. See Fig. 1 for the beam caustic and laser power distribution at different working positions.

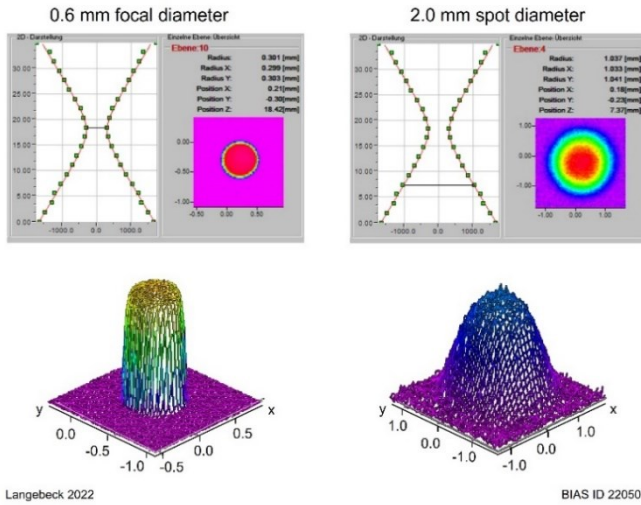


Fig. 1: Laser beam caustic and power distribution for TruDisk 2012, with 0.6 mm laser light cable, 200 mm collimation and focal length

To maintain a sufficient and stable melt pool size during the process a heating device (G. Maier Elektrotechnik) was used to preheat the substrate material before LMI and was also used during LMI. The necessity of a substrate heating is known from earlier studies [7]. A Metis H322 two-color pyrometer (Sensortherm), with 700 °C to 2300 °C measuring range, was used to track the melt pool temperature during LMI. The pyrometer was laterally integrated onto the processing head. Fig. 2 shows the experimental set-up.

Pure copper (Cu-ETP) with a high thermal conductivity of 394 W/m·K (at 20 °C) was used as substrate material. The substrates were cut into small bricks with 50 mm length, 20 mm width and 12 mm height. Spherical fused tungsten carbide particles (sFTC), supplied by Oerlikon Metco WOKA GmbH, with -106 μm +45 μm particle size were used to reinforce the Cu-ETP substrates during LMI.

With this set-up the effects of the heating device temperature and laser power on the MMC microstructure and process zone temperature were examined in fivefold determination. For this five MMC single tracks per parameter-set were manufactured on one Cu-ETP substrate. Between every single track the substrates cool down in order to provide similar starting conditions for each of the five single tracks. See Tab. 1 for the varied and constant process parameters. The process window ranged from 1.6 kW to 1.8 kW laser power which corresponds to a laser power intensity of $5.7 \cdot 10^4$ W/cm² and $6.4 \cdot 10^4$ W/cm², respectively. The heating device temperature ranged from 300 °C to 400 °C.

To characterize the microstructure optical microscopic (OM) images of the MMC tracks were recorded. The particle content of the MMC was calculated by using an automated image processing based on binarized OM images of the MMC cross-sections.

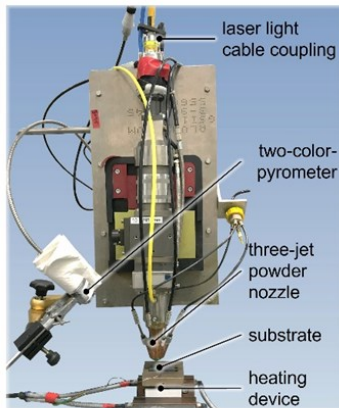


Fig. 2: Experimental set-up

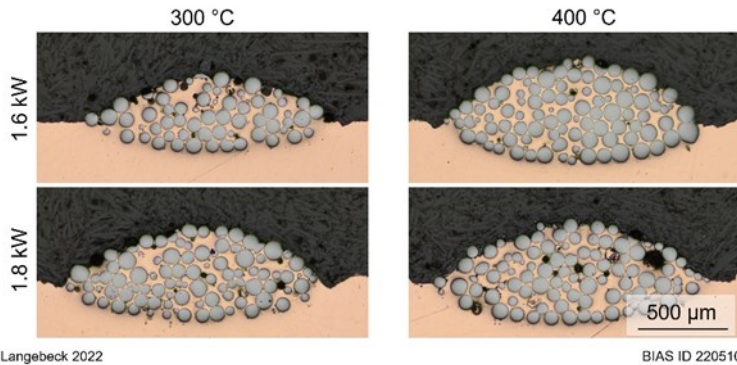
Tab. 1: Process parameters

Process parameter	Value(s)
Laser power	1.6 kW; 1.8 kW
Heating device temperature	300 °C; 400 °C
Powder mass flow	5.5 g/min
Process velocity	150 mm/min
Carrier gas flow (Ar)	3.5 l/min
Shielding gas flow (Ar)	15 l/min
Track length	40 mm

3 Results

Fig. 3 shows cross-sections of MMC single tracks manufactured within the proposed process window (Tab. 1). With increasing the laser power (Fig. 3, top to bottom) the MMC track geometry increases as well. Same applies for increasing heating device temperature (Fig. 3, left to right). A more detailed evaluation of the influence of the process parameters on the track geometry can be found here [7].

From these cross-sections the particle content of the MMC tracks was determined (see Tab. 2). No impact of the used laser power, the used heating device temperature, or an impact of the interaction between both factors were detected for the examined process window. The mean particle content was between 43% (for 1.6 kW laser power, 300 °C heating device temperature) and 45% (for 1.8 kW laser power, 300 °C) with a standard deviation ranging between 1.3% and 3.3%.

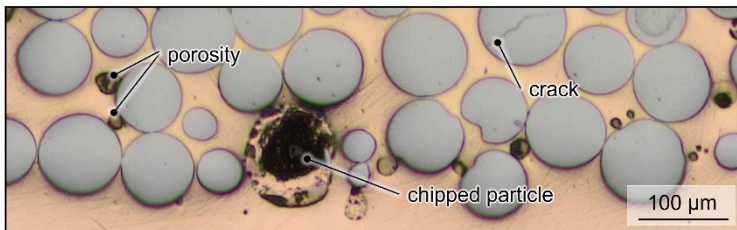


Tab. 2: Particle content

		heating device temp.	
		300 °C	400 °C
laser power	1.6 kW	42.7% ±1.7%	44.7% ±3.3%
	1.8 kW	45.0% ±1.3%	43.5% ±1.9%

Fig. 3: Exemplarily OM images of MMC cross-sections manufactured with varying laser power and heating device temperature during LMI

With all parameter-sets high-quality MMC were manufactured. Though in some cases, imperfections within the MMC tracks were visible (see Fig. 4). A few micro-cracks in the hard particles occurred as well as a few pores near by the sFTC particles. Some OM images show larger pore-like imperfections which can be attributed to particles which were chipped during the preparation process of the cross-sections. A significant impact of the examined process parameters on the imperfections was not detected.



process parameters		heating temperature	300 °C
laser power	1.6 kW	powder mass flow	5.5 g/min
Langebeck 2022		BIAS ID 220511	

Fig. 4: OM image with higher magnification to exemplarily show imperfections within the MMC microstructure

The process zone temperature measured by two-color pyrometer was affected by the used laser power. With increasing laser power, the process zone temperature slightly increased from 1527 °C to about 1563 °C (see Fig. 5). For the heating device temperature, no impact on the process zone temperature was detected.

4 Discussion

Some imperfections within the MMC surface were observed. The cracks in the particles are caused by different coefficients of thermal expansion with $6.4 \cdot 10^{-6} \text{K}^{-1}$ to $7.4 \cdot 10^{-6} \text{K}^{-1}$ for tungsten carbide [8] and $16.5 \cdot 10^{-6} \text{K}^{-1}$ for copper [9]. This mismatch leads to micro-cracks during/after LMI which was shown for other material combinations as well [10]. The chipping of particles (see Fig. 4), which occurred during the preparation of the cross-sections can be a result of excessively cracked particles or can be an indicator for lack of fusion between sFTC and Cu matrix.

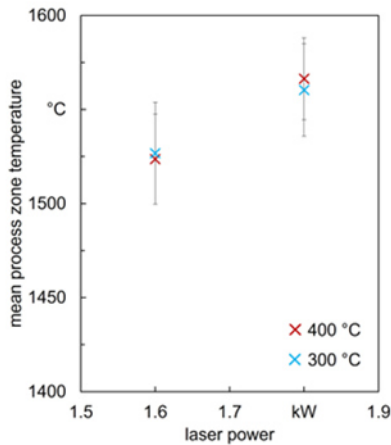


Fig. 5: Mean process zone temperature in dependence of the used laser power and heating device temperature

5 Conclusion

High-quality MMC can be manufactured by using laser power intensities in the range of 10^4 W/cm² and additional conduction heating of the matrix material between 300 °C and 400 °C. Within this process window a stable particle content of 44% can be reached.

Acknowledgements

The IGF-Project with the IGF-No.: 21079 N / DVS-No.: 06.3341 of the “Forschungsvereinigung Schweißen und verwandte Verfahren e. V.” of the German Welding Society (DVS), Aachener Str. 172, 40223 Düsseldorf was funded by the Federal Ministry for Economic Affairs and Climate Action (BMWK) via the German Federation of Industrial Research Associations (AiF) in accordance with the policy to support the Industrial Collective Research (IGF) on the basis of a decision by the German Bundestag. Furthermore, the authors gratefully acknowledge the collaboration with the members of the project affiliated committee regarding the support of knowledge, material, and equipment over the course of the research.

Supported by:



on the basis of a decision by the German Bundestag



References

- [1] Zou, Y.; Tan, C.; Qiu, Z.; Ma, W.; Kuang, M.; Zeng, D.: Additively manufactured SiC-reinforced stainless steel with excellent strength and wear resistance. In: Additive Manufacturing 41 [1] (2021) p. 101971
- [2] Nurminen, J.; Näkki, J.; Vuoristo, P.: Microstructure and properties of hard and wear resistant MMC coatings deposited by laser cladding. In: International Journal of Refractory Metals and Hard Materials 27 [2] (2009) p. 472-478
- [3] Heider, A.; Stritt, P.; Weber, R.; Graf, T.: High-power laser sources enable high-quality laser welding of copper. ICALOE® 2014: 33rd International Congress on Laser Materials Processing, Laser Microprocessing and Nanomanufacturing; October 19–23, 2014; San Diego, California, USA; Hrsg.: S. Kaierle. In: ICALOE 2014: 33rd International Congress on Laser Materials Processing, Laser Microprocessing and Nanomanufacturing; Laser Institute of America; Orlando, FL (2014) p. 343-348
- [4] Hess, A.; Schuster, R.; Heider, A.; Weber, R.; Graf, T.: Continuous Wave Laser Welding of Copper with Combined Beams at Wavelengths of 1030 nm and of 515 nm. In: Physics Procedia 12 (2011) p. 88-94
- [5] Fedorov Kukuk, A.; Freiße, H.; Bohlen, A.; Vollertsen, F.: Laser melt injection of hard particles with beam wobbling for wear protection of micro-injection molding tools. Lasers in Manufacturing Conference (2019)
- [6] Auwal, S. T.; Ramesh, S.; Yusof, F.; Manladan, S. M.: A review on laser beam welding of copper alloys. In: The International Journal of Advanced Manufacturing Technology 96 [1-4] (2018) p. 475-490
- [7] Langebeck, A.; Bohlen, A.; Seefeld, T.; Zhang, X.; Kormmeier, J. R.; Hofmann, M.; Alameddin, S.; Alessio, R. P.; Fritzen, F.: Laser melt injection of spherical fused tungsten carbide in Cu-ETP with 515 nm wavelength laser. In: Procedia CIRP 111 [1] (2022) p. 726-731
- [8] Lynch, C. T.: Practical Handbook of Materials Science. CRC Press (1989)
- [9] CRC handbook of chemistry and physics - A ready-reference book of chemical and physical data. CRC Press; Taylor & Francis; Boca Raton, Fla., London (2011)
- [10] Wang, J.; Li, L.; Tao, W.: Crack initiation and propagation behavior of WC particles reinforced Fe-based metal matrix composite produced by laser melting deposition. In: Optics & Laser Technology 82 (2016) p. 170-182

Materials Characterization at High Strain Rates

Tobias Valentino*¹ , Eric A. Jägler², Tim Radel¹ 

¹BIAS - Bremer Institut für angewandte Strahltechnik GmbH, Klagenfurter Str. 5, 28359 Bremen, Germany

²Universität der Bundeswehr München - Institute of Materials Science, Werner-Heisenberg-Weg 39, 85577 Neubiberg, Germany

Abstract

The identification of material properties at high strain rates is of considerable technical interest, e.g., in applications for passenger safety-related parts which are expected to absorb energy in case of collisions. To additionally meet the requirements of a rapid and resource-efficient materials characterization, a novel high-speed hardness testing method based on laser-induced shock waves was investigated. The principal applicability of this laser-induced shockwave indentation technique for materials characterization at high strain rates is shown.

Keywords: Laser shock processing, High throughput, Measurement

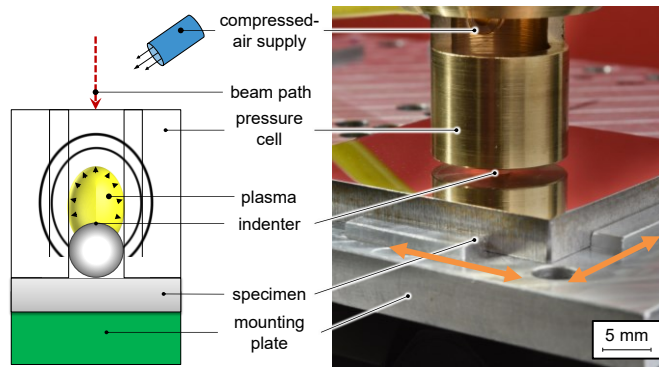
1 Introduction

Besides various safety-related applications, strain rates can reach up to 10^4 s^{-1} for most metal fabrication processes like cutting, forging, stamping, or forming [1]. The deformability is affected by strain rate because of microstructural reasons combined with dislocation mechanics [2]. Amongst others, mild steel, carbon steels, austenitic steels, and maraging steels become strain rate sensitive above 10^3 s^{-1} [3]. So far, ballistic testing is a widely used and standardized process. However, several challenges arise when performing tests at cycle rates above 10 times the speed of the standard procedures [4] and at strain rates above 10^2 s^{-1} . Those challenges concern the limited dynamics of mechanical and measurement processes, which lead to inaccuracies. This gives reason to explore and identify material characteristics at high strain and cycle rates.

Suitable mechanical-based techniques rarely exist, which also consider the ongoing demand for rapid materials characterization. So far, those techniques are performed on a nanoscale as weight and stiffness are the limiting factors for mechanical-based indentation systems [1]. For this purpose, high speed nano-indentation testing has emerged as an advanced materials characterization technique to study mechanical properties at strain rates between $10^1 \dots 10^3 \text{ s}^{-1}$. Moreover, with improved electronics and novel designs, it is already possible to perform those tests faster than 1 s per indent [5]. Larger systems like ballistic testing are considerably slower.

To increase the testing speed at a larger scale, a new materials characterization approach is being studied which is based on laser-induced shock waves. This laser-based technique (Fig. 1) is hereinafter referred to as LiSE. Characteristic values are extracted from the indentation geometry, which correlate with mechanic material properties.

A TEA-CO₂ laser is used to induce shock waves above spherical indenters. So far, up to 90 indentations per minute can be created reproducibly with LiSE [6]. Reproducible indentations are theoretically possible at cycle rates of more than 20 Hz [7]. The TEA-CO₂ laser creates quasi-instantly a plasma at laser intensities $> 10^8 \text{ W/cm}^2$, which absorbs nearly all the laser-specific wavelength of $10.6 \mu\text{m}$ [8]. The plasma absorption hinders ablation on metals and technical ceramics [9] which is why ablation layers are not necessary [10].



Valentino 2022
 Fig. 1: Setup of the laser-induced shock wave indentation technique

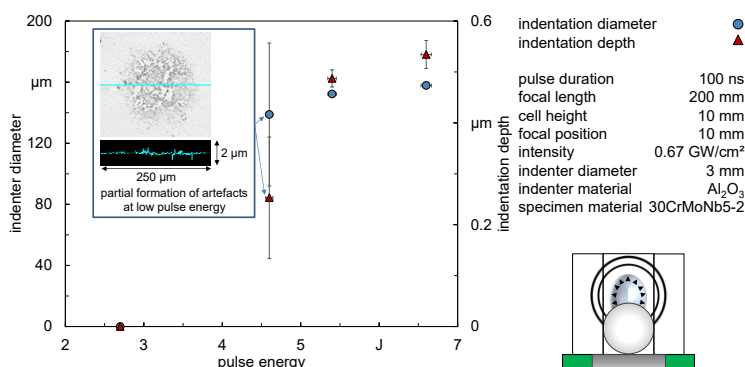
The shock wave is the result of the laser-plasma-interaction, which is used to penetrate the indenter inside a specimen. The indenter is penetrated inside the specimen at more than 10^3 s^{-1} [11]. Amongst others, the strain rate is influenced by the pulse energy and pressure cell [6]. So far, it has been found that the extracted characteristic values indentation depth, pile-up height, and indentation diameter strongly correlate with the Vickers hardness [11] and tensile strength [12].

2 Methods

In this study, LiSE was used to investigate the feasibility to characterize the ballistic steel 30CrMoNb5-2. Such ballistic steel is usually tested at high strain rates with ballistic tests. Material properties were determined according to [6] and compared to conventionally measured values. The pulse energy was varied between 2.7 J and 6.6 J. The LiSE setup is described in detail in [6].

3 Results and Discussion

The resulting indentation diameter and depth as function of pulse energy are shown in Fig. 2. Both characteristic values increase with increasing pulse energy. No indentation is found for the lowest pulse energy of 2.7 J. When increasing the pulse energy to 4.6 J, artefacts are observed on the surface (Fig. 2). These artefacts lead to an increase of the deviation of the measured indentation depth and diameter. The artefacts can be explained by a phase transformation of the retained austenite present in the as-delivered state to a martensitic structure in the deformation area. Martensite causes a volume change in the microstructure [13] leading to a subsequent bulging of the surface. Such effects are also observed for harder materials and higher pulse energies but similar material compositions [6]. The Vickers hardness and the tensile strength are calculated from the measured characteristic values according to [6]. The calculated hardness (Fig. 3 a) and tensile strength (Fig. 3 b) decrease with increasing pulse energy. A higher pulse energy leads to a larger strain rate [6]. Larger strain rates are associated with increase in yield strength [3]. The contrary effect is observed here. Especially, the calculated tensile strength is considerably lower compared to the specified one determined under standard conditions. Thermal effects significant to the process are not induced by the laser [14]. However, adiabatic heating may affect the indentation process at higher strain rates. In future research, this contrary strain rate effect will be investigated for LiSE. Nevertheless, it is suggested that strain rate effects significantly affect the hardness and tensile strength for 30CrMoNb5-2. Thus, LiSE is potentially suitable for hardness and tensile characterization of materials that experience high strain rates during application and accordingly, need to be tested under these conditions.



Valentino 2022
 Fig. 2: Indentation diameter and depth in dependence of the pulse energy

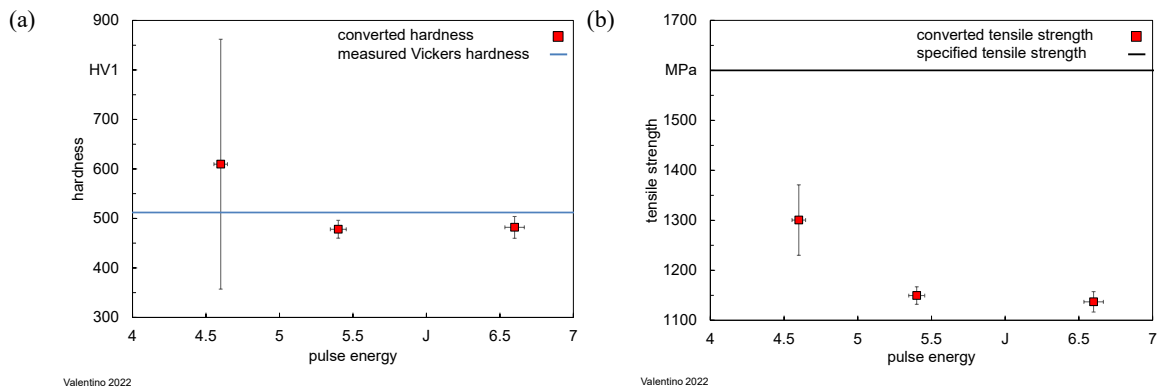


Fig. 3: (a) Converted and measured hardness and (b) converted and measured tensile strength in dependence of the pulse energy

4 Summary

The principal applicability of the laser-induced shockwave indentation technique for materials characterization at high strain rates is shown for the ballistic steel 30CrMoNb5-2.

Acknowledgements

Financial support of the subproject D02 “Laser induced hardness measurements” funded by the Deutsche Forschungsgemeinschaft (DFG, German Research Foundation) – Project number 276397488 – SFB 1232 is gratefully acknowledged.

References

- [1] LW Meyer (2004) Material Behaviour at High Strain Rates. 1st ICHSF, 45-56.
- [2] BO Reinders, H-D Kunze (1990) Influence of Mechanical Twinning on the Deformation Behavior of Armco Iron. Shock Waves and High-Strain-Rate Phenomena in Materials, Eds. MA Meyers, LE Murr, KP Staudhammer, M Dekker, 127-136.
- [3] H-D Kunze, LW Meyer (1986) Materials for Extreme Dynamic Loads. Metallurgical Applications of Shock Waves and High-Strain-Rate Phenomena, Eds. LE Murr, KP Staudhammer, MA Meyers, M Dekker, 481- 507.
- [4] MF Maier, K Stowe, S Sieg (2007) Combinatorial and high-throughput materials science. Angewandte Chemie - International Edition 46, 6016–6067.
- [5] B Vignesh, WC Oliver, G Siva Kumar, P Sudharshan Phani (2019) Critical assessment of high speed nanoindentation mapping technique and data deconvolution on thermal barrier coatings. Mater Des 181, 108084.
- [6] T Valentino (2021) Nutzung laserinduzierter Stoßwellen zur Hochdurchsatz-Werkstoffprüfung. Universität Bremen. DOI: 10.26092/elib/1435
- [7] H Wielage (2011) Hochgeschwindigkeitsumformen durch laserinduzierte Schockwellen. Strahltechnik 44, Eds. F Vollertsen, R Bergmann. BIAS Verlag, Bremen.
- [8] HW Bergmann, H Hügel (1998) Modellierung und Diagnostik des Abtragsprozesses. Strahltechnik, Band 6, 35-44.
- [9] U Trdan, JA Porro, JL Ocaña, J Grum (2012) Laser shock peening without absorbent coating (LSPwC) effect on 3D surface topography and mechanical properties of 6082-T651 Al alloy. Surf Coat Technol 208, 109–116.
- [10] S Veenaas, H Wielage, F Vollertsen (2014) Joining by laser shock forming: realization and acting pressures. Prod Eng 8, 283–290.
- [11] T Czotscher, DO Bager, F Vollertsen, I Piotrowska-Kurczewski, P Maaß (2019) Connection between shock wave induced indentations and hardness by means of neural networks. AIP Conf Proc 2113, 1-6.
- [12] T Czotscher, A Von Hehl, T Radel, A Toenjes (2020) Correlation between Shock Wave-induced Indentations and Tensile Strength. Proc Manuf 47, 756–760.
- [13] GB Olson, M Cohen (1972) A mechanism for the strain-induced nucleation of martensitic transformations. J Less-Common Met 28, 107–118.
- [14] T Czotscher, F Vollertsen (2018) Plasma Induced On Indenter Balls. 8th ICHSF, 1-10.

Tensile strength of Nitinol flanges fabricated by laser rod end melting and immediate flange processing

Yang Lu*¹ , Tim Radel¹ 

¹ BIAS - Bremer Institut für angewandte Strahltechnik GmbH, Klagenfurter Straße 5, Bremen 28359, Germany

Abstract

Nitinol is a shape memory alloy used for actuator applications. However, the connection between Nitinol wire and mechanical system via adhesive bonding or crimping could be weakened due to the exposure of joint in aggressive environments and temperature changes. Therefore, a process chain called laser rod end melting with immediate flange processing has been put forward and proven to fabricate all-in-one Nitinol flanges. According to previous work, there is a partially solidified preform connecting to the wire as the shaft, where the connection fractures under tensile tests. In the present study, the effect of size of partially solidified preform on the tensile behavior was investigated on the cylindrical flanges with different flange heights. The results show that the partial preform volume increases with the flange heights, while the tensile strength becomes smaller when the flange height is too small. This suggests that it is important to maintain the mechanical strength of Nitinol flange by choosing the appropriate flange height.

Keywords: Shape memory alloy, Laser rod end melting, Flange processing, Tensile strength

1 Contents

Nowadays, Nitinol (shape memory alloy) wires are used as actuators to conduct mechanical actions with temperature changes or heated with electrical current, widely applied in medical, automobile and aerospace industries. At present the solution of attachment to mechanical systems are mostly crimping, screwing [1] and adhesive bonding [2]. However, the adhesive bonding may have a weakened chemical and thermal resistance when the joint is exposed to aggressive environment such as chemical solution and cyclic temperature change. Thus, a robust method to fabricate all-in-one flanges is required to fulfill this application condition. Here, a so-called laser rod end melting process serve as a solution. This process is a thermal process that generates material accumulation called melt and preform (before and after complete solidification) at the end of a wire, followed by die forming or rotary swaging leading to final geometry. This process has been successfully applied to fabricate micro flange from stainless steel [3].

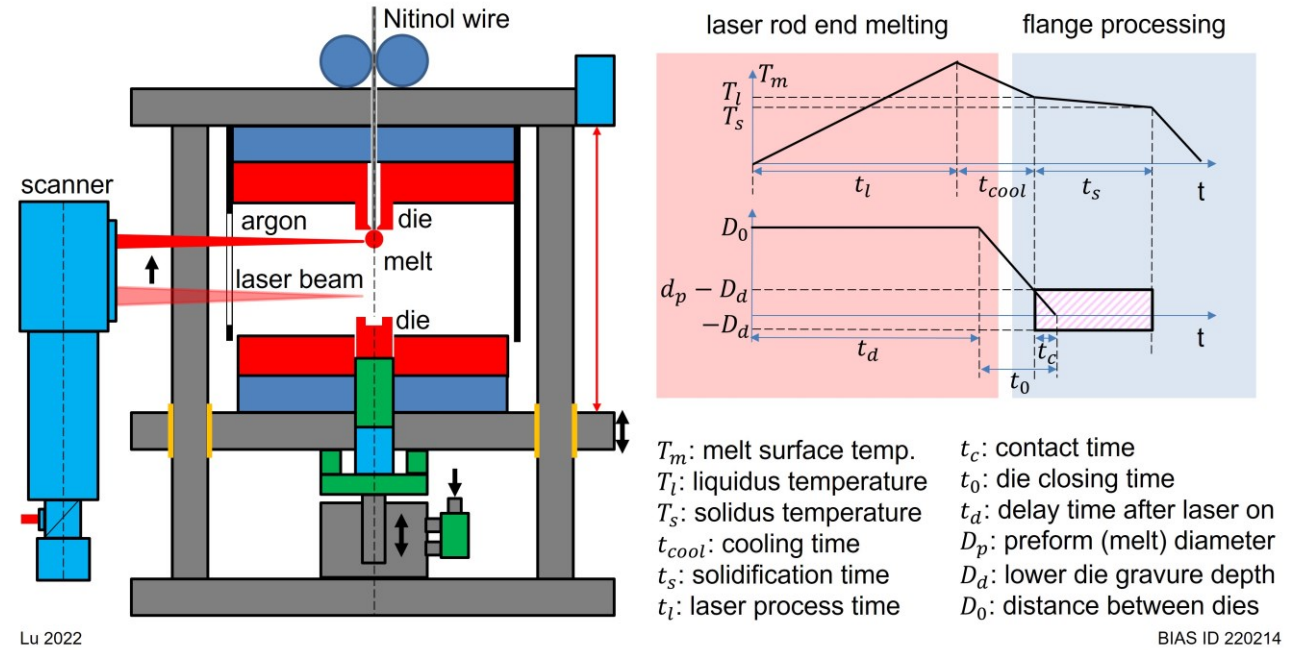
However, cold forming ability of Nitinol is limited because of ductility limitation and work-hardening [4]. Regarding this, the authors have developed a new approach of flange processing [5], showing that it is possible to produce chemically and thermally resistant Nitinol flanges. The fabricated flange shows a partially solidified preform connected to the wire and a newly distributed zone. Instead of the flange processing, the laser rod melting determines the microstructure distribution crossing fusion line where grain size varies and the wire-flange connection fractures under loading. In addition, the heat-treated Nitinol flange shows an improved tensile strength due to generation of metastable precipitates, indicating that the microstructure is one of factors determining the tensile behavior. In this work, it is aimed to fabricate cylindrical Nitinol flange with different heights, and the factors affecting the tensile behavior will be investigated by comparing microstructure distribution and fracture surface topography.

2 Methodology

Fig. 1 shows the processing system for fabrication of Nitinol cylindrical flange. The chemical composition is listed in Tab. 1. The whole process is conducted in a semi-sealed chamber with the constant input of argon gas. The wire end is melted by a moving laser beam into an accumulated melt, until it reaches the upper die with a comparable volume of the lower die cavity. The laser works in a continuous-wave mode and has a wavelength of 1070 nm. During the flange processing, a pneumatic cylinder pushes the lower die upwards to reshape the melt, after a specific delay time from the start of laser melting. Assuming that the surface temperature of the melt represents its average temperature, the delay time is calculated according to the temperature-time course measured by a quotient camera and the time sequence in Fig. 1.

Tab. 1: Chemical composition of used Nitinol wire according to ASTM 2063-18

composition	Ni	C	O	Fe	Ti
wt%	56.15	0.009	0.0176	<0.01	remain



Lu 2022

BIAS ID 220214

Fig. 1: Experimental setup for laser rod end melting and flange processing of Nitinol wire and their working sequence

The used lower die has a tunable bottom, so that different volume of die cavity can be set by varying its depth. Based on this the flanges with different heights can be fabricated. Correspondingly the wires with different lengths are molten, and these flanges are fabricated with the cavity depth of 0.2, 0.4 and 0.6 mm and cavity diameter of 3 mm. It has to be mentioned that the reproducibility of flange using cavity depth of 0.2 mm is quite low. In this work, the laser and flange processing parameters for flange fabrication are listed in Tab. 2, and flanges with different heights are fabricated multiple times. Afterwards, tensile tests are conducted on the fabricated flanges in a universal test machine with a constant strain rate of 0.0067 1/s. Moreover, the surface quality and microstructure of fabricated flanges are analyzed with an optical microscope and metallographic preparation by Kroll solution (93 mL H₂O, 5 mL HNO₃ and 2 mL HF, etched for 2 mins). The fractography of tested flanges is analyzed by a confocal microscope.

Tab. 2: Laser and flange processing parameters for fabrication of Nitinol flanges

laser power [W]	scan speed [mm/s]	spot diameter [μ m]	die speed [mm/s]	die temperature [$^{\circ}$ C]
85	5	55	48	20

3 Results

Fig. 2 shows the successful fabrication of cylindrical Nitinol flanges with different heights. The surface appears reflective without evident oxide layer. Fig. 3 show the comparison between the geometry and microstructure of flange. For the flange size, the flange height is generally larger than the die cavity depth. Inside the flange, there are three typical zones: heat affected zone (Zone A), partially solidified preform (Zone B) and newly distributed Zone C. The grain size varies from Zone A to Zone C and the grains of both fusion zones orient towards each other. The solidification front in Zone C is always found in the center, and it coincides

with the boundary between Zone B and Zone C partially. With decreasing die cavity depth, the flange height and thickness of Zone B becomes smaller.

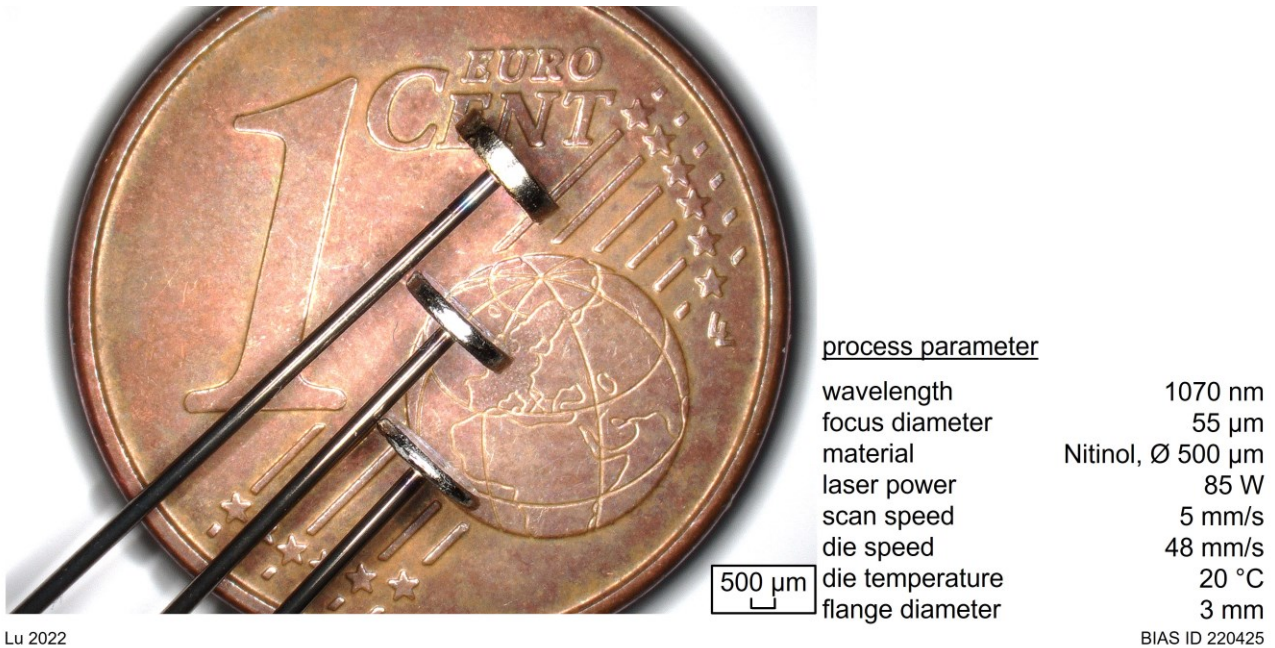


Fig. 2: Nitinol flanges with cylindrical shape

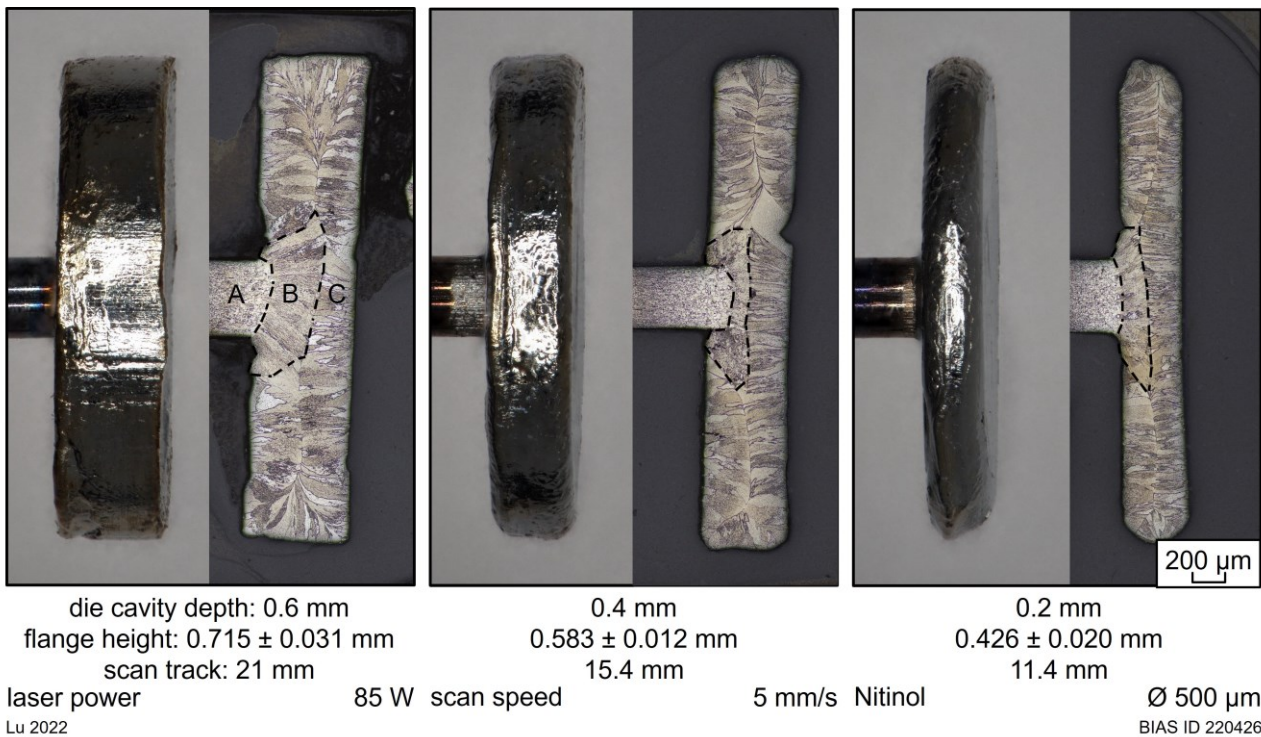


Fig. 3: Surface quality and microstructure distribution of the cylindrical Nitinol flanges with different flange heights

Fig. 4 shows the tensile behavior and fracture results of flanges in Fig. 3, and the maximum of height map scale in the fracture surface topography stands for the base surface of flange. The tensile test of original wire is based on the previous work. Each strain stress curve is made of average value and standard deviation from the multiple tests. In general, curves of flanges and wires overlap each other. The curve of wire shows a typical loading stress plateau with increasing strain. In comparison, flanges with average heights of 513 μm and 715 μm fracture in the loading plateau, while the flanges for 426 μm fracture before entering this phase. The corresponding fracture topographies show that material at the connection between the flange and wire is pulled out, and the maximum fracture depth increases with the flange height. In addition, the fractured wires and flanges are comparable.

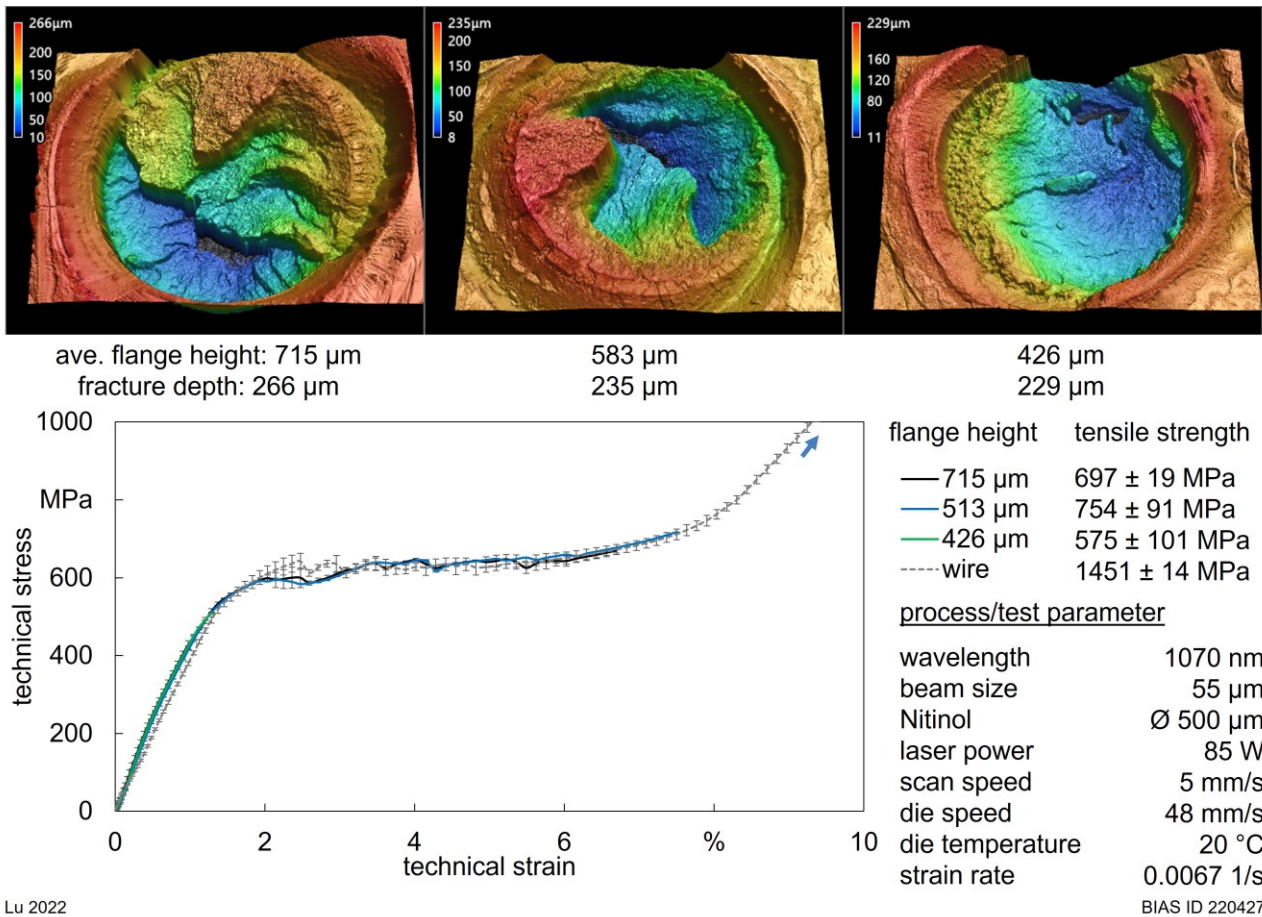


Fig. 4: Tensile tests of cylindrical Nitinol flanges with different flange heights and corresponding fracture surface topography in height map

4 Discussion

By comparing with previous work, in this study it shows that the laser rod end melting and flange processing enables the fabrication of cylindrical Nitinol flange besides the truncated cone shaped one. Despite of the flange shape, the partially solidified preform and newly distributed zone are always generated in the flange. With decreasing flange size, the former zone becomes smaller (cf. Fig. 3). By comparing the axial size of partially solidified preform (Zone B) and fracture height map (see Fig. 4), it shows that the flanges with height of 513 μm and 715 μm fracture inside Zone B (see Fig. 3) while this zone in the flange with height of 426 μm is almost pulled out. This corresponds to its lower tensile strength, indicating that the boundary between the partially solidified preform (Zone B) and newly distributed zone is a weaker zone compared to the heat affected zone in wire and wire-flange connection [5]. Nevertheless, this phenomenon can be avoided by the larger partially solidified preform. One reason might be explained by the wedge-shaped newly distributed zone preventing from the pull-out of partial preform. In addition, the tensile strength between cylindrical flanges with height of 513 μm and 715 μm and the truncated cone shaped ones from previous work are comparable.

5 Conclusions

The following conclusions can be drawn based on the investigation:

- Laser rod end melting and flange processing in a not fully solidified state enable the fabrication of Nitinol flange with cylindrical shape.
- The boundary between the partially solidified preform (Zone B) and newly distributed zone inside the flange is a weak point, and too small former zone leads to its fracture under lower tensile stress. Therefore, miniaturization of Nitinol flange while maintaining its mechanical strength is achieved by choosing the appropriate flange size.

Acknowledgements

The authors gratefully acknowledge the financial support for the project “Laserschmelzen im Gesenk” funded by the Deutsche Forschungsgemeinschaft (DFG, German Research Foundation) – Project number 449377606.

References

- [1] Mertmann, M.; Vergani, G. 2008. Design and application of shape memory actuators. *The European Physical Journal Special Topics*. 158. pp. 221–230.
- [2] Lin, F.-Y.; Bergeles, C.; Yang, G.-Z. 2015. Biometry-based concentric tubes robot for vitreoretinal surgery. *Annual International Conference of the IEEE Engineering in Medicine and Biology Society*. 2015. pp. 5280–5284.
- [3] Vollertsen, F.; Friedrich, S., et al. 2020. *Cold Micro Metal Forming*. Springer International Publishing. Cham.
- [4] Hodgson, D.; Russell, S. 2000. Nitinol melting, manufacture and fabrication. *Minimally Invasive Therapy & Allied Technologies*. 9. pp. 61–65.
- [5] Lu, Y.; Radel, T. 2022. Tensile strength of Nitinol flanges produced by laser rod end melting and immediate flange processing in a not fully solidified state. *Procedia CIRP*. 111. pp. 721–725.

On the combination of plasma nitrided surfaces and LIPSS

Lewin Rathmann*¹ , Henning Hasselbruch², Andreas Mehner², Tim Radel¹ 

¹BIAS - Bremer Institut für angewandte Strahltechnik GmbH, Klagenfurter Str. 5, 28359 Bremen, Germany

²Leibniz-Intitut für Werkstofforientierte Technologien, Badgasteiner Str. 3, 28359 Bremen, Germany

Abstract

LIPSS are subjected to excessive wear when exposed to direct contact in tribological applications. Therefore, precautions must be taken to increase LIPSS' hardness and wear resistance while simultaneously preserving their properties like superhydrophilicity. This work shows that a firstly plasma nitrided and subsequently structured surface results in LIPSS of high nano-hardness ($14.88 \text{ GPa} \pm 1.05 \text{ GPa}$) who show a super hydrophilic wetting behavior (contact angle of 7°). The results indicate that a previous nitriding could bring LIPSS into tribological applications.

Keywords: Laser micro machining, Surface modification, Steel, LIPSS

1 Introduction

Sheet metal processes such as deep drawing are highly efficient due to high material utilization while simultaneously being subjected to friction. This friction is reduced using mostly conventional, mineral oil-based lubricants. But due to the increasing environmental awareness, the application of alternative lubricants is of great interest. A great step towards this objective would be the utilization of deionized water in forming applications. One major obstacle is its low viscosity that provides water from staying where it is needed like the contact zones between the die and the blank. This obstacle could be overcome using surface structures like laser induced periodic surface structures (LIPSS) that alter surface properties making surfaces i.e., hydrophile. The problem is that these nanostructures wear off in direct tribological contact. Therefore, processes are needed to increase the hardness as well as the wear resistance of the LIPSS or even to protect them from direct contact. Previously investigated solutions included laser hardening [1], the combination of LIPSS and PVD hard coatings [2], and the use of hierarchical structures [3]. To provide further possibilities for preparing surface structures for tribological applications, this work combines plasma nitrided surfaces with different surface structures. It is shown that this combination leads to an increased hardness of LIPSS while preserving their hydrophilic behavior at the same time.

2 Methodology

As substrates hardened and tempered cylindrical disks made of 1.2379 with diameters of 32 mm, thicknesses of 4 mm, and an initial hardness of $62 \pm 2 \text{ HRC}$ were used. Each disk was polished to a mean arithmetic height of smaller than 6 nm. Subsequently, plasma nitriding processes by varying the gas compositions and treatment durations were carried out on all disks in a plasma nitriding device of type Eltropuls. The nitriding parameters are shown in Tab. 1. At a gas flow rate ratio of 1:7 (6/43 l/h N_2/H_2) no hard and brittle compound layers (CL) are formed. When increasing the N_2/H_2 ratio to 1:1 the formation of CL takes place. Since all other nitriding parameters were kept constant, both the depth of the diffusion layers (DL) and the thicknesses of the compound layers only depend on the nitriding durations. Further information is provided in [4, 5, 6]. According to the test setting of Tab. 1, not only the mechanical properties of the near-surface regions are significantly influenced. This refers to the surface hardness, the hardness depth curve, and thus the mechanical supporting function, which have a direct impact on the achievable tribological properties. In addition, the chemical surface

properties are influenced by the gas composition and plasma nitriding duration resulting in different phase proportions such as formed martensites, Fe_3C or Cr_{26}C_6 measured by X-ray diffraction (XRD). Plasma nitriding affects the amounts of formed nitrides such as γ' - Fe_4N and ϵ - Fe_3N , see Tab. 1. The different gas flow ratios and nitriding duration results in different nitriding hardness depths (NHD) and compound layer thicknesses (CLT) which can also be taken from Tab. 1.

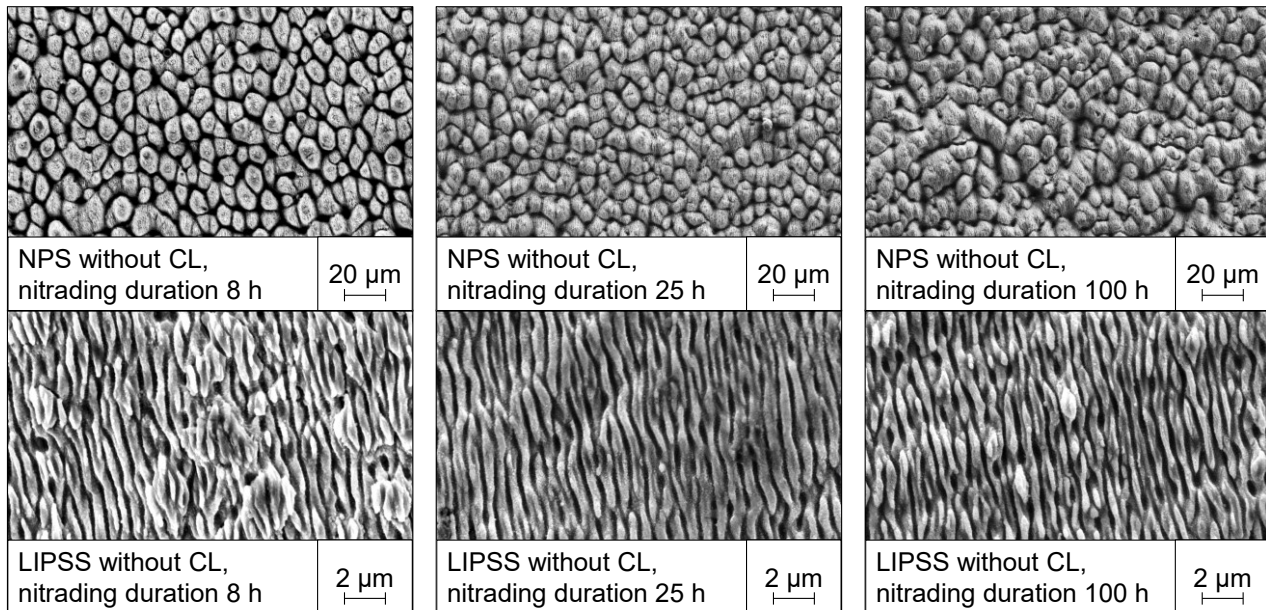
Tab. 1: Plasma nitriding parameters and resulting nitriding hardness depths (NHD), compound layer thicknesses (CLT) and quantitative phase proportions of γ' - Fe_4N and ϵ - Fe_3N nitrides.

Temperature in °C	Duration in h	N_2 -flow in l/h	H_2 -flow in l/h	NHD in mm	CLT in μm	γ' : Fe_4N in %	ϵ : Fe_3N in %
480	8	6	43	0.07	0	9,6	8,1
480	25	6	43	0.10	0	5,6	9,1
480	100	6	43	0.22	0	19,1	10,1
480	8	25	25	0.09	4	9,3	53,5
480	25	25	25	0.17	7	13,0	56,3
480	100	25	25	0.26	13	17,4	58,9

As surface treatment these disks were structured with LIPSS and none-periodic structures (NPS) which result due to different laser fluences. As laser source, the pulsed fiber laser TruMicro 5050 by Trumpf was used. The pulse energy was set to 200 μJ for LIPSS and 225 μJ for NPS at a repetition rate of 50 kHz and a single path cycle. The laser spot size on the substrate was set to 46 μm . The path trajectory consisted of parallel, equidistant lines. The LIPSS emerged at a path distance of 36.8 μm , while the distance was set to 2.3 μm for the NPS. The overview images of the resulting structures were taken using SEM (EVO MA10 microscope by Zeiss) at 14 k fold magnification for the LIPSS and 2 k-fold for the NPS. The mean distance between two peaks of the NPS respectively the periodicity of the LIPSS as well as the height and width were measured via CLSM images and evaluated via VK-X 3000 MultiFileAnalyzer by Keyence. The indentation tests were performed on a universal micro-hardness (UMH) tester Fischerscope H100C made by Helmut Fischer GmbH. The indentation hardness H_{IT} as well as the elastic indentation modulus E_{IT} were measured according to DIN EN 14577. A detailed description is to be found in [2]. The wetting behavior of the firstly plasma nitrided and subsequently structured substrates was determined via Sessile Drop tests. During these tests, a single droplet of deionized water was applied to the substrates' surfaces and the resulting contact angles (CA) were measured. Contact angles greater than 90° indicate a hydrophobic surface, contact angles smaller than 90° indicate a hydrophilic surface and contact angles smaller than 30° indicate a super hydrophilic surface. A detailed description is provided in [2].

3 Results

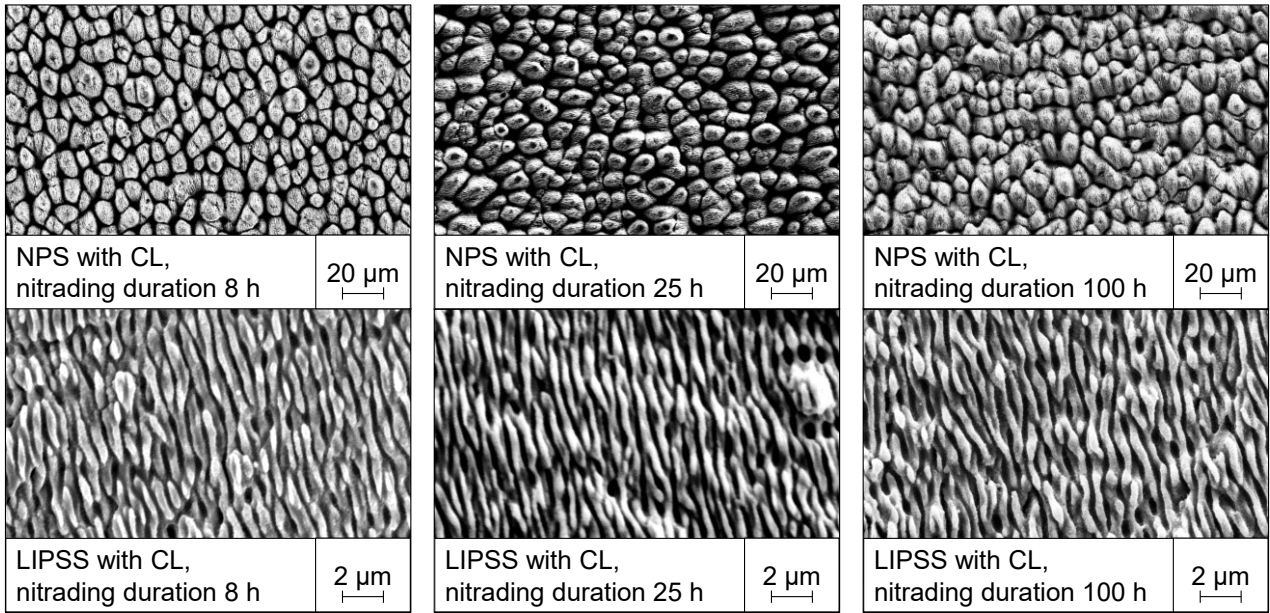
Consequently, the plasma nitrided surface was exposed to different thermal loads. Fig. 1 and Fig. 2 depict the different types of structures.



source: BIAS (Piedade) 2022

BIAS ID 220409

Fig. 1: NPS and LIPSS after structuring of plasma nitrided steels substrates without CL.



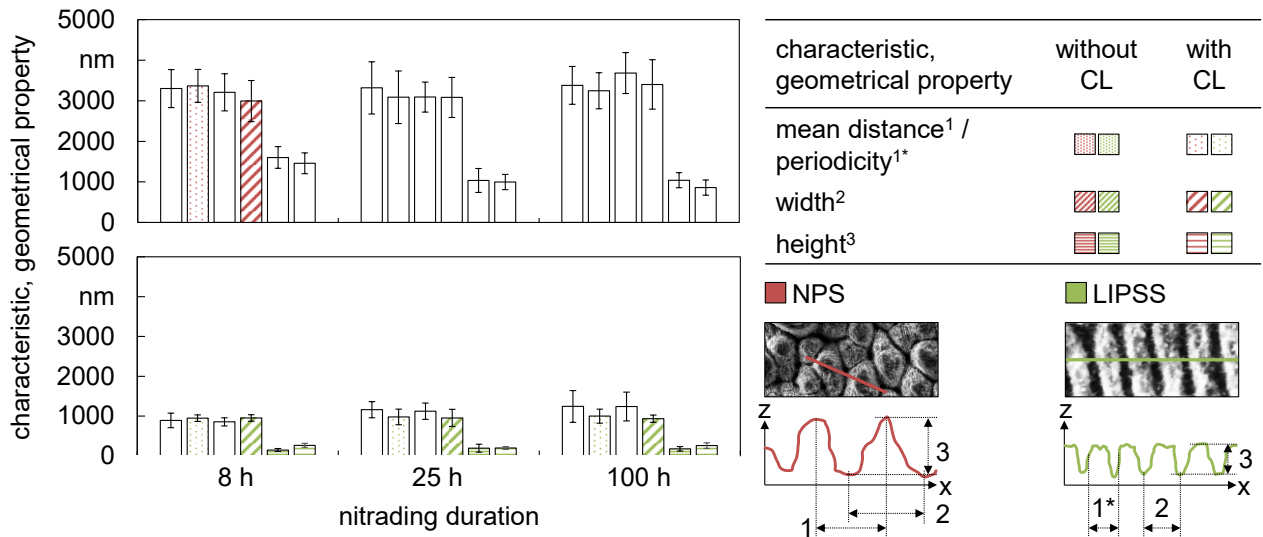
source: BIAS (Piedade) 2022

BIAS ID 220408

Fig. 2: NPS and LIPSS after structuring of plasma nitrided steels substrates with CL.

As the Fig. 1 and Fig. 2 depict, the formation of brittle compound layers with increased amounts of $\epsilon\text{-Fe}_3\text{N}$ has no visual effect on the emerging structures whether LIPSS or NPS and compared to the nitriding states without CL's. In case of the LIPSS, homogeneous and ditch-like structures occur while in case of NPS island-like structures cover the substrates' surfaces independent of the formed nitrides ($\gamma\text{'-Fe}_4\text{N}$ and $\epsilon\text{-Fe}_3\text{N}$).

The geometrical properties are summarized in Fig. 3. Since the NPS do not form homogeneous ditch-like structures, the mean distance between two peaks substitutes the periodicity in case of the NPS. As Fig. 3 depicts there is no influence on the geometric properties whether a CL is used or not. But there is an influence of the nitriding conditions on the mean distance between two peaks if NPS are applied. With increasing nitriding duration expressed through the nitriding depth, the distance between two peaks decreases slightly.

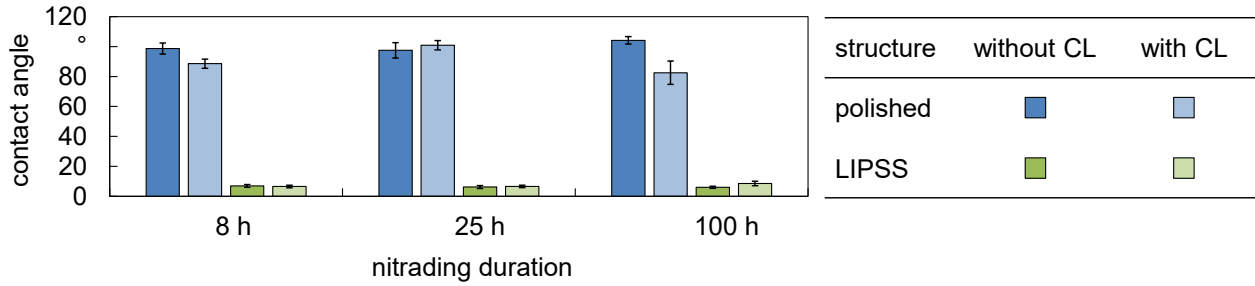


Rathmann 2022

BIAS ID 220410

Fig. 3: Characteristic and geometrical properties of the processed structures in dependency of the nitriding duration and with and without the CL.

With these geometric prerequisites, the structured substrates were examined regarding their wetting behavior. The results of the Sessile-Drop-Tests carried out are summarized in Fig. 4. The contact angle reveals that the processed surfaces covered with LIPSS have a super hydrophilic ($CA < 30^\circ$) behavior regardless of the prior nitriding conditions. Contrasting, the initial polished surface has a hydrophobic behavior according to a CA greater than 90° .

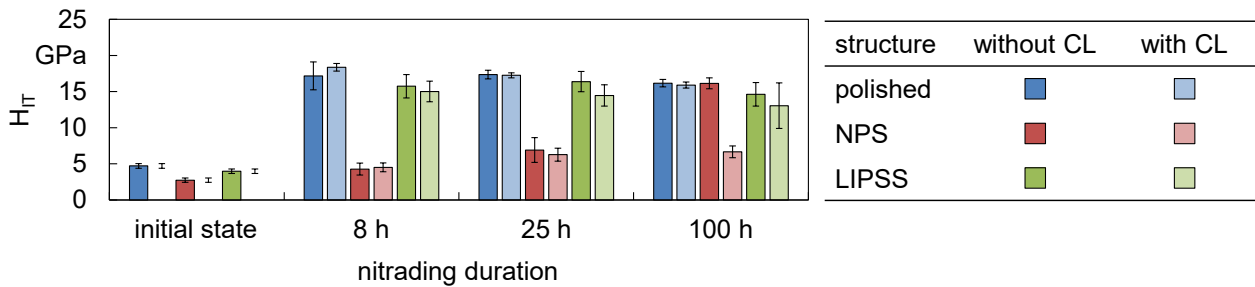


Rathmann 2022

BIAS ID 220411

Fig. 4: Contact angle on NPS and LIPSS structured in dependency of nitriding duration and with and without the CL.

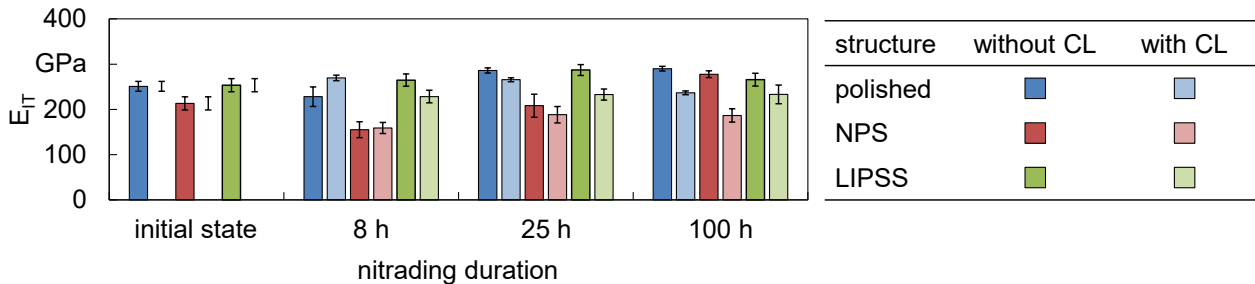
A key property to increase LIPSS' wear resistance is their hardness. Accordingly, the nitrided substrate should maintain its initial hardness during laser structuring. Therefore, the indentation hardness H_{IT} and the elastic indentation modulus E_{IT} of LIPSS were measured via nano-indentation and the results are presented in Fig. 5 and Fig. 6 in dependency of the nitriding duration and with and without CL.



source: IWT (Hasselbruch) 2022

BIAS ID 220411

Fig. 5: Indentation hardness H_{IT} in dependency of the and nitriding duration and with and without the CL.



source: IWT (Hasselbruch) 2022

BIAS ID 220411

Fig. 6: Elastic indentation modulus E_{IT} in dependency of the nitriding duration and with and without the CL.

The results of the indentation hardness in Fig. 5 depict that using NPS lead to an indentation hardness near the initial hardness of the hardened and tempered steel substrate independent of the usage of CL with one exception. At a nitriding duration of 100 h and without CL the indentation hardness of NPS is like the hardness of LIPSS and the polished and nitrided reference substrate. In contrast to the NPS, the appliance of LIPSS leads only to a negligible decrease in the indentation hardness compared to the polished and nitrided reference substrate independent of the usage of CL. The indentation modulus shows an influence of the CL with increasing nitriding depth. At durations of 8 h no influence can be seen. But at durations of 100 h, the formed CL leads to lower elastic indentation moduli. Overall nitriding depths, substrates structured with LIPSS lead to higher moduli compared to NPS-structured substrates. Those moduli achieved with LIPSS lie in the range of those moduli of hardened and tempered substrates without any surface structure.

4 Discussion

Concerning the elastic indentation modulus in Fig. 6, it is observed that except the combination of NPS and a nitriding depth of 0.05 mm no significant deviation from the initial indentation modulus of the hardened and tempered steel substrate is to be recognized. Since there is no significant deviation of the indentation hardness in terms of LIPSS for different nitriding depths, these hardnesses are averaged to a mean indentation hardness of $14.88 \text{ GPa} \pm 1.05 \text{ GPa}$. Compared to those hardnesses achieved by different processes like combing PVD hard coatings with LIPSS (DLC: $6.24 \text{ GPa} \pm 1.05 \text{ GPa}$, TiN_x : $4.94 \text{ GPa} \pm 0.94 \text{ GPa}$) [2] and laser hardening

of LIPSS ($5.66 \text{ GPa} \pm 1.93$) [3], it becomes clear that the combination of firstly nitriding a surface and subsequently structuring with LIPSS leads to a three times higher indentation hardness. Simultaneously, the hydrophilic and even super hydrophilic property of with LIPSS structured surfaces could be maintained. A nitrided surface structured with LIPSS has a 22 times respectively 21 times lower contact angle than a DLC ($155^\circ \pm 2$) respectively a TiN_x coating ($146^\circ \pm 2^\circ$) structured with LIPSS [2] or a 9 times lower contact angle than laser hardened LIPSS ($62 \pm 2^\circ$) [3]. This work thus demonstrates the suitability of firstly nitrided and subsequently with LIPSS structured substrates in principle for tribological applications. This is because, on the one hand, a high nano-hardness is present in the case of LIPSS and, on the other hand, the hydrophilic behavior is retained. In the following, wear tests will be carried out to further quantify their suitability.

5 Conclusion

In this work were firstly nitrided surfaces combined with LIPSS and NPS to obtain hard and simultaneously hydrophile surface structures for tribological applications. As the results indicate, LIPSS maintain the hardness of the nitrided substrate and the hydrophilicity in contrast to NPS. Therefore, it is concluded that a previous nitriding could bring LIPSS into tribological applications since it settles the right prerequisites regarding nano-hardness and wetting behavior.

Acknowledgements

Funding by the Deutsche Forschungsgemeinschaft DFG (project 416530419 „Wasser als Schmierstoff für die Hochgeschwindigkeitsumformung mithilfe von LIPSS“) is gratefully acknowledged.

References

- [1] L. Rathmann, T. Radel: Influence of laser hardening on laser induced periodic surface structures on steel substrates. *IOP Conference Series: Materials Science and Engineering* 1135 (2021) 0120245. <https://doi.org/10.1088/1757-899X/1135/1/012024>
- [2] L. Rathmann, T. Rusche, H. Hasselbruch, A. Mehner, T. Radel: Friction and wear characterization of LIPSS and TiN / DLC variants. *Applied Surface Science* 584 (2022) 152654. <https://doi.org/10.1016/j.apsusc.2022.152654>
- [3] L. Rathmann, T. Radel: On the use of LIPSS in single- and multi-scale laser-structured tool surfaces under lubricated conditions. *Journal of Manufacturing Processes* 77 (2022) 819-830. <https://doi.org/10.1016/j.jmapro.2022.03.049>
- [4] H. Hasselbruch, A. Mehner, H.-W. Zoch: Influence of plasma nitriding parameters and subsequent surface finishing on the adhesion strength of tungsten doped PVD a-C:H coatings. In: *THE "A" Coatings in Manufacturing Engineering* (Ed.): Proceedings of the 13th International Conference of THE "A" Coatings, (2017) 169-179.
- [5] H. Hasselbruch, A. Mehner, H.-W. Zoch: Einfluss der Plasmanitrierparameter und anschließenden Oberflächenveredelung auf die Haftfestigkeit von Wolfram dotierten PVD-a-C:H-Schichtsystemen. In: *Gesellschaft für Tribologie e.V. (GfT) (Ed.): 58. Tribologie-Fachtagung (2017) 1-11.*
- [6] H. Hasselbruch, M. Herrmann, J. Heidhoff, et al.: Strukturierte und DUPLEX behandelte Werkzeuge für die Trockenbearbeitung beim Rundkneten. *Dry Metal Forming OAJ FMT 5* (2019) 31-38.

Laser micro structuring of multi-layer coatings on aircraft splines for optimization of the surface properties

Andreas Stephen*¹ , Bastian Lenz², Gerrit Hellenbrand³

¹ BIAS – Bremer Institut für angewandte Strahltechnik GmbH, Klagefurter Str. 5, 28359 Bremen, Germany

² Leibniz-Institut für Werkstofforientierte Technologien, Badgasteiner Str. 3, 28359 Bremen, Germany

³ Laboratory of Machine Tools and Production Engineering (WZL) of RWTH Aachen University, Steinbachstr. 19, 52074 Aachen, Germany

Abstract

In the aircraft industry spline-joints are used for the connection of subassemblies in geared turbofans. Besides the power transmission, spline-joints are used to compensate deviations in the shaft system, such as angular or axial misalignments. By decoupling the subassemblies, constraining forces are reduced, which affects the dimensioning of the surrounding components. Increasing the load capacity of spline-joints enables a lean and efficient design of the components. The wear behavior of such heavily loaded splines can be improved by multi-layered coatings deposited e. g. by physical vapor deposition (PVD). Further improvements can be realized by an additional laser structured surface topology, which includes an arrangement of semi-spheres in the coating system with diameters in the micrometer range. These semi-spheres can either serve as a micro pocket for lubrications or are applied before the final coating step to be replenished with a hard lubricant layer. This paper addresses this subject by presenting the manufacturing process of splines with focus on the laser texturing process.

Keywords: Laser micro structuring, PVD-coatings, Wear behavior

1 Introduction

To connect subassemblies and to transmit high torque, spline-joints are used in powertrain technology [1]. Spline-joints are furthermore used in modern aero-engine-turbines to connect shaft systems and compensate shaft misalignments [2]. This enables to raise potentials according to the required packaging volume and components weight of the whole system, which leads to an increasing power density. Overall, manufacturing costs can be cut because of a reduced need of material and the system efficiency is increased, while simultaneously the system emissions are decreased due to reduced inertia [3]. Due to the compensation of the misalignment of the shaft systems, a sliding velocity is generated in the spline-joint contact between the teeth of the spline-shaft and -hub. Therefore, the risk of upcoming wear and fatigue phenomena is raised on the tooth flanks [4]. To minimize wear effects and raise the load carrying capacity of spline-joints, new optimized surface treatments are developed, see Fig. 1.

In a first step, Stephen et. al. has developed possible surface treatments for the optimization of the load carrying capacity of spline-joints [5]. Different coatings have been selected for the upcoming full scale spline testing. Therefore, TiN + MoS₂:Ti and TiN + DLC + MoS:Ti:C multi-layered coatings are manufactured by physical vapor deposition (PVD). Additionally, a laser structuring process is applied, where dimple textures are manufactured on the tooth flanks [5]. As known, surface texturing is an effective way of improving tribological properties under both dry and lubricated conditions [6]. Its main effect mechanisms are to trap wear particles, store lubricants, and increase load carrying capacity [7].

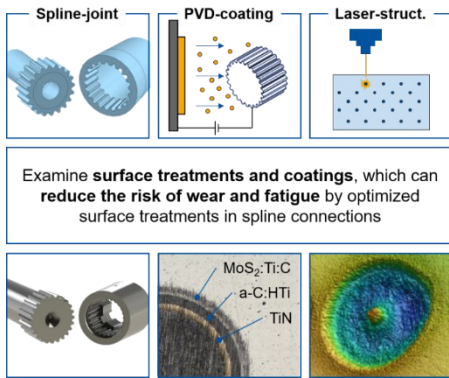
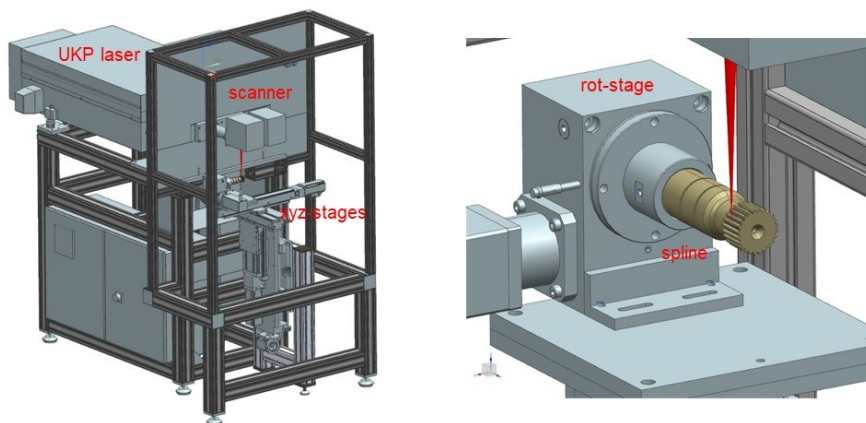


Fig. 1: Manufacturing steps for high-loaded splines for aerospace applications in fan-turbines

Nevertheless, the influence of texturing parameters, like dimple diameter and density, spatial arrangement and aspect ratio on friction forces is not explicitly known at all, as it depends on many different conditions of the tribological system. Variations of the dimple diameter showed that there is an optimum in the dimple diameter and that this optimum depends on the oil viscosity and the velocity gradient along the contact area [8]. The aspect ratio [9] and the textured area [10] widely influence the tribological properties of the texturing. Besides structuring, hard coatings are used to increase the wear resistance, e.g., multi-layer PVD coatings. Especially, in case of aircraft applications for turbine engines, high contact pressures of more than 1 GPa and a partially lubrication lost due to air holes while flying occur. Therefore, in defined multi-layer systems with respect to the diameter of the structured dimples and their density also should be of most importance to improve the tribological properties according to decreasing friction and wear.

2 Method

An ultrashort pulse laser with a wavelength of 1030 nm was used as the laser beam source for structuring the multi-layer systems. The laser used (Trumpf TruMicro 5050) has a pulse length of less than 10 ps with a maximum output power of 50 W and a pulse repetition rate of 200 kHz. The laser beam was guided over the workpiece by a Galvano scanner with a focus diameter of 40 μm . The spline was clamped into a rotational stage mounted on xyz-stages for positioning, see Fig. 2. The laser texturing by the scanner after positioning was performed without a protective gas supply. Applied to the multi-layer systems were four different textures varying the dimple diameter and the dimple density. The dimple diameter is indicated as d with a pitch a hexagonally orientated leading to a dimple density of A , i.e., the percentage of surface area covered by dimples, see Fig. 3.

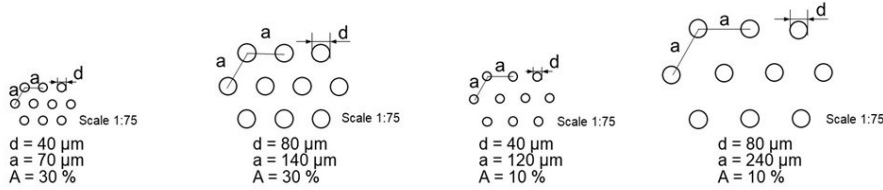


Stephen 2021

BIAS ID 210236

Fig. 2: Machining system (left) and detailed view of the spline machining arrangement (right)

Based on the chosen coating designs and laser structuring parameters, a full factorial design of experiments (DoE) was applied to systematically analyze the effect of the input factors [5]. These factors are the dimple diameter, the remaining coating coverage, the coating system, and the process design. On the last point, structuring of all coating layers is compared to structuring of only the hard coating layer (TiN/a-C:H:Ti) and subsequent application of the solid lubricant. One example from the full factorial design applied to splines will be discussed in the following.



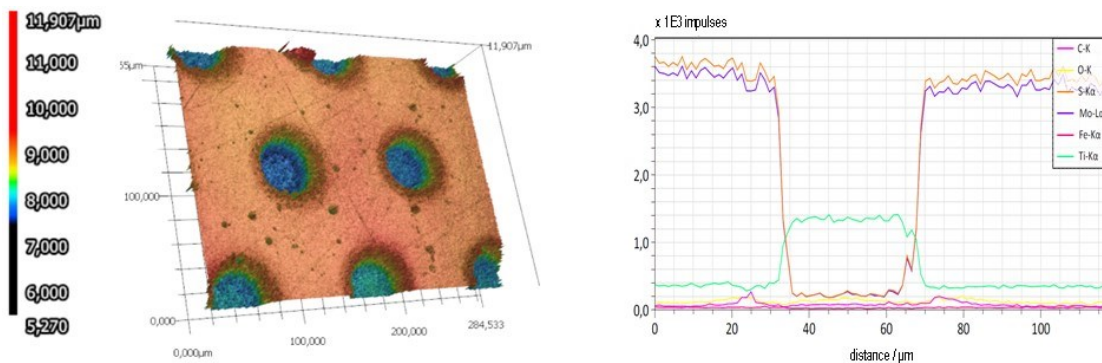
Stephen 2021

BIAS ID 210237

Fig. 3: Different textures defined for the laser structuring

3 Results and discussion

A corresponding laser confocal microscope image and an EDX analysis of a multi-layer system consisting of TiN + MoS₂:Ti applying a dimple diameter of 40 μm and a dimple density of 10 % are shown in Fig. 4. The 3-dimensional measurements indicate a constant depth of 1 μm for all measured micro dimples, see Fig. 4 (left). This results by choosing a suitable laser pulse energy (5 μJ) and pulse repetition rate (50 kHz), that the ablation could be set in such a way that the MoS₂:Ti layer on top was removed which have a depth of 1 μm . Furthermore, the underlying layers retained on the substrate as proved by EDX analysis also shown in Fig. 4 (right). This is indicated by the fact that the Mo and S signals decrease nearly completely whereas that of Ti increases inside of the dimple. The number of applied scans for processing was 5 at a constant speed of 250 mm/s. The depth can be reproducibly set with an absolute deviation of less than 0.2 μm . The evenness of the dimples is in the range of $\pm 0.1 \mu\text{m}$. Almost no burr formation or melt residues are observed.



Stephen 2021

BIAS ID 210239

Fig. 4: Laser Confocal Microscopy and EDX analysis of an laser structured multi-layer system (TiN + MoS₂:Ti; $d = 40 \mu\text{m}$, $A = 10\%$)

The process development and analysis were performed on flat discs with structure dimensions of 20 mm times 20 mm for enabling pin-on-disc test to evaluate the surface properties regarding friction and wear behavior. A challenge for laser texturing of the splines is the more complex geometry, i. e. curved surface on the partially shadowed flank, see Fig. 5. Therefore, a precise adjustment of the laser beam in lateral and axial position must be realized to ensure an almost perpendicular incidence of the laser beam deeply on the flank side as shown in Fig. 5 (right). The individual 24 left- and right-handed flanks are textured using a fixed laser beam position and precisely rotating, respectively laterally moving the spline into the correct position after finalizing each flank itself. Indeed, the focal position must be identical for each flank and concentrically located in the flank taking the Rayleigh length of the laser beam into account.

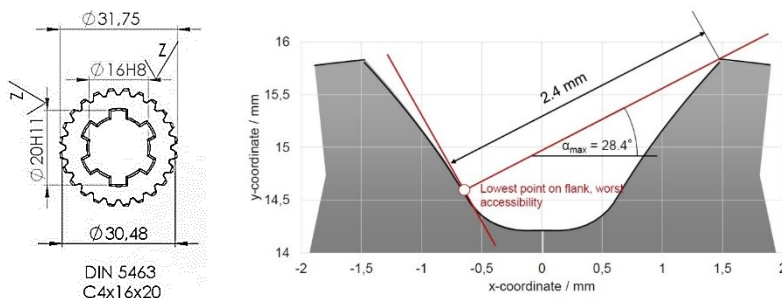


Fig. 5: Geometry of the splines in cross-sectional view (left) and necessary incidence of the laser beam (right)

Applying such a texturing strategy using the developed processing technology the complete spline flanks can be evenly machined. Depending on the size and density of dimples the splines are covered with 25,000 to more than 100,000 dimple structures in less than 1 hour machining time. Indeed, the bottom of a flank will not be textured, and the top is slightly influenced by the touching laser beam, see Fig. 6. However, these areas are not affected by high loads and therefore not critical for the friction and wear behavior.

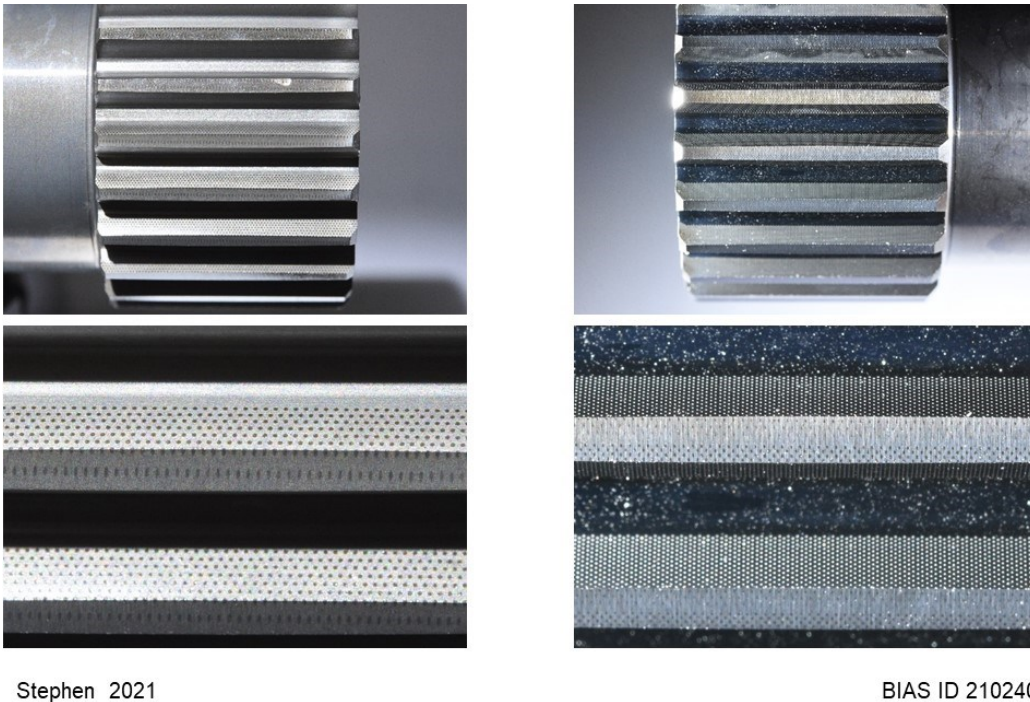


Fig. 6: Textured splines overall view and in magnified detail: left: $d = 80 \mu\text{m}$, $A = 10\%$, right $d = 40 \mu\text{m}$, $A = 10\%$

4 Conclusion

The manufacturing process focused on a laser texturing step for surface optimized spline-joints has been presented. The spline has been manufactured within a conventional process chain, which is likely to be used in aero-gear-applications. The innovation is the combination of laser and PVD processes suitable to perform on splines obtaining a surface modification which can be applied for highest contact pressure applications.

Acknowledgements

The authors thank the support from the Clean Sky 2 initiative within the framework of the Horizon 2020 program of the European Union (GA no. 821344).



Horizon 2020
European Union Funding
for Research & Innovation

References

- [1] C.H. Wink, M. Nakandakar: Influence of Gear Loads on Spline Couplings. *Power transmission Engineering* (2014) 42–49.
- [2] J. Ding, I.R. McColl, S.B. Leen: The application of fretting wear modelling to a spline coupling. *Wear* 262/9-10 (2007) 1205–1216.
- [3] H.E. Friedrich, S.K. Krishnamoorthy: *Leichtbau als Treiber von Innovationen. Leichtbau in der Fahrzeugtechnik*. Springer (2017) 1–31.
- [4] F. Curà, A. Mura, S. Ugarte, P. Saenz: Recent Advances in Spline Couplings Reliability. *Proc. Structural Integrity* 19 (2019) 328–335.
- [5] A. Stephen, B. Lenz, A. Mehner, T. Radel: Laser structuring of PVD multi-layer systems for wear reduction. *Lasers in Manufacturing* (2021).
- [6] Z. Wu, J.X. Deng, Y. Chen, Y.Q. Xing, J. Zhao: Performance of the self-lubricating textured tools in dry cutting of Ti-6Al-4V. *Int. J. Adv. Manu. Technol.* 62 (2012) 943–951.
- [7] Y.Q. Xing, J.X. Deng, Z. Wu, H.W. Cheng: Effect of regular surface textures generated by laser on tribological behavior of Si₃N₄/TiC ceramic. *Appl. Surf. Sci.* 265 (2013) 823–832.
- [8] C. Greiner, T. Merz, D. Braun, A. Codrignani, F. Magagnato: Optimum dimple diameter for friction reduction with laser surface texturing: The effect of velocity gradient. *Surf. Topogr. Metrol. Prop.* 3 (2015) 044001.
- [9] A. Shinkarenko, Y. Kligerman, I. Etsion: The effect of elastomer surface texturing in soft elasto-hydrodynamic lubrication. *Tribol. Lett.* 36 (2009) 95–103.
- [10] X.L. Wang, K. Kato, K. Adachi, K. Aizawa: The effect of laser texturing of sic surface on the critical load for transition of water lubrication mode from hydrodynamic to mixed. *Tribol. Int.* 34 (2001) 703–711.

Influence of electrolyte concentration on laser chemical machining

Marcel Simons*¹, Tim Radel¹ 

¹ BIAS – Bremer Institut für angewandte Strahltechnik GmbH, Klagenfurter Str. 5, 28359 Bremen

Abstract

To meet the increasing trend of miniaturization, new (non-conventional) manufacturing processes are constantly being developed. The laser chemical process describes one of these non-conventional removal processes in the microscale, based on the thermochemical dissolution of metals. To determine the influence of electrolyte concentrations, linear cavities were created in Titanium Grade 1 using phosphoric acid and sulfuric acid with different concentrations. The experimental results show that as the electrolyte concentration increases, the process window is reduced. One possibility for this is, as the electrolyte concentration increases, the viscosity increases, as well. With increasing viscosity, the electrolyte boiling process, which causes the shielding effect of the gas bubbles becomes more significant. Due to the increasing conductivity of the electrolyte at higher concentrations, the laser chemical removal rate increases within the process window at constant laser power. The maximum removal rate is observed at the maximum conductivity of the electrolyte.

Keywords: micromachining, shielding effect, boiling

1 Introduction

The laser chemical process is a non-conventional removal process based on the thermo-chemical dissolution of metals. The laser chemical process links the advantages of laser processing with selective energy input and the advantages of electro chemical machining with a gentle removal process [1].

During laser chemical machining, the workpiece is embedded in an etching cell and irradiated with a laser beam. This introduces heat locally into the workpiece. The introduced temperature gradient starts an anodic material dissolution [2]. Within a suitable process window, this enables gentle material removal without a heat-affected zone and without changing the microstructure. This advantage opens up a wide range of applications for laser chemical machining. For example, materials such as Inconel, which is costly to machine using conventional machining methods, can be processed [3]. Furthermore, the laser chemical process allows a selective and specific adjustment of the surface roughness [4].

However, the machining temperature of the laser chemical process is above the boiling point of the electrolyte [2], resulting in an electrolyte boiling process. The resulting boiling bubbles shield the surface, which results in disturbed material removal. This restricts the laser chemical process window and, consequently, the removal rate. To reduce this limitation, the process can be performed at higher process pressures [5]. This reduced electrolyte boiling and enables thereby higher laser chemical removal rates.

Furthermore, an influence of the electrolyte viscosity by the admixture of the additive PEG (polyethylene glycol) could be determined [6]. With increasing admixture of PEG and thus with increased viscosity, a reduction of the process window was observed. In order to investigate the influence of viscosity in more detail, without the addition of an additive, the influence of varying electrolyte concentrations on the process window and the removal rates was investigated in the present work.

2 Methods

A cw fiber laser from the company IPG (YLR-AC100) with a wavelength of 1070 nm was used for the experimental investigations. With the help of a beam attenuator built into the beam path, the laser power was controlled in 0.1 W steps. The beam was guided by an optical fiber with a fiber core diameter of 10 μm . The laser beam was collimated by a collimator and then focused by a lens from “Qioptiq” with a focal length of 93 mm. This resulted in a spot diameter of 25 μm .

Based on preliminary investigations, the electrolytes phosphoric acid and sulfuric acid were used [7]. The concentration of Phosphoric acid was varied from 1 mol/L to 10 mol/L in 1 mol/L steps. The concentration of sulfuric acid was varied between 1 mol/L and 5 mol/L also in 1 mol/L steps.

Prior laser chemical machining, the Titanium Grade 1 samples were fabricated to a size of 20 mm x 20 mm x 1 mm and ground to ensure uniform surface roughness. The fabricated samples were embedded in a chemical cell, see Fig. 1, which was flushed with the particular electrolyte. The propagation height was 46 mm, resulting in a transmission of 0.44.

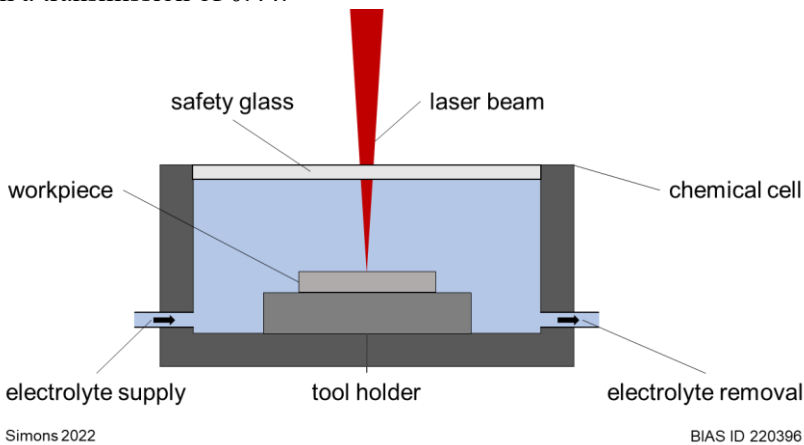


Fig. 1: Schematic depiction of the laser chemical experimental set-up

Linear cavities with a length of 2 mm were fabricated using the set-up described. The evaluation of the fabricated cavities was performed by confocal microscopy. To determine the quality of the laser chemical generated cavities and thus to determine the process window, the respective removal cavities were divided into three categories, depending on the profile of the cavities, according [8]:

Category I (no material removal): No material removal deeper than 0.5 μm is detectable. The laser-induced surface temperatures within the laser chemical interaction zone are lower than the activation temperature at which the passive layer dissolves locally.

Category II (undisturbed material removal): Continuous material removal occurs along the feed direction. This is characterized by a Gaussian profile of the removed material. Within the removal path, there are no material residues or interruptions of the laser chemical material removal. In addition, a lower surface roughness is measurable within the cavity compared to unmachined surfaces.

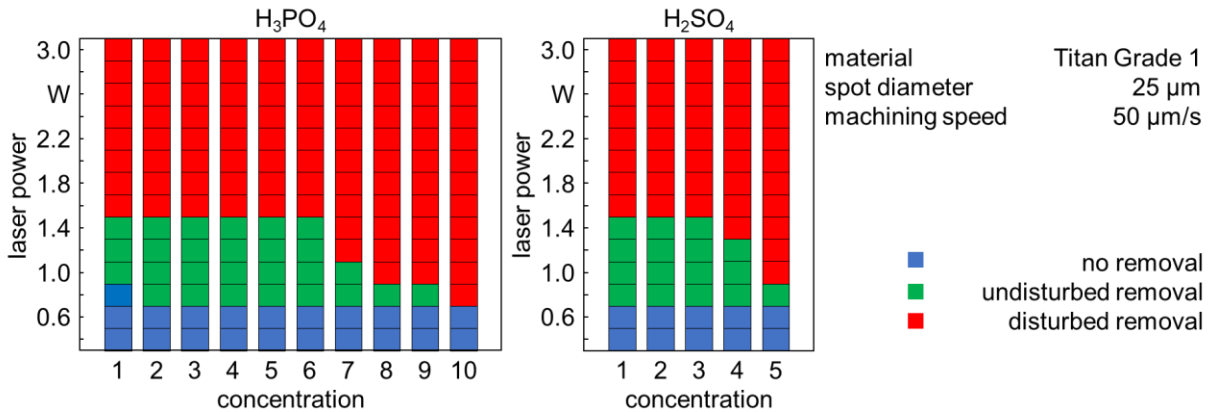
Category III (disturbed material removal): Characterized by deviating non-Gaussian removal characteristics of the surface. Within the cavity, material residues and interruptions of the removal path are visible. In addition, the cross-sectional profile shows a W-shaped material removal. The cavities are characterized by a very uneven and furrowed surface, which is accompanied by a higher surface roughness than category II material removal. In addition, it is noticeable that the width of the generated cavities is several times larger than the width of category II cavities and also larger than the laser spot diameter.

The removal rates were determined analogously to [8].

3 Results

Fig. 2 shows the process window for laser chemical machining with phosphoric acid and sulfuric acid at varying electrolyte concentrations. For both electrolytes, it should be noted that the process window becomes smaller at higher electrolyte concentrations. In addition, it should be mentioned that at a concentration of

1 mol/L phosphoric acid and an applied laser power of 0.8 W, in contrast to all other electrolyte concentrations used, no removal could be detected.

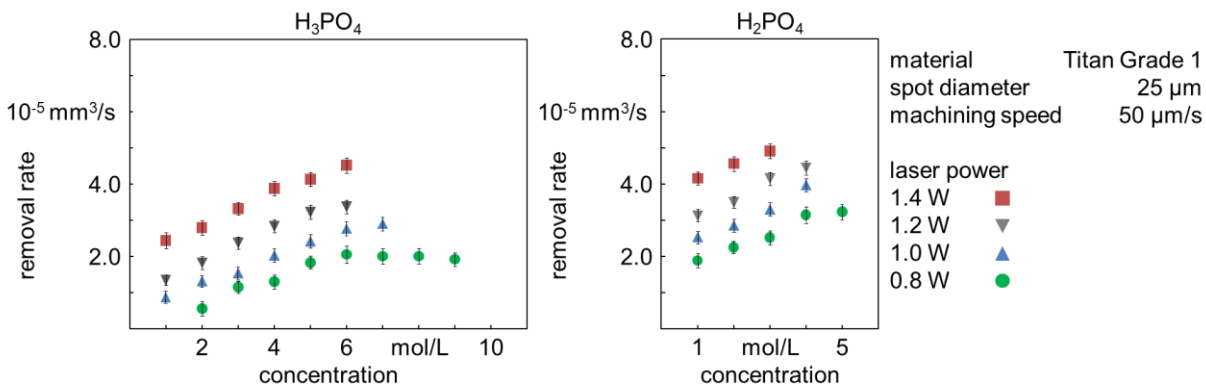


Simons 2022

BIAS ID 220397

Fig. 2: Process window of laser chemical machining with phosphoric acid and sulfuric acid

In addition to the process window, Fig. 3 shows the removal rates within the process window (marked green in Fig. 2). It can be seen that the removal rates initially increase. At a concentration of 6 mol/L, the maximum removal rate could be achieved for laser chemical machining of phosphoric acid with constant applied laser power of 0.8 W. For laser chemical machining with sulfuric acid at constant applied laser power, the maximum removal rate was obtained at a laser power of 5 mol/L.



Simons 2022

BIAS ID 220398

Fig. 3: Laser chemical removal rates within the process window for laser chemical machining with phosphoric acid and sulfuric acid

4 Discussion

Based on the experimental data, it can be seen that the process window of laser chemical machining reduces at higher electrolyte concentrations, compare Fig. 2. When increasing the electrolyte concentration, there are two opposing mechanisms.

On the one hand, as the electrolyte concentration increases, the boiling points of the electrolytes become elevated [9]. This can be attributed to the fact that increasing the concentration decreases the vapor pressure. Therefore, a higher temperature is required to reach the boiling point [10]. The electrolyte boiling process during laser chemical machining was identified as limiting the laser chemical process window [8]. The gas bubble diameters and the adhesion times of the gas bubbles to the workpiece surface could be determined as critical parameters of the electrolyte boiling process [2]. When the electrolyte boiling temperature is increased, the gas bubble diameters and adhesion times of the gas bubbles to the workpiece surface decrease. This effect could already be observed in [5]. Here, the electrolyte boiling point was increased by increasing the process pressure. As a results, the smaller gas bubble diameters and shorter adhesion times were detected while the applied laser power remained constant. Based on this finding, the laser chemical process window could be extended. However, based on the experimental investigations, it can be stated that no enlargement of the process window takes place at increased viscosities. On the contrary the process window is reduced at higher electrolyte concentrations. Thus, another mechanism predominates over this one.

On the other hand, the viscosities of the electrolytes increase due to an increase in the electrolyte concentration [11]. The increase of the electrolyte viscosity leads to an increased characteristic of the electrolyte boiling process [8]. Due to the increasing gas bubble diameters and adhesion times of the gas bubbles to the workpiece surface, the shielding effect of the gas bubbles comes in effect. This reduces the process window at higher electrolyte viscosities. Based on the reducing process window at higher concentrations of both phosphoric acid and sulfuric acid, it can be observed that this mechanism dominates compared to the increase of the electrolyte boiling temperature.

Considering the removal rates at a constant applied laser power, an increase of the removal rates with increasing electrolyte concentration can be observed at first. Fig. 4 shows the removal rates achieved during laser chemical machining with phosphoric acid and sulfuric acid as well as the conductivities of both electrolytes [12], [13]. It can be seen that with increasing conductivity, the laser chemical removal rate increases. If the conductivity decreases, a decrease in the removal rate can be observed, especially for laser chemical machining with phosphoric acid.

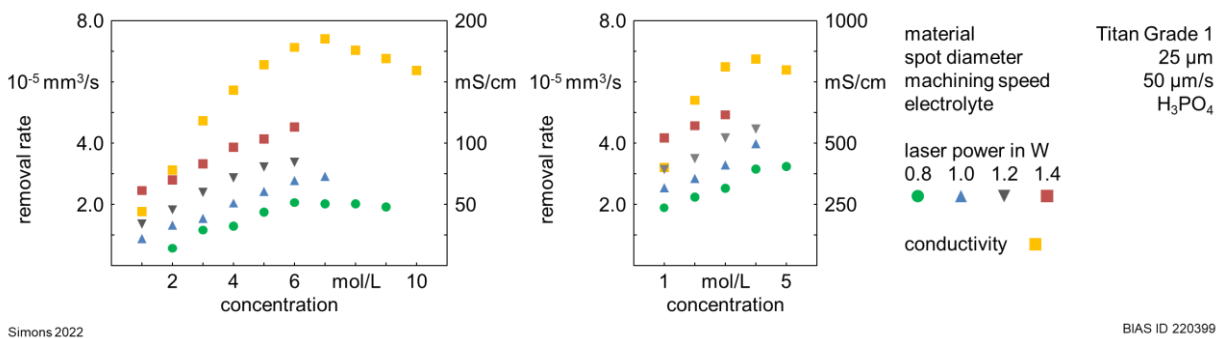


Fig. 4: Laser chemical removal rates and conductivities of the electrolytes phosphoric acid [12] and sulfuric acid [13]

At a concentration of about ca. 7 mol/L and 4 mol/L, respectively, the electrolytes phosphoric acid and sulfuric acid reach the maximum conductivity. Up to these concentrations, an increase in the removal rates during machining with phosphoric acid can be identified. At higher electrolyte concentrations, which do not reach the maximum conductivity a decrease in the removal rates can be observed. Therefore, the removal rate seems to correlate with the conductivity of the electrolyte.

5 Conclusion

Based on the present investigations, it can be stated that the dominant mechanism in an increase of the electrolyte concentration regarding the process window limitation during laser chemical machining is the increase of the viscosity in contrast to an increase of the electrolyte boiling point. The maximum removal rate is observed at the maximum conductivity of the electrolyte.

Acknowledgements

This work has been funded by the Project 451385285 – “Prozessnahe Charakterisierung der Temperaturfeld- und Abtragsveränderung bei der laserchemischen Bearbeitung“ and the transregional collaborative Research Program SFB/TRR 136 „Funktionsorientierte Fertigung auf Basis charakteristischer Prozesssignaturen“ sub project F07 Project 223500200. The authors gratefully acknowledge the financial support by the Deutsche Forschungsgemeinschaft.

References

- [1] Bäuerle, D.: Etching of Metals and Insulators Laser Processing and Chemistry. 4th Edition, Springer Verlag (2011)
- [2] Messaoudi, H.: Thermische Bedingungen der laserchemischen Mikrobearbeitung von Metallen. Strahltechnik Band 70, BIAS Verlag: Bremen (2020)
- [3] Simons, M., Beste, L.-H., Radel, T.: Laserchemie Mikrobearbeitung von Inconel 718. Mikroproduktion 10, 3, 26-27 (2021)
- [4] Eckert, S, Vollertsen, F.: Prozessbeschleunigung beim laserchemischen Polieren. Laser Magazin 2, 20-22 (2020).
- [5] Simons, M., Shanta, V., Radel, T., Vollertsen, F.: Bubble behavior during laser chemical machining under superatmospheric pressure. Proc. of the 11th CIRP Conference on Photonic Technologies (LANE2020) (2020), eds.: M. Schmidt, F. Vollertsen, E. Govekar. Procedia CIRP 94, Elsevier B.V. Amsterdam (2020), 561-564
- [6] Simons, M., Radel, T.: Laser chemical machining with additive-increased electrolyte viscosity. Proc. 23rd Int. Symposium on Laser Precision Microfabrication (LPM2022) (2022)
- [7] Stephen, A., Vollertsen, F.: Mechanisms and processing limits in laser thermochemical machining. CIRP Annals 59, 1 (2010), 251-254

- [8] Mehrafsun, S.: Dynamisches Prozessverhalten bei der laserinduzierten thermochemischen Mikrostrukturierung von Metallen. Strahltechnik Band 67 (2018)
- [9] Peyghambarzadeh, S.M. Hatami, A., Ebrahimi, A., Alavi Fazel, S.A.: Photographic study of bubble departure diameter in saturated pool boiling to electrolyte solutions. Chem. Ind. Chem. Eng. 20, 1, 143-153 (2014)
- [10] anonymous: Properties of Solutions, chemistry LibreTexts, online available: [https://chem.libretexts.org/Bookshelves/Introductory_Chemistry/Basics_of_General_Organic_and_Biological_Chemistry_\(Ball_et_al.\)/09%3A_Solutions/9.04%3A_Properties_of_Solutions](https://chem.libretexts.org/Bookshelves/Introductory_Chemistry/Basics_of_General_Organic_and_Biological_Chemistry_(Ball_et_al.)/09%3A_Solutions/9.04%3A_Properties_of_Solutions); accessed date: 11.08.2022
- [11] Goldsack, D.E.; Franchetto, R.: The viscosity of concentrated electrolyte solutions. Can. J. Chem. 55, 1062-1072 (1977)
- [12] Machorro, J.J., Olvera, J.C., Larios, A., Hernandez-Hernandez, H.M., Alcantara-Garduno, M.E., Orozco, G.: Electrodialysis of Phosphates in Industrial-Grade Phosphoric Acid. ISRN Electrochemistry, 865727 (2013)
- [13] anonymous: Instrumentation – Acid Concentration, DKL Engineering Inc., online available at: http://www.sulphuric-acid.com/techmanual/Instrumentation/instr_acidconc.htm; accessed date: 11.08.2022

Macro-pore free sub-surface PBF-LB/M components through laser polishing

L. Rathmann*¹ , L.H. Beste¹, P.J. Faue², B. Richter², K. Klingbeil³, F.E. Pfefferkorn², T. Radel¹ 

¹BIAS – Bremer Institut für angewandte Strahltechnik GmbH, Klagenfurter Str. 5, 28359 Bremen Deutschland

²University of Wisconsin – Madison, 1513 University Ave, Madison, 53706, USA

³Cross Product Solutions, LLC, 780 218th Street, Osceola, 54020, USA

Abstract

Despite notable improvements in the laser-based powder bed fusion of metals (PBF-LB/M) in recent years, residual porosity is still an issue. Near surface pores can affect the functional properties of PBF components, such as their fatigue life, yield strength, or corrosion behavior. To help address the challenge, this work shows that laser polishing decreases the surface roughness while also creating a highly dense sub-surface region of PBF parts with only microscale pores remaining.

Keywords: Laser beam machining, polishing, metals, pores

1 Introduction

High process related design flexibility of metal components is one of the key characteristics of laser-based powder bed fusion. These components find applications ranging from medical technologies, aerospace segments, and more. However, despite the advantages of the process, PBF-LB/M parts face challenges in terms of surface quality based on surface roughness and pores close to or connected to the parts' surface. Near surface pores can affect the functional properties of the components, such as fatigue life, yield strength, or corrosion behavior. These pores have various formation mechanisms like dissolved gas porosity, residual porosity within powder, lack-of-fusion porosity due to processing, spatter induced lack-of-fusion porosity and keyhole porosity [1]. A porosity of 1 % according to the Archimedes method decreased the fatigue limit of Ti6Al4V down to 100 MPa from an initial value of 350 MPa at nearly 0 % porosity [2]. When it comes to the surface roughness of PBF-LB/M parts, the resulting surface roughness is commonly smoothed using conventional, mechanical processes such as sand blasting. Liang et al. [3] demonstrated that ns-pulsed laser polishing is capable of simultaneously reducing the surface roughness while also decreasing the porosity of Ti6Al4V. Panov et al. showed a decrease in porosity of 90 % due to cw-laser remelting of PBF 316L which is also referred as pore healing or densification [4]. These results confirm the findings of Yasa et al. [5].

To further understand the mechanism of reducing the near-surface porosity of PBF-LB/M parts made of Co-Cr with a focus on micropores, this work studied cw-laser polishing as a post processing technique for PBF-LB/M specimen and analyzed the porosity size distribution following polishing.

2 Methods

The PBF-LB/M specimens (10 mm x 10 mm x 4 mm) were printed using a TruPrint 1000 by Trumpf with Celsit-21P (Co-Cr-alloy) powder. The PBF-LB/M build process used a laser power of 120 W and a scanning velocity of 900 mm/s. The hatching distance was set to 50 μm while the layer thickness was 20 μm . The post-process laser polishing used a JK 400 fiber laser with a circular beam and a gaussian intensity profile. Polishing was performed with a laser power of 35 W, scanning velocity of 120 mm/s, and variable path overlap percentage. The specimens were shielded with Argon gas to prevent chemical reactions during processing. The pores and their position were examined in cross sections perpendicular to the scanning direction using scanning

© 2022 The Authors. Published under responsibility of BIAS - Bremer Institut für angewandte Strahltechnik GmbH.

*E-mail address of corresponding author: rathmann@bias.de

electron microscopy (SEM). Since different hatch spacings i.e., overlapping degrees of the scanning paths were chosen parts of the scanning paths, were remelted different number of times, as Fig. 1 depicts.

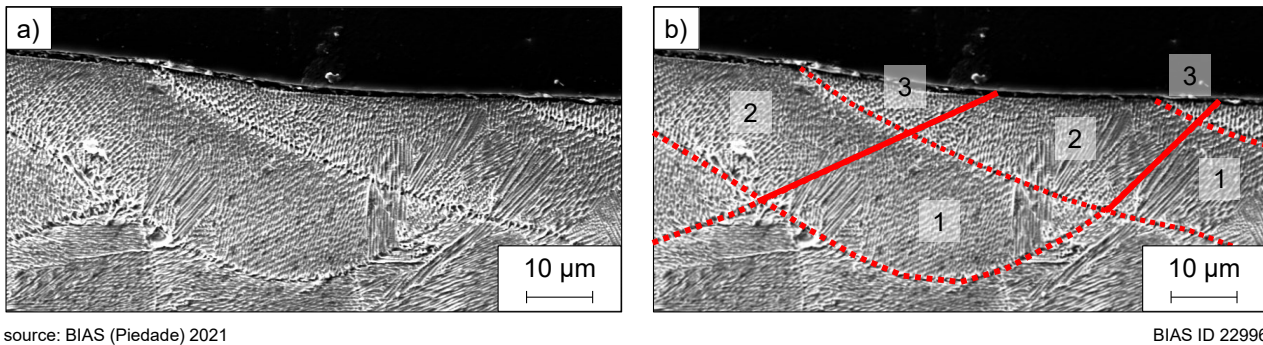


Fig. 1: a) Cross-sectional SEM image and b) visible melt line marked as red dashed line and extrapolation of former melt lines marked as red solid line. Numbers indicate the number of remelting events.

The horizontal position of a pore was defined as the smallest distance to seam center that is perpendicular to the surface and located at the deepest point of the melt path. The vertical position of a pore was described as the smallest distance of it to the surface of the specimen. In terms of the cross-sectional size of pores, those were considered ideal circular, resulting in an approximated pore cross section area. The detected pores were categorized into different sizes classes. Fig. 2 gives a schematic description of the measurement procedure in term of the pores' position.

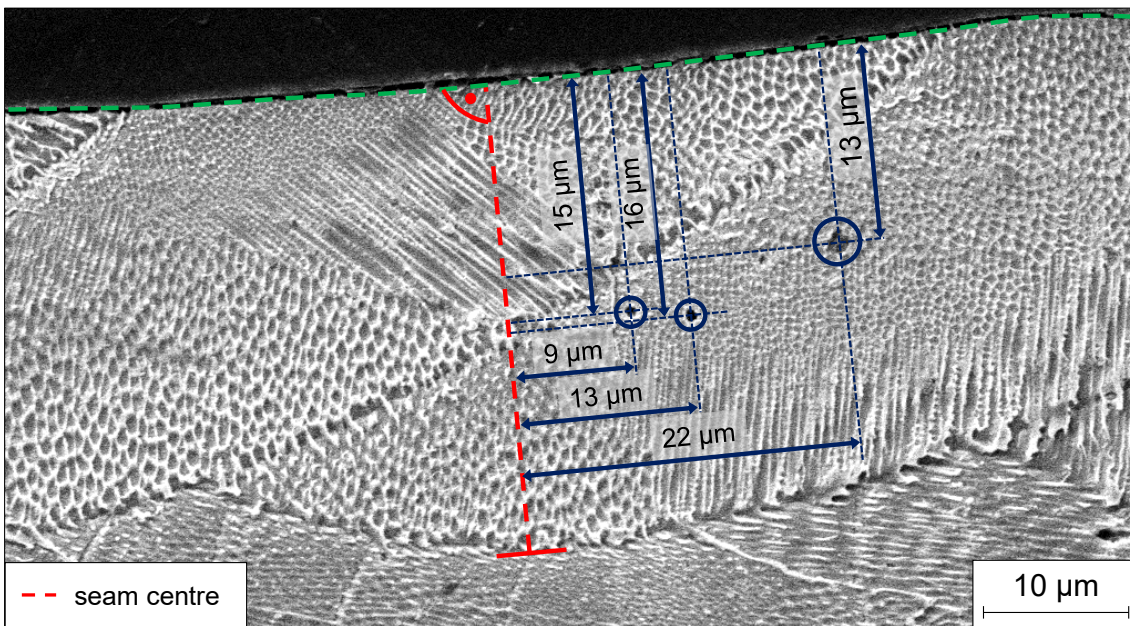
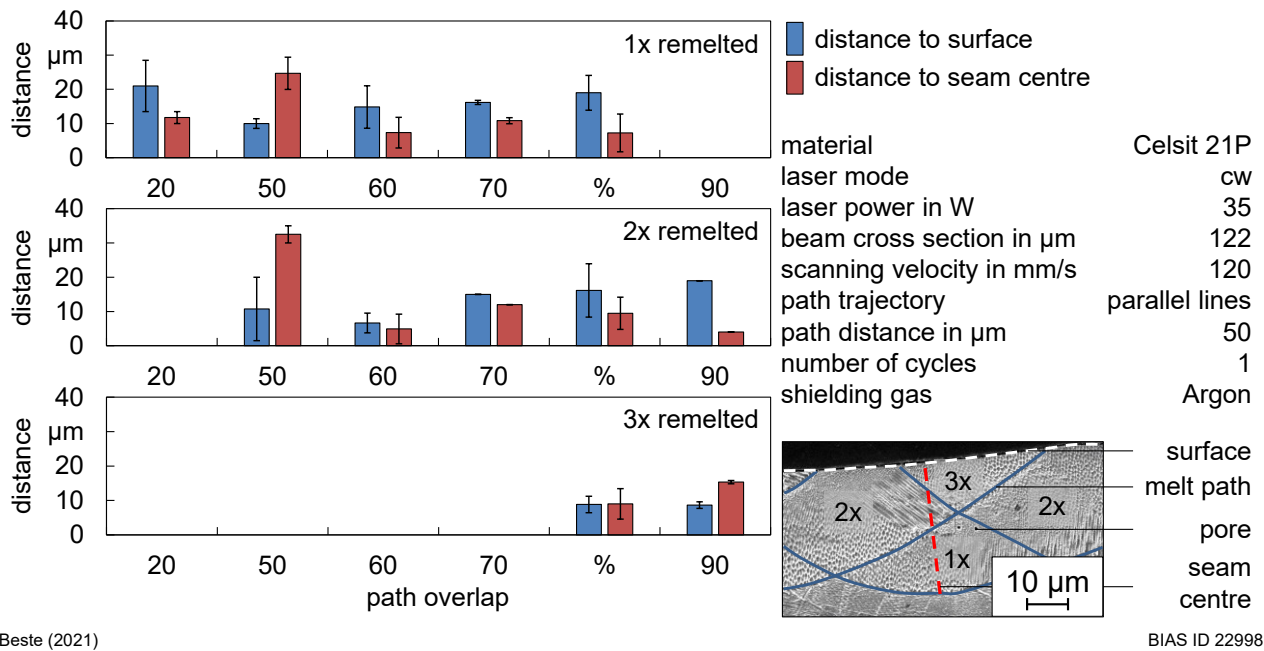


Fig. 2: Schematic depiction of pore position determination.

3 Results and Discussion

The evaluation of the distance of pores to the surface and the seam center as a function of different path overlaps leads to the results depicted in Fig. 3. As shown, depending on the path overlap, the areas are remelted between one to three times. Thereby, no clear tendency of the path overlap and hence the resulting number of remelting events on the distances of the pores to the surface and to the path center are noticeable. Therefore, the mechanism that gas moves to the surface on each case within the time when the molten pool is liquid and moves through the solidification fronts towards the center during solidification does not seem to play a significant role here.

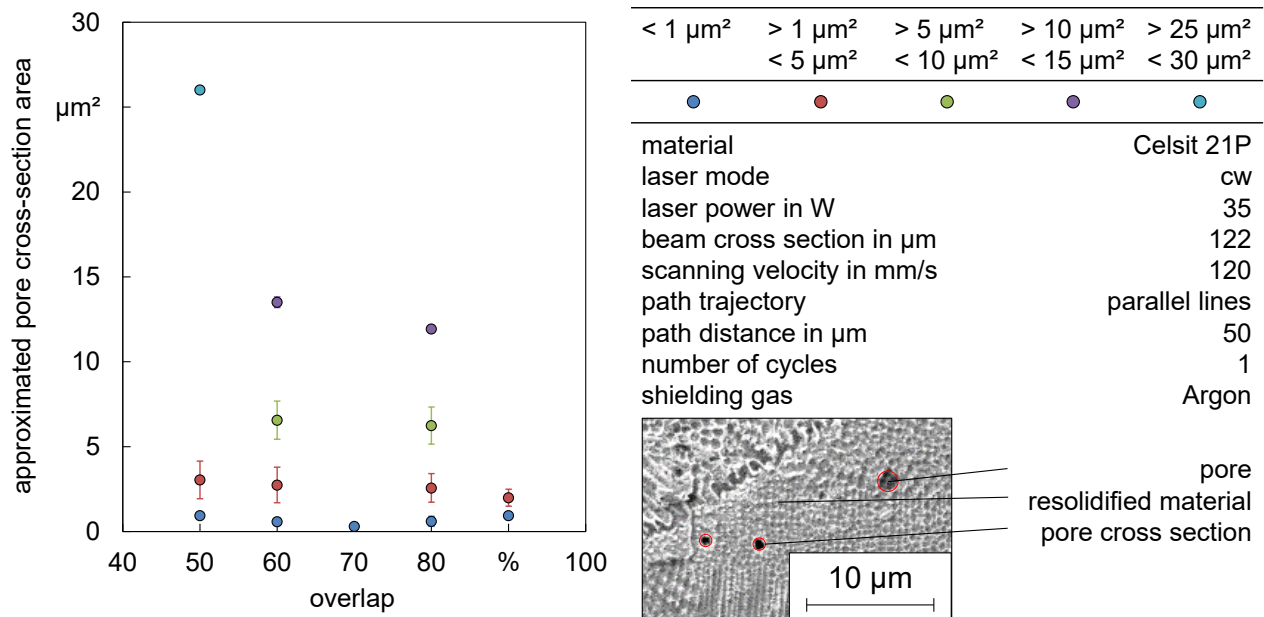


Beste (2021)

BIAS ID 22998

Fig. 3: Distances of pores to the surface and to the seam center in dependency of the path overlap.

In terms of the cross-sectional size of pores, Fig. 4 presents this size as a function of the path overlap. There seem to be only a slight size decrease with increasing overlap degree, but the variability on pore size decreases with increasing overlap distance. For the applied polishing and Argon shielding conditions, using a path overlap between 60 % and 90 %, only pores with an approximated pore cross section area smaller than 15 μm² were observed. Hence, laser polishing can lead to a nearly full dense sub-surface layer with remaining micropores only, which is not the expected condition directly after the PBF process, even if a direct correlation of the pore reduction in micrographs is not possible. Such small micropores are further difficult to measure with micro x-ray computed tomography to compare the PBF and polished state directly. Large pores with cross-section areas in the range of hundreds or thousands μm² as observed in laser polishing of PBF-LB/M with high mean laser power [6] were not detected. The results are in line with the findings in [7] and [3] showing that laser polishing can lead to a nearly full dense sub-surface layer. Further investigations are necessary to understand the acting mechanism which could be the elimination of pores due thermocapillary force as observed during PBF-LB/M [8].



Beste 2022

BIAS ID 22999

Fig. 4: Mean pore cross-sectional sizes in dependency of the path overlap.

4 Summary

In this work PBF-LB/M Co-Cr parts were laser polished with varying path overlaps resulting in regions being molten up to 3 times. For each case, cross sections of these molten paths were investigated in terms of occurring pores and their cross-sectional areas. No correlation between the number of remelting events and the pore distribution could be observed but the variability in pore size decreases with increasing overlap distance. Thus, the presumed mechanism that higher degrees of overlap, resulting in multiple melted areas, lead to a significantly increased reduction of the pores cannot be confirmed. A trend regarding a pore's size and its ability to be removed or reduced by the melt pool during laser polishing through remelting appears to be present and must be further investigated. The results show that laser polishing can lead to a nearly full dense sub-surface layer with only micropores remaining, whereby it is assumed that such a condition did not exist directly after the PBF process.

Acknowledgements

Funding by the Deutsche Forschungsgemeinschaft DFG (project 386371584 “Laser-Nachbearbeitung vielschichtiger Oberflächenstrukturen von additiv gefertigten Bauteilen“) and the U.S. National Science Foundation (grant no. 1727366 “Laser finishing of the multi-scale structure of additive manufactured parts“) is gratefully acknowledged.

References

- [1] A. Mostafaei, C. Zhao, Y. He, et al.: Defects and anomalies in powder bed fusion metal additive manufacturing. *Current Opinion in Solid State and Materials Science* 26/2 (2022) 100974.
- [2] H. Gong, R. Khalid, G. Hengfeng, et al.: Influence of defects on mechanical properties of Ti-6Al-4V components produced by selective laser melting and electron beam melting. *Materials & Design* 86 (2015) 545-554.
- [3] C. Liang, Y. Hu, N. Liu, et al.: Laser polishing of Ti6Al4V fabricated by selective laser melting. *Metals* 10 (2020) 191.
- [4] D. Panov, O. Oreshkin, B. Voloskov, et al.: Pore healing effect of laser polishing and its influence on fatigue properties of 316L stainless steel parts fabricated by laser powder bed fusion. *Optics&Laser Technology* 156 (2022) 108535.
- [5] E. Yasa, J.-P. Kruth, J. Deckers: Manufacturing by combining selective laser melting and selective laser erosion/laser re-melting. *CIRP Annals* 60 (2011) 263-266.
- [6] M. Hofele, A. Roth, J. Schanz, et al.: Laser polishing of additive manufactured aluminium parts by modulated laser power. *Micromachines* 12 (2021).
- [7] D. Bhaduri, P. Penchev, A. Batal, et al.: Laser polishing of 3D printed mesoscale components. *Applied Surface Science* 405 (2017) 29-46.
- [8] S.M.H. Hojjatzadeh, N.D. Parab, W. Yan, et al.: Pore elimination mechanisms during 3D printing of metals. *Nature Communications* 10 (2019) 3088.

Hybrid additive manufacturing with titanium powder and aluminum substrates via laser powder bed fusion

Sven Müller*¹ , Thorsten Mattulat¹ , Peer Woizeschke² 

¹ BIAS GmbH, Klagenfurter Straße 5, 28359 Bremen, Germany

² TU Dortmund University, Department of Mechanical Engineering, Professorship LMP+ (affiliated with ISF), Baroper Straße 303, 44227 Dortmund, Germany

Abstract

For the thermal joining of aluminum and titanium, the approach of solely melting the aluminum joining partner, while the titanium partner stays in the solid form, has been commonplace since 1996. This is done to limit the formation of a brittle intermetallic compound layer in the interface. In case of additive manufacturing with titanium powder and aluminum substrates, this approach is not transferrable because the titanium powder has to be melted to create the part. In this study, titanium samples were additively manufactured onto aluminum substrates using a commercial laser powder bed fusion (LPBF) machine. The influences of the energy density during the process on the sample porosity, the characteristics of the interface between sample and substrate, as well as the interfacial tensile strength are analyzed. Despite the melting of both materials, a great potential for high interfacial tensile strength has been found.

Keywords: Laser powder bed fusion, additive manufacturing, multi-material

1 Introduction

Due to the successive generation of parts layer by layer, the laser powder bed fusion manufacturing process (LPBF or PBF-LB/M for “powder bed fusion - laser beam / metals”) enables complex designs and the integration of additional functionalities [1]. Considering the improvement of structures in terms of high functionality and low weight, multi-material (hybrid) structures are of significant interest for adapting the part properties to specific local requirements [2]. Due to its layer-wise working principle, PBF-LB shows high potential for the generation of multi-material parts and in-situ alloying for graded material properties [3]. While state of research is constantly growing, hybrid and multi-material PBF-LB are currently still at beginning stages [4]. First implementation examples of multi-material PBF-LB production exist for the combination of different alloys based on the same material [5], of stainless steel and copper [6] as well as of aluminum and copper [7]. At the interface between those material pairings, intermetallic phases are formed. In case of aluminum and copper, significant cracking occurred within intermetallic compounds with thicknesses of 200 μm [7]. In addition to increasing interest in multi-material, also the additive manufacturing of hybrid metallic parts using ‘preforms’ is developed further [8]. Initial studies show that additional interlayers are needed to improve bonding when titanium powder is used for PBF-LB on stainless-steel substrates [9]. For the combination of aluminum powder and steel substrates, it was found that even though the steel substrate has a higher melting interval compared to the aluminum powder, its melting can only be avoided at comparatively small energy densities [10].

When joining aluminum and titanium, different intermetallic phases can be formed in the interface area. Aluminum-rich phases (i. e. trialuminide Al_3Ti) have a high oxidation resistance, but show very brittle material behavior after cooling down due to a low number of slip planes [11]. When joining aluminum and titanium thermally, the cooling process induces significant thermal stresses within the bi-metal component due to the

significantly different thermal expansion coefficients. These stresses are sufficient to cause failure by cracking without any additional forces [12].

The risk of an interfacial connection failure increases with increasing volume fractions of intermetallic phases in the interface area. If both joining partners (aluminum and titanium) melt during the process, the increased diffusion and mixing of the materials lead to excessive interfacial compound formation [13]. Therefore, the approach of solely melting the aluminum joining partner, while the titanium partner stays in the solid form, has been commonplace for the thermal joining of aluminum and titanium sheets or parts since 1996 [14]. If the thickness of the interfacial intermetallic compound layer is limited to approximately below 2 μm , tensile strengths of about 200 N/mm² have been achieved for different thermal joining processes [15].

2 Aim and Scope

Hybrid additive manufacturing using preform substrates offers new design possibilities and room for process chain optimization in terms of manufacturing costs and times. Therefore, the aim of this work is to verify the feasibility of a standard PBF-LB process to produce hybrid titanium-aluminum structures, see [17]. In the study reported here, the additive manufacturing with titanium powder and aluminum substrates is investigated using a commercial PBF-LB system and standard constant process parameters in the build direction of the samples. The hybrid titanium-aluminum samples are examined with regard to the porosity, the interface between sample and substrate, and, for selected parameter sets, the interfacial tensile strength as well as the fracture behavior.

The approach of solely melting the aluminum joining partner while the titanium component remains in a solid state should not be applicable for additively manufacturing with titanium powder and aluminum substrate via PBF-LB since the titanium powder must be melted during the process. The melting temperature of the titanium powder is significantly higher than that of the aluminum substrate. Therefore, it is hypothesized that the small melt pools and fast laser beam scanning speeds during PBF-LB, in comparison to typical laser-based thermal joining processes, reduce the interfacial intermetallic compound formation to an extent that adherent and strong interfaces can be generated despite melting of both materials in the interface, compare [17].

3 Materials and Methods

In this study, Ti6Al4V powder with a particle size distribution between 15 μm and 45 μm and EN AW 5083 substrates were used to additively manufacture hybrid samples using a commercial PBF-LB system (TruPrint 1000 from TRUMPF). This system operates with a maximum effective laser power of 200 W, a laser wavelength of 1070 nm, and a beam diameter in the working plane of 55 μm with a gaussian-like beam distribution. Argon (purity 4.8) was used to create an inert gas atmosphere with an oxygen level smaller than 0.01%. A bi-directional scanning strategy with a rotation of the scanning vectors between the individual layers of 51° was utilized. The energy density was adopted by varying the laser power and scanning speed. The layer thickness and hatching distance were kept constant at 20 μm and 80 μm respectively. The constant process parameters were selected according to common parameter ranges used for PBF-LB of Ti6Al4V [16]. The laser power and scanning speed were varied over a wide enough range to reach two times and less than half of commonly used energy densities. The variations were carried out to evaluate the influences on the process behavior, especially on the interface characteristics and properties. The first powder layer was manually created by moving the substrates, which were coated with a closed powder layer beforehand, upwards in 10 μm increments until the recoater used in the PBF-LB system had completely removed the powder from the substrate. Thereafter, the substrate was moved down by 20 μm and new powder was applied using the recoater.

The influence of different energy densities (different laser powers and scanning speeds) on the porosity was determined using additively manufactured 5 mm cube samples. These were analyzed using vertical cross sections in the center of the sample and a contrast-based image analysis. For this, a light microscope (ZEISS Axio) and the ‘Olympus Stream’ analysis software were utilized. The connection areas to the substrates and the direct surface areas of the samples were not taken into consideration within the porosity analysis. The microscope images of the cross sections were also used to determine the ‘connection in cross section’ (see Fig. 1). Therefore, a pixel-based length analysis was used to measure the percentage of the actual connection length (between the additively manufactured sample and the substrate remaining after the process) from the width of the cube. The measurements were carried out using a scanning electron microscope (SEM) (EVO-MA10 from ZEISS). For the material contrast in the images, a backscattered electron (BSE) detector was utilized. In addition, an energy dispersive X-ray spectroscopy (EDS) (Bruker Quantax) was used to determine elemental compositions. Tensile specimens were produced to analyze the interfacial tensile strength (see Fig. 1) between the additively

manufactured structures and the substrates. To avoid influences of post-processing steps, the tensile specimens were directly manufactured in a wedge-shape and tested in as-built condition. The tensile testing was performed using a ZwickRoell Z250 RED tensile testing machine and a Xforce HP load cell with a measuring range between 10 N and 5000 N. For each set of examined parameters, five tensile test samples were produced and tested. Therefore, to account for deviations in the samples, the median and the mean positive and negative deviations were calculated. The tensile strengths of all specimens were calculated using the initial connection area (not the actual remaining area after cooling), which was measured using a Keyence VK-9710 laser-scanning confocal microscope and the ‘VK Viewer VKH1V1E’ software (see Fig. 1). The same confocal microscope and software were used to measure the height profiles of the substrate-sided fracture surfaces of the tensile test samples and to determine the average height differences between the substrates and fracture surfaces.

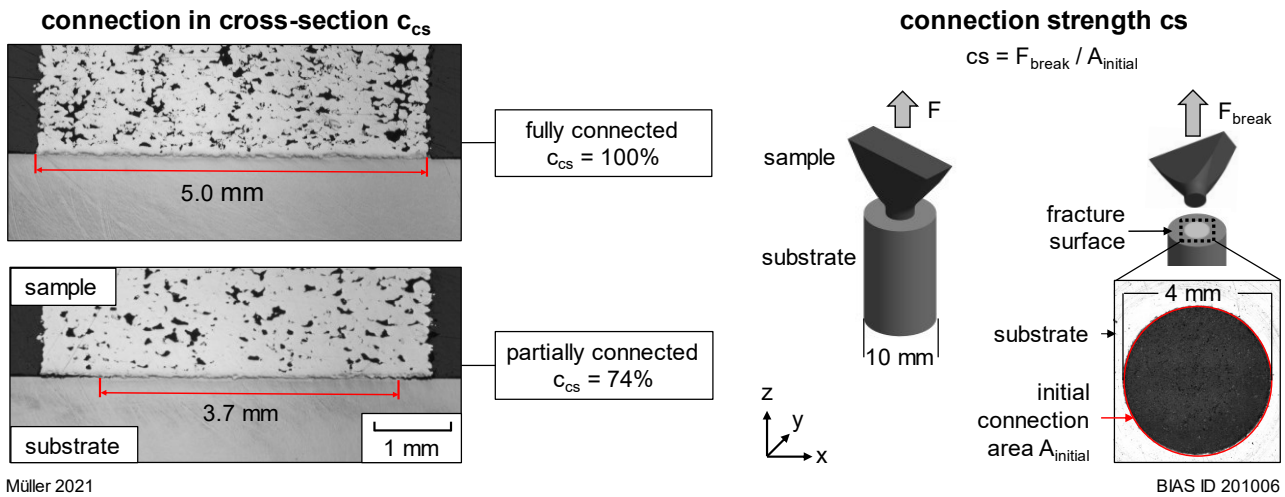
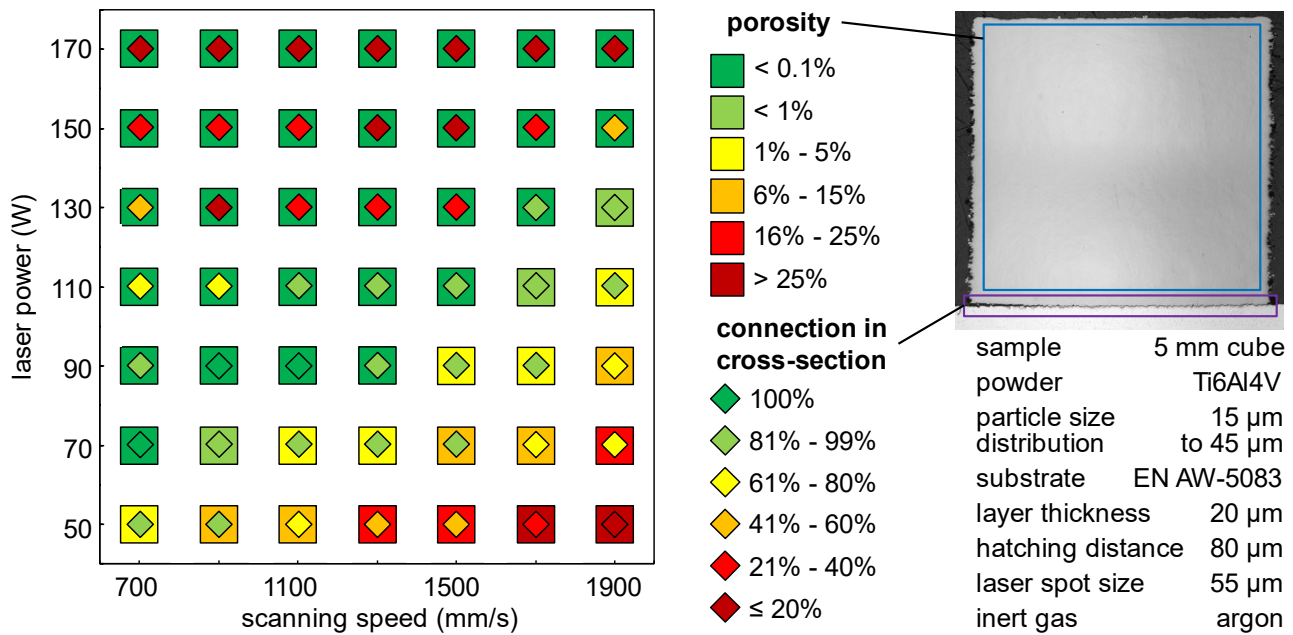


Fig. 1: Determination of the connection in cross-section and the connection strength, according to [17]

The optical properties of the first 20 μm powder layers were examined using a double integrating sphere setup with a laser wavelength of 1080 nm and a diffusely reflecting BaSO₄ sphere coating. Thereby, the reflection of the laser radiation at the powder layer and the transmission of the laser radiation through the powder layer were measured. More details regarding the double integrating sphere setup can be found in [17].

4 Results

Using the double integrating sphere setup, the transmission of a measuring laser beam with the same wavelength regarding the LPBF processing laser beam through Ti6Al4V powder layers with a thickness of 20 μm was measured as 22%. With a determined reflection of 14%, the absorption of the laser radiation by the titanium powder was calculated as 64%. The influence of the energy density on the porosity and the interfacial connection measured in the cross sections of the Ti6Al4V samples additively manufactured onto EN AW 5083 substrates is shown in Fig. 2 for energy densities between 16 J/mm³ and 152 J/mm³. Three parameter sets resulted simultaneously in a porosity < 0.1% and a complete interfacial connection after cooling.

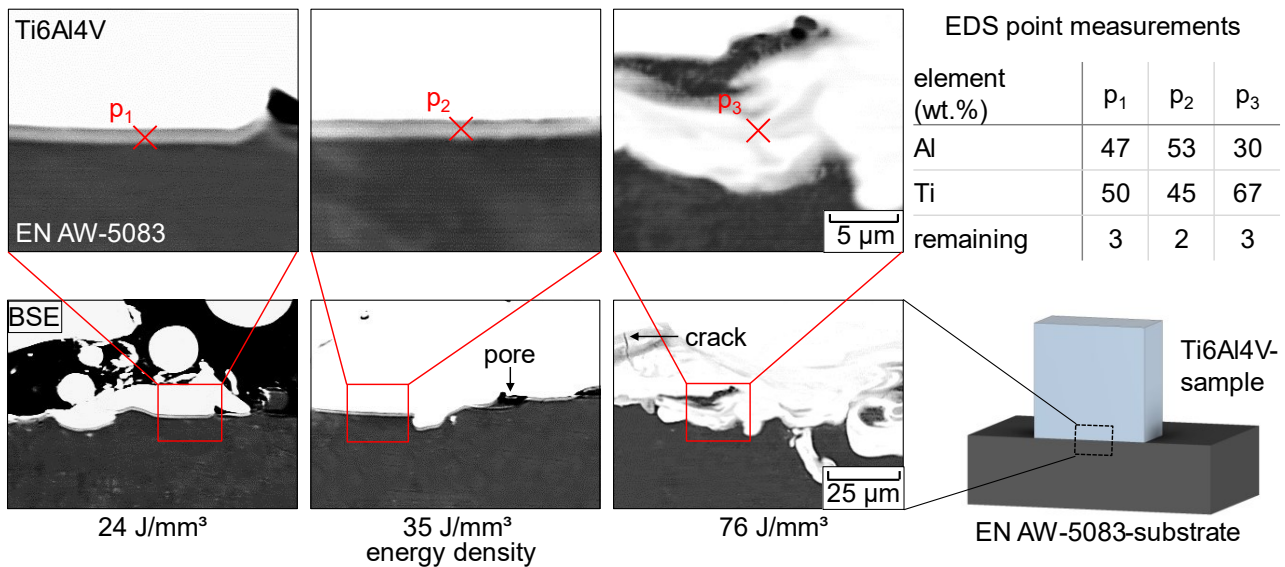


Müller 2021

BIAS ID 201062

Fig. 2: Influence of laser power and scanning speed on the porosity and the connection in cross-sections of titanium-aluminum hybrid samples, data from [17]

In Fig. 3, exemplary BSE images of the interfacial areas are shown for increasing energy densities from left to right. At a low energy density (24 J/mm^3 : 50 W and 1300 mm/s), the formation of intermetallic compounds is limited to a layer of $1 \mu\text{m}$ thickness. However, significant lack of fusion porosity on the titanium side (white in the image) is observable. When slightly increasing the energy density (35 J/mm^3 : 50 W and 900 mm/s), the porosity in the titanium is reduced and the intermetallic compound layer is approx. $1.5 \mu\text{m}$ thick. For higher energy densities, the substrate strongly melted and a dominant mixing of titanium and aluminum occurred. Irregularly distributed intermetallic compounds and cracks are present in a $40 \mu\text{m}$ wide area around the interface.



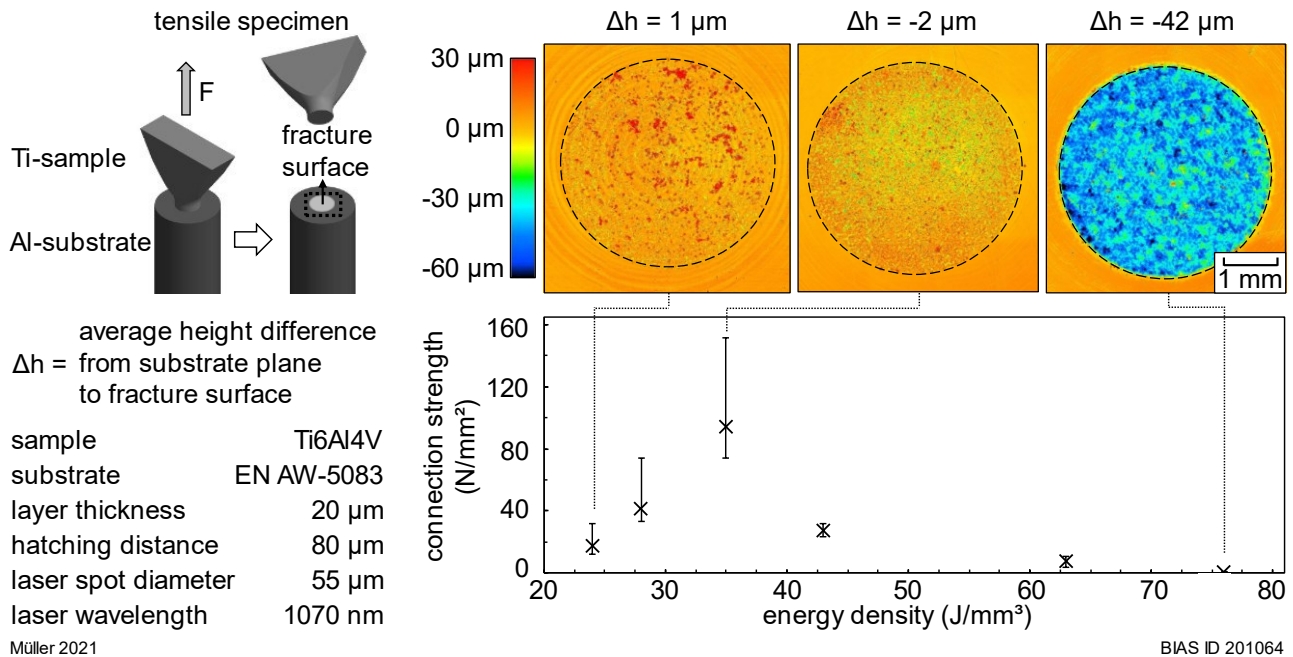
Müller 2021

BIAS ID 201063

Fig. 3: BSE images of the connection areas of titanium-aluminum hybrid samples as well as EDS point measurements. [17]

Fig. 4 shows the tensile strength of titanium-aluminum tensile specimen produced with different energy densities in the range of 24 J/mm^3 (50 W and 1300 mm/s) to 76 J/mm^3 (110 W and 900 mm/s) as well as exemplary correlating height profiles of substrate-sided fracture surfaces. In the case of an energy density of 35 J/mm^3 (50 W and 900 mm/s), the highest strengths occurred with a median value of 94 N/mm^2 and a mean positive deviation up to 151 N/mm^2 (maximum individual sample value 170 N/mm^2). Thereby, the average height difference between the substrate surface (=initial interface) and the fracture surface lies at a small negative value, i.e. mainly some microns in the direction of the aluminum (Fig. 4 height measurement in the middle). At a

smaller energy density of 24 J/mm^3 (Fig. 4 left height measurement), the significantly lower strength correlates with a change of the fracture surface average height level in the direction of the titanium side (positive red peaks in Fig. 4 left). Otherwise, an increase in the energy density to 76 J/mm^3 results in a connection strength of below 5 N/mm^2 . The corresponding fracture surface (Fig. 4 right height measurement) lies at an average height of $42 \mu\text{m}$, i.e. significantly within the height level of the initial aluminum substrate.



Müller 2021

BIAS ID 201064

Fig. 4: Connection strengths and height profiles of the substrate-sided fracture surfaces of titanium-aluminum tensile specimen. [17]

5 Discussion

The hypothesis, namely that the small melt pools and fast laser beam scanning speeds during PBF-LB, in comparison to the typical laser-based thermal joining processes, reduce the interfacial intermetallic compound formation in the case of titanium powder onto aluminum substrate to an extent that adherent and strong interfaces can be generated despite melting of both materials in the interface, is supported by this study (see also [17]). The experiments have demonstrated that parameters exist that result in low porosity within the additively manufactured titanium volume as well as simultaneously in a completely connected interface to the aluminum substrate. Firstly, the transmission of laser radiation through a $20 \mu\text{m}$ thick titanium powder layer is low (22%). Additionally, the Fresnel absorption of laser radiation of the wavelength used is much less in the case of aluminum than for titanium. Secondly, the high thermal conductivity of aluminum increases the thermal conduction into the substrate volume and the corresponding heat loss. This results in high temperature gradients near the interface and rapid cooling. This can explain the comparatively marginal melting of the aluminum, despite the contact with molten titanium having a much higher melting temperature, and the formation of thin intermetallic compound layers with thicknesses $< 2 \mu\text{m}$ (see Fig. 3). Comparable to the findings for conventional joining of aluminum and titanium as well as for multi material PBF-LB of aluminum and copper [7], it could be shown that thin intermetallic layers are not prone to cracking and show high bonding strengths, while bigger intermetallic layers are susceptible to cracking and only have minor bonding strengths. A distinct assignment of the present intermetallic phases to known aluminum titanium phases (TiAl , Al_3Ti , Ti_3Al) was not possible. The aforementioned reasons can explain the fact that strength values of up to 170 N/mm^2 were achieved for individual tensile test samples. The rough surfaces (as-built condition) and the notch stress effect due to the specimen shape might be two reasons for the remaining gap to the values of $> 200 \text{ N/mm}^2$ [15] being reported for conventional aluminum-titanium joints.

6 Conclusion

For the hybrid additive manufacturing of titanium samples onto aluminum substrates using a commercial PBF-LB machine with a constant layer thickness ($20 \mu\text{m}$) and constant energy densities in build direction, it can be concluded that, rather contradictory to the state of the art in laser-based joining of aluminum and titanium:

The manufacturing of titanium powder onto aluminum substrates shows high strength potential as dense titanium volume can already be built up, while only small amounts of intermetallic compounds are formed at the interface.

References

- [1] M. Schmidt, M. Merklein, D. Bourell, D. Dimitrov, T. Hausotte, K. Wegener, G.N. Levy: Laser based additive manufacturing in industry and academia. *CIRP Annals* 66(2) (2017) 561–583.
- [2] K. Martinsen, S.J. Hu, B.E. Carlson: Joining of dissimilar materials. *CIRP Annals* 64(2) (2015) 679–99.
- [3] M. Schmidt, M. Merklein, D. Bourell, D. Dimitrov, T. Hausotte, K. Wegener, L. Overmeyer, F. Vollertsen, G.N. Levy: Laser based additive manufacturing in industry and academia. *CIRP Annals* 66(2) (2017) 561–83.
- [4] M. Schneck, M. Horn, M. Schnitt, C. Seidel, G. Schlick, G. Reinhart: Review on additive hybrid- and multi-material-manufacturing of metals by powder bed fusion: state of technology and development potential. *Progress in Additive Manufacturing* (2021).
- [5] C. Wei, L. Li: Recent progress and scientific challenges in multimaterial additive manufacturing via laser-based powder bed fusion. *Virtual and Physical Prototyping* (2021) 1-25.
- [6] C. Wei, L. Li, X. Zhang, Y.H. Chueh: 3D printing of multiple metallic materials via modified selective laser melting. *CIRP Annals* 67(1) (2018) 245–8.
- [7] S.L. Sing, L.P. Lam, D.Q. Zhang, Z.H. Liu, C.K. Chua: Interfacial characterization of SLM parts in multi-material processing: Intermetallic phase formation between AlSi10Mg and C18400copper alloy. *Materials Characterization* 107 (2015) 220-227.
- [8] P. Pencheva, D. Bhadurib, L. Carterc, A. Mehmetia, K. Essaa, S. Dimova, N.J.E. Adkinse, N. Maillold, J. Bajoletd, J. Maurathe, U. Jurdeczkaf: System-level integration tools for laser-based powder bed fusion enabled process chains. *Journal of Manufacturing Systems* 50 (2019) 87-102.
- [9] C.F. Tey, X. Tan, S.W. Sing, W.Y. Yeong: Additive manufacturing of multiple materials by selective laser melting: Ti-alloy to stainless steel via a Cu-alloy interlayer. *Additive Manufacturing* 31 (2020) 100970.
- [10] D.S. Nguyen, H.S. Park, C.M. Lee: Applying Selective Laser Melting to Join Al and Fe: An Investigation of Dissimilar Materials. *Applied Sciences*. 9(15) (2019) 3031.
- [11] M. Yamaguchi, Y. Umakoshi, T. Yamane: Plastic deformation of the intermetallic compound Al₃Ti. *Philosophical Magazine A* 55(3) (1987) 301–15.
- [12] B. Majumdar, R. Galun, A. Weisheit, B.L. Mordike: Formation of a crack-free joint between Ti alloy and Al alloy by using a high-power CO₂ laser. *JOURNAL OF MATERIALS SCIENCE* 32 (1997) 6191–200.
- [13] I. Tomashchuk, P. Sallamand, E. Cicala, P. Peyre, D. Grevey: Direct keyhole laser welding of aluminum alloy AA5754 to titanium alloy Ti6Al4V. *Journal of Materials Processing Technology* 217(0) (2015) 96–104.
- [14] P. Skoda, J. Dujak, P. Michalicka: Creation of heterogeneous weld joints of titanium- and aluminium-based materials by electron beam welding. Japan - Slovak welding symposium proceedings of the International Welding Conference (1996) 157–160.
- [15] M. Kreimeyer, F. Wagner, F. Vollertsen: Laser processing of aluminum-titanium-tailored blanks. *Optics and Lasers in Engineering* 43(9) (2005) 1021–35.
- [16] S. Pal, G. Lojen, V. Kokol, I. Drstvensek: Evolution of metallurgical properties of Ti-6Al-4V alloy fabricated in different energy densities in the Selective Laser Melting technique. *Journal of Manufacturing Processes* 35 (2018) 538–46
- [17] S. Müller, P. Woizeschke: Feasibility of a laser powder bed fusion process for additive manufacturing of hybrid structures using aluminum-titanium powder-substrate pairings. *Additive Manufacturing* 48 (2021) 1–7.

Prevention of coating-induced agglomerations within the weld seam during laser beam deep penetration welding of aluminum-silicon coated press-hardened steel

Marcel Möbus¹ , Peer Woizeschke² , Thorsten Mattulat¹ 

¹BIAS - Bremer Institut für angewandte Strahltechnik GmbH, Klagenfurter Str. 5, 28359 Bremen, Germany

²TU Dortmund University, Department of Mechanical Engineering, Professorship LMP+ (affiliated with ISF), Baroper Straße 303, 44227 Dortmund, Germany

Abstract

Press-hardened steels like 22MnB5 (1.5528) have great potential in terms of their use in the field of lightweight construction. However, due to the aluminum-silicon coating, applied for press-hardening, strength-reducing agglomerations can occur within the seam after laser deep penetration welding of already hardened material. To investigate the hypothesis that the agglomeration formation can be reduced by beam modulation strategies, laser deep penetration welding experiments with changing beam modulation strategies such as “transversal”, “circular” and “vertical eight” shaped patterns were carried out using constant welding speed and laser power. After comparing the resulting cross-sections to coated and decoated samples welded without beam modulation, the hypothesis was found to be true in case of all modulation strategies examined as no agglomerations could be detected within the samples. In addition, in case of the beam modulation strategies “circle” and “vertical eight”, the fracture type could be changed from a separation fracture along the melting line to a shear fracture crosswise to the seam in sheet metal plane comparable to the decoated samples.

Keywords: Laser beam welding, beam modulation, agglomeration prevention, aluminum-silicon coating

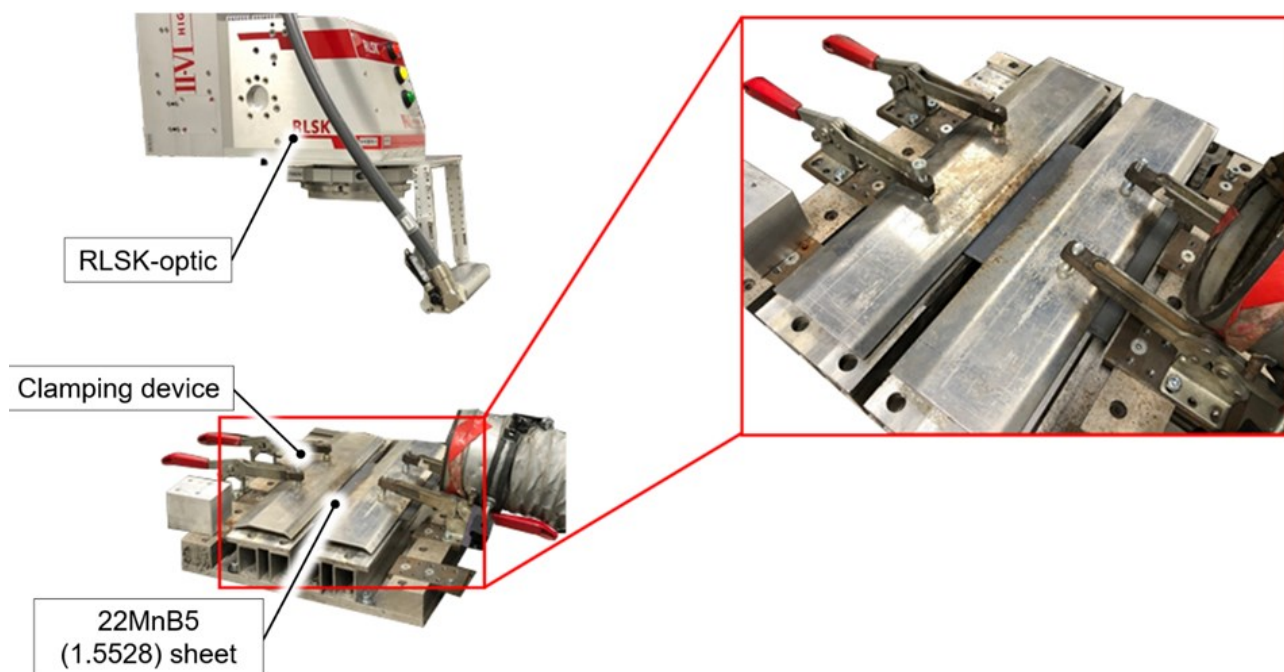
1 Introduction

Steel-intensive lightweight construction makes it possible to reduce the weight of e.g. automobiles by using thin-walled steel components with maximum strength, including press-hardenable manganese boron steels. One of the most widely used manganese boron steel grades is 22MnB5 (1.5528), which has very good formability when untempered (ferritic) and an extremely high tensile strength of about 1650 MPa when tempered (martensitic) [1]. To prevent tinder formation during press hardening, MnB steels are coated [2]. The most widespread coating systems of press-hardening materials currently on the market are aluminum-silicon based (AS) coatings, which allow direct press hardening [1]. When welding coated and already hardened MnB steels, the coating primarily dissolves into weldments as solid solution with an aluminum content of about 2.6 atom-% and partially develops as an inter-metallic phase with Fe and an aluminum content of about 6.7 atom-% [3]. The resulting presence of intermetallic phases in the weld metal leads on the one hand to a reduction in joint strength [4], and on the other hand alloying leads to an increase in the critical cooling rate required for martensite formation. A considerable reduction of the achievable joint strength occurs especially in laser beam deep penetration welding, since the intermetallic brittle phases accumulate at the melting line as a result of the melt pool flow [3]. However, this also makes it possible to influence the melt pool flow and thus the agglomeration formation by means of suitable process manipulation like multiple remelting, as pursued in the case of multi-dimensional local beam oscillation or modulation strategies. In addition, spatial beam modulation can increase the seam or bond width. This is why beam modulation strategies have been investigated based on the hypothesis that temporal and/or spatial beam modulation strategies can prevent the formation of

agglomerations and homogeneously distribute the intermetallic phases in the melt pool, increasing the overall joint strength.

2 Experimental

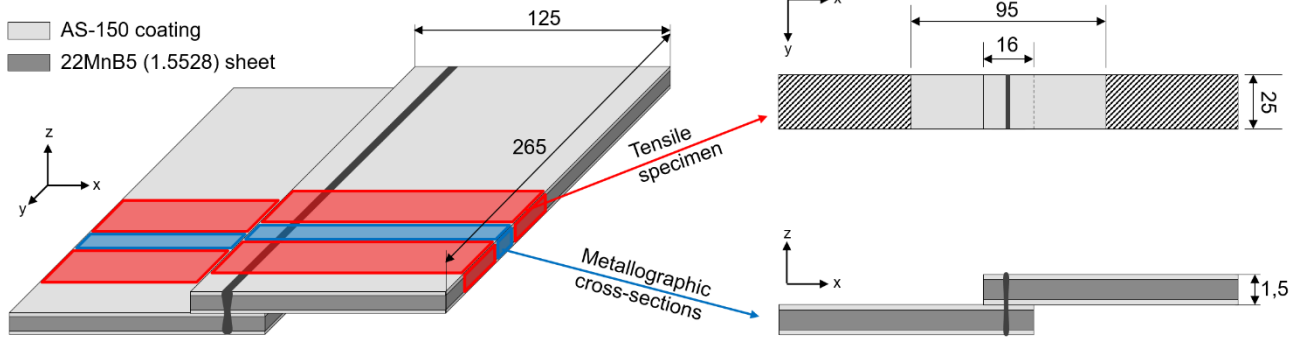
The experimental setup is shown in Fig. 1. A processing optic RLSK 2.1 by HIGHYAG Lasertechnologie (nowadays part of the II-VI Group). was used with a disk laser source TruDisk 12002 by TRUMPF. The spot diameter and the Rayleigh length were measured to 570 μm and 9.6 mm. “AS-150”-coated and partially de-coated (using a TruMicro 5050 ultrashort pulse laser by TRUMPF) 1.5 mm thick 22MnB5 (1.5528) sheets were clamped as displayed in Fig. 2 while laser deep penetration welding in lap joint configuration. In this study, three beam modulation strategies (Tab. 1) are compared with the laser deep penetration welding process without beam modulation with respect to the agglomeration formation and the lap shear strength. All experiments were carried out with the constant laser beam power of 2.5 kW and the welding speed of 0.96 m/min. The experiments with beam modulation were done with a focal position of 0 mm, an oscillation frequency of 60 Hz and an oscillation amplitude of 400 μm . The linear welded samples were welded with a focal position at -16 mm in order to reach a comparable seam width of 930 μm on the sample surface. One welded sample per parameter was cut into ten tensile test samples and 15 metallographic samples for cross-section analyses by using a wire-cut electrical discharge machine. The resulting lap shear tests were carried out using a materials testing machine of the type AllroundLine Z250 by ZwickRoell to determine the maximum endured tensile force and the fracture type (see Fig. 3). Metallographic cross-sections were etched and microscope images were taken to measure the seam width and analyze the agglomeration formation. Regardless of the type of fracture, the lap shear strength σ was calculated from the seam width at the sheet metal transition a , the test sample width l and the maximum tensile force F using the equation $\sigma = \frac{F}{a \cdot l}$.



Möbus 2022

Fig. 1: Experimental setup

BIAS ID 220369



Möbus 2022

BIAS ID 220368

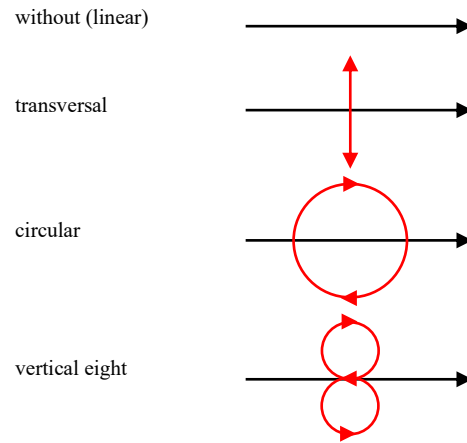
Fig. 2: Dimensions of the weld, lap shear test and analysis specimens

Tab. 1: Laser beam welding parameters and beam modulation strategies (global welding direction displayed in black, oscillation pattern displayed in red)

Laser beam welding parameters

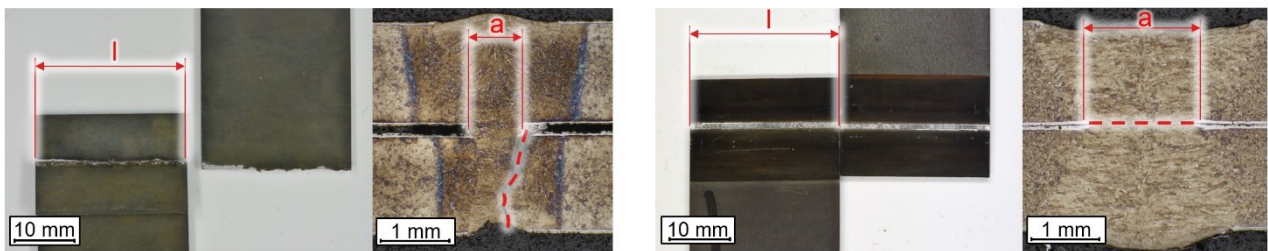
Laser power	2.5 kW
Focal diameter	570 μm
Rayleigh length	9.6 mm
Focal position linear weld	-16 mm
Focal position with oscillation	0 mm
Welding speed	0.96 m/min
Oscillation frequency	60 Hz
Oscillation amplitude	400 μm
Joint type	Lap joint

Beam modulation strategies



Separation fracture

Shear fracture



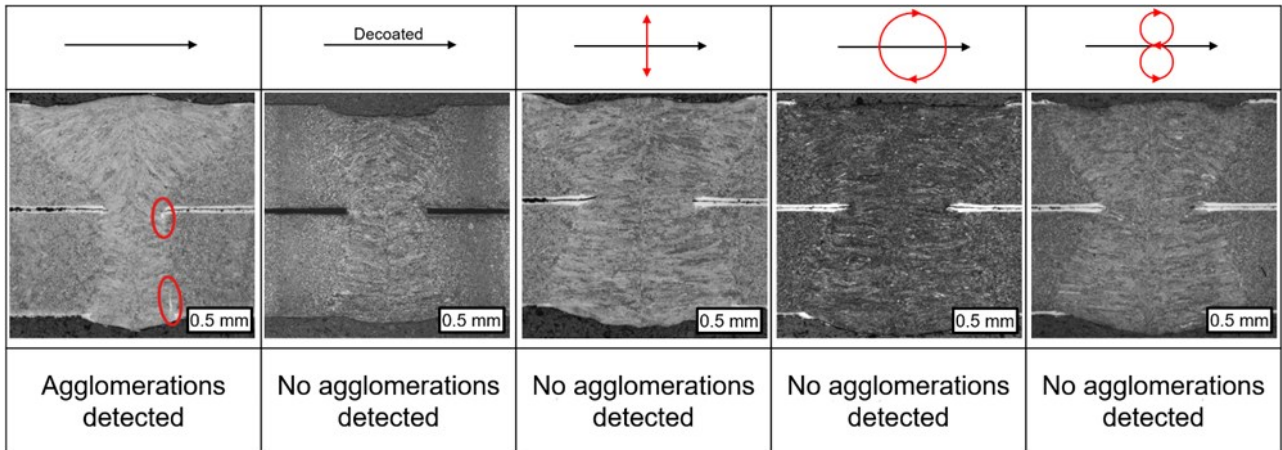
Möbus 2022

BIAS ID 220371

Fig. 3: Shear testing fracture types, sample width (l) and seam width at the sheet metal transition (a)

3 Results

The results of the analysis of the metallographic cross-sections are shown in Fig. 4. The welding without beam modulation resulted in the formation of agglomerations along the melting line, as it was also shown in [3]. In case of all beam modulation strategies, all 15 metallographic cross-sections per strategy are free of agglomerations bigger than 50 μm in diameter.



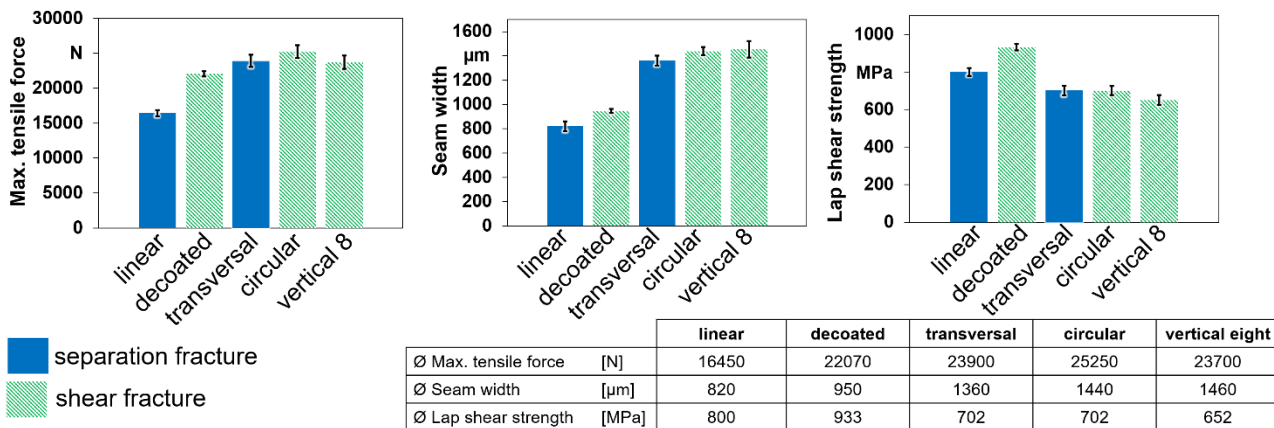
Möbus 2022

BIAS ID 220354

Fig. 4: Exemplary metallographic cross-sections

Fig. 5 shows the results of the tensile lap shear tests. The average maximum endured tensile force increases significantly for all modulation strategies and for decoated linear welded samples compared to the coated specimens welded linear without beam modulation. Furthermore, by applying the beam modulation strategies “circle” and “vertical eight”, the fracture type varied between the separation fracture along the melting line and the shear fracture crosswise to the seam in sheet metal plane, comparable to the decoated samples. The seam width also increases for all modulation strategies compared to the coated and decoated specimens welded linear without beam modulation, while the lap shear strength is significantly lower for the samples welded with beam modulation strategy.

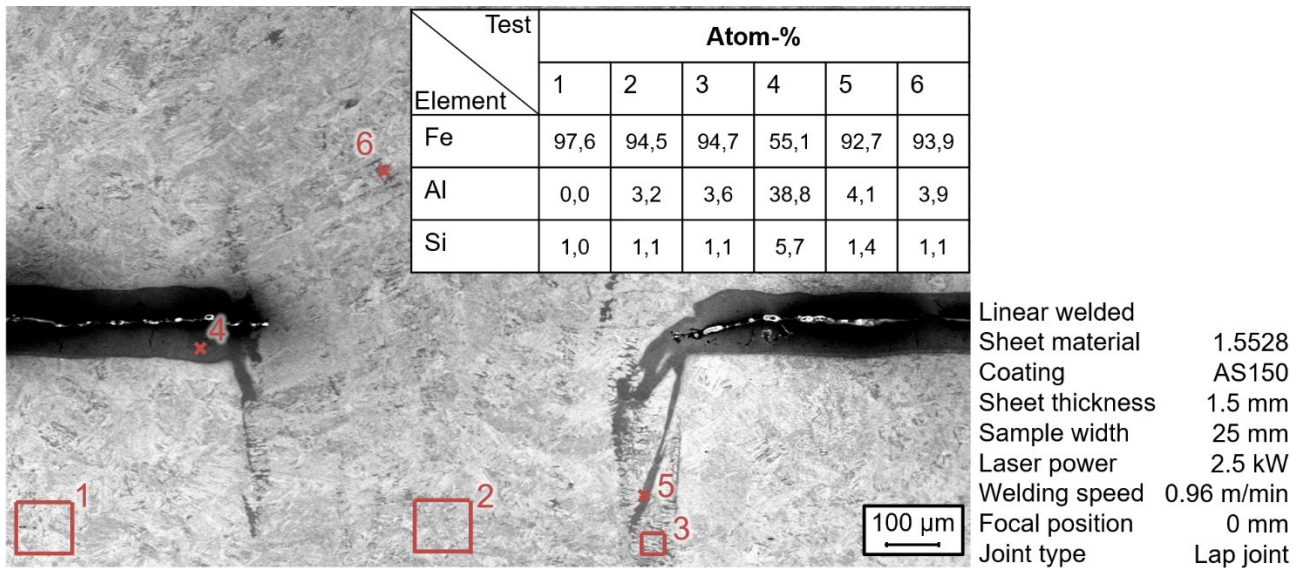
The Energy-dispersive X-ray spectroscopy (also known as EDS, EDX, or EDXA) measurement in Fig. 6 shows that the aluminum content of the homogeneously distributed intermetallic phases (Test 6, 3.9 atom-% Al) is comparable to the content in the agglomerations along the melting line (Test 5, 4.1 atom-% Al) and that the entire structure of the weld seam generally has a high aluminum content (Test 2, 3.2 atom-% Al).



Möbus 2022

BIAS ID 220355

Fig. 5: Results of the lap shear tests



Mobus 2022

BIAS ID 220370

Fig. 6: EDX- (Energy-dispersive X-ray spectroscopy) measurement results of the welded 22MnB5 sample with AS-150 coating and without beam modulation.

4 Discussion

Since no agglomerations are visible in the cross sections of all specimens welded with beam modulation, the hypothesis that beam modulation strategies can prevent their formation can be evaluated as true with high probability. However, in the case of beam modulation, the increase in maximum tensile force is not only due to the prevention of agglomeration formation, but primary to the increased seam widths. The results of the increased seam widths also explain the lower lap shear strength across all beam modulated specimens compared to the linear welded samples. The EDX-analysis showed with 3.2 atom-% (test 2) a higher content of aluminum within the weld than it was found in [4], where the aluminum content was measured to 2.55 atom-%. The strength of the samples welded with beam modulation is reduced compared to the decoated samples without beam modulation, which suggests that not only the agglomerations but also the homogeneously distributed aluminum phases and the structural transformation as a result of the welding process in general reduce the strength of the welded samples.

5 Conclusions

Based on the experiments of this study, it can be concluded that the investigated beam modulation strategies prevent the formation of the typical agglomerations along the melting line and can be used to increase the seam width and therefore also the maximum tensile force that can be applied. The application of the beam modulation strategies distributes the coating entry homogeneously in the weld seam and, thus, the fracture type changes partly from separation fracture to shear fracture. However, the uniform aluminum content due to the coating-based aluminum input within the entire seam in combination with an increase in seam width at the sheet transition also result in a reduction of the lap shear strength.

Acknowledgements

The IGF project No. 20652 N (P 1215) of the FOSTA – Research Association for Steel application was supported by the program for Industrial Collective Research (IGF), funded by the Federal Ministry for Economic Affairs and Climate Action based on a decision by the German Bundestag. This support is greatly acknowledged. The “BIAS ID” numbers are part of the figures and allow the retraceability of the results with respect to the mandatory documentation required by the funding organization.

References

- [1] ArcelorMittal: Warmumformstähle -Usibor® - Extrem hochfeste Stähle. Produktinformation Januar 2014.
- [2] Karbasian, H.; Tekkaya A. E.: A review on hot stamping. In: Journal of Materials Processing Technology 210 (2010), Elsevier, pp. 2103–2118.
- [3] Kim, C.; Kang, M. J.; Park, Y. D.: Laser welding of Al-Si coated hot stamping steel. In: International Conference on the Mechanical Behavior of Materials (ICM11), Procedia Engineering 10 (2011), 2226–2231.
- [4] Vierstraete, R.; Cretteur, Pic, A.; Yin, Q.: Laser ablation for hardening laser welded steel blanks. In: Industrial Laser Solutions for Manufacturing 25 [2] (2010)

Industrial applicability of reflection-assisted laser beam brazing of ZM-coated steel sheets

Insa Henze*¹ , Ronald Pordzik¹ , Philip Marben², Thorsten Mattulat¹ 

¹ BIAS - Bremer Institut für angewandte Strahltechnik GmbH, Klagenfurter Straße 5, 28359 Bremen, Germany

² Scansonic MI GmbH, Schwarze-Pumpe-Weg 16, 12681 Berlin, Germany

Abstract

A major challenge in laser beam brazing of zinc-magnesium-coated (ZM) steel sheets is the uniform preheating of the substrate surface for achieving a stable wetting process. A process modification of the conventional laser beam brazing that addresses this requirement is the reflection-assisted laser beam brazing in laser leading configuration, which utilizes the laser reflections from the brazing wire onto the substrate material for preheating and wire melting with a single laser beam. In this study the industrial applicability of this process variant is addressed by analyzing the process parameters as well as the required position tolerance limits for continuous and uniform seams.

The results showed the suitability of a laser beam brazing process in laser leading configuration for ZM-coated steel sheets. Process velocities of 6 m/min were possible. Regarding the process tolerances it has been shown that flange joints with a gap width of up to 100 µm and lateral displacements of the TCP of up to 400 µm were joinable. The brazing seams showed a higher tensile shear strength than the substrate material.

Keywords: Laser brazing, Zinc-magnesium-coated steel, Reflection-assisted laser brazing

1 Introduction

Zinc-magnesium (ZM)-coated steel sheets, e.g. used in car body construction for automotive production, offer higher corrosion resistance than conventionally hot-dip galvanized steel sheets [1]. To connect this coated body parts, especially in areas that lie in the field of view of the customer, laser beam brazing in flanged joint configuration with copper based brazing material is widely applied [2]. ZM-coated steel sheets have higher demands on the joining process regarding a complete wetting inside of the flange joint area towards the conventionally used brazing materials, as shown by Wachsmuth et al. [3].

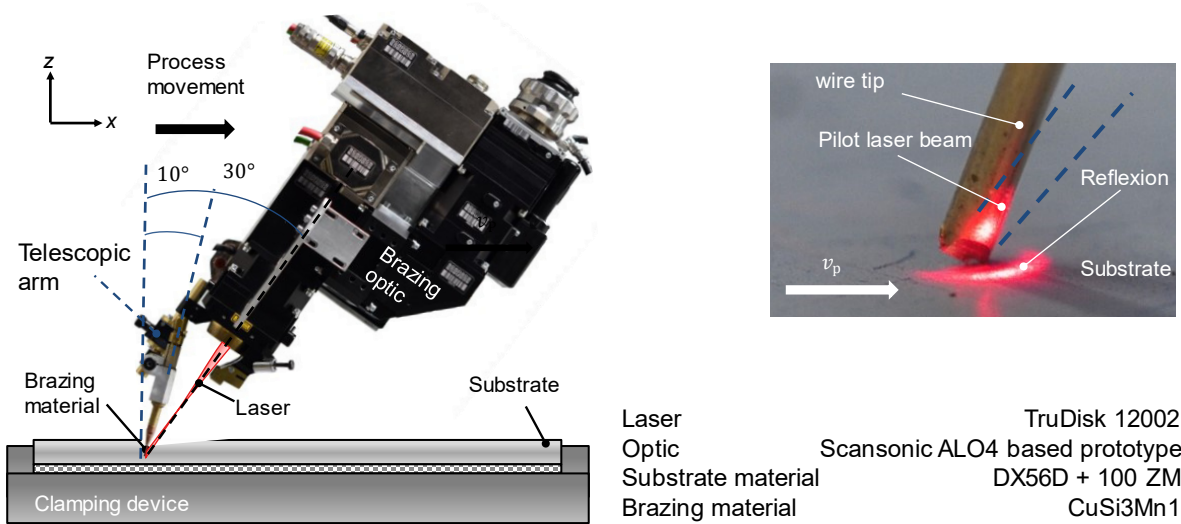
An approach to improve the wetting process is the preheating of the substrate surface [4]. In the conventionally used laser brazing processes with one laser beam in wire leading configuration the preheating is realized using a laser beam diameter bigger than the wire diameter. Nonetheless, the brazing wire is shadowing the substrate surface in front of the wire and the process zone respectively, limiting the area of direct preheating [5]. A possibility to improve the preheating is a laser brazing process in laser leading configuration as shown by Mittelstädt et. al. [5]. The brazing material and the laser beam axis are positioned with an inclination in process movement direction towards the surface normal of the substrate surface whereby the angle of the beam axis was bigger than that of the brazing material (cf. Fig. 1). The laser beam is thus positioned in leading direction, melting the brazing material from the bottom side. Due to the positioning of the wire and laser beam axis the reflected laser beam from the brazing material is partially reflected onto the substrate surface in front of the brazing material [6]. The joining zone in front of the brazing material is therefore directly preheated by the laser reflection. This enhances the preheating in comparison to the conventional process in wire leading configuration where the area in front of the wire is shadowed by the brazing wire.

With regard to industrial applicability, robot-based laser brazing requires compliance with geometric tolerance limits such as joint gaps and offset between the joint and the tool center point (TCP) of the brazing optic. Variations of the geometrical arrangement for example can result from insufficient clamping, deformations of the substrate material before and during the process and inaccuracies in the process movement. However, these tolerance limits for the brazing process are currently not known.

In this study, the process limits regarding the combination of process velocity, wire feed rate and laser power were investigated for brazing of ZM-coated steel sheets. Regarding an industrial application of the joining process the tolerance limits of the process towards variations of the geometrical arrangement such as joint gaps and TCP-offsets are examined.

2 Experimental setup

For the joining process a prototype brazing optic based on the concept of a conventionally used laser brazing optics ALO4 (Scansonic MI GmbH) was applied [6]. As presented in Fig. 1 the laser beam was positioned in leading position. The wire nozzle and laser beam axis were positioned with an angle of 10° and 30° respectively to the substrate surface normal in process movement direction. The optics was used in combination with a Trumpf TruDisk 12002 disk laser operating at a wavelength of 1030 nm and a spot diameter of 2.4 mm on the substrate surface. CuSi3Mn1 with a diameter of 1.2 mm was used as brazing material and the ZM-coated steel DX56D+100 ZM with a thickness of 0.8 mm served as substrate material. The brazing wire was transported using a DINSE DIX WD 300 wire transporting system. The experiments were carried out using flanged brazing joints with a bending angle of 90° and bending radii of 1.6 mm and 2.0 mm. For every parameter set a minimum of 3 samples was brazed.



Henze 2022

BIAS ID 220478

Fig. 1: Process setup and material

During the experiments suitable process parameter ranges were investigated. Therefore, the relevant process parameters e.g., laser power, wire feed rate and the process velocity, as well as the geometrical arrangement gap width and lateral offset of the TCP were varied. The local amount of melted wire depends on the ratio of the process velocity to the wire feeding rate. Therefore, the wire feeding rate was represented using the wire factor calculated with equation 1, where v_{wire} denotes the wire feeding velocity and $v_{process}$ the process velocity. The continuous complete melting of the wire in the tool center point (TCP) requires a certain amount of energy per unit length of the brazing wire. This energy is characterized by the gross energy for melting further denoted as E_{wire} as shown in equation 2. The applied laser power P_L is adjusted depending on the process velocity and the wire factor to keep the gross energy for melting in a certain range that was proven to ensure a stable wire melting in preceding studies. Therefore, instead of investigating the process window with respect to the laser power, the gross energy for melting was considered. In general, the gross melting energy depends on further parameters such as the wire diameter and the ratio between the wire diameter and the spot diameter. As those parameters were kept constant throughout the investigations presented in this study the equation for the gross melting energy can be simplified as shown in equation 2. Using these derived parameters

instead of the original process parameter enabled a comparison between the results of different parameter fields.

$$D = \frac{v_{wire}}{v_{process}} \quad (1)$$

$$E_{wire} = \frac{P_L}{v_{process} \cdot D} \quad (2)$$

The resulting brazing seams were evaluated based on the visual seam quality which is an indicator for a successful brazing process and important for the industrial applicability in the automotive production. Homogeneous seams with continuous connectivity on both sides of the joint without inaccuracies on top of the surface or on the seam edge, were considered as seams without defect (green dots, e.g. Fig. 3) and therefore applicable seams. The joint quality of the applicable seams was measured using tensile shear strength tests with the tensile testing machine Zwick Roell Z250. The test specimens for the tensile shear strength tests were cut to a width of 45 mm by eroding before testing. The influence of the process velocity and the gross melting energy on the wetting behavior of the defect free seams was evaluated based on metallographic cross sections. Thereby the wetting length and depth were measured as indicator for the wetting quality.

3 Results and discussion

The experiments showed that it is possible to join the ZM-coated steel in flange joint configuration using CuSi3Mn1 as brazing material in a laser brazing process with laser leading configuration. Fig. 2 shows an example for a brazing sample with an according cross section. The seam appearance was homogenous without irritations. The cross sections showed a steady connection of the brazing material with the substrate material without melting the latter.

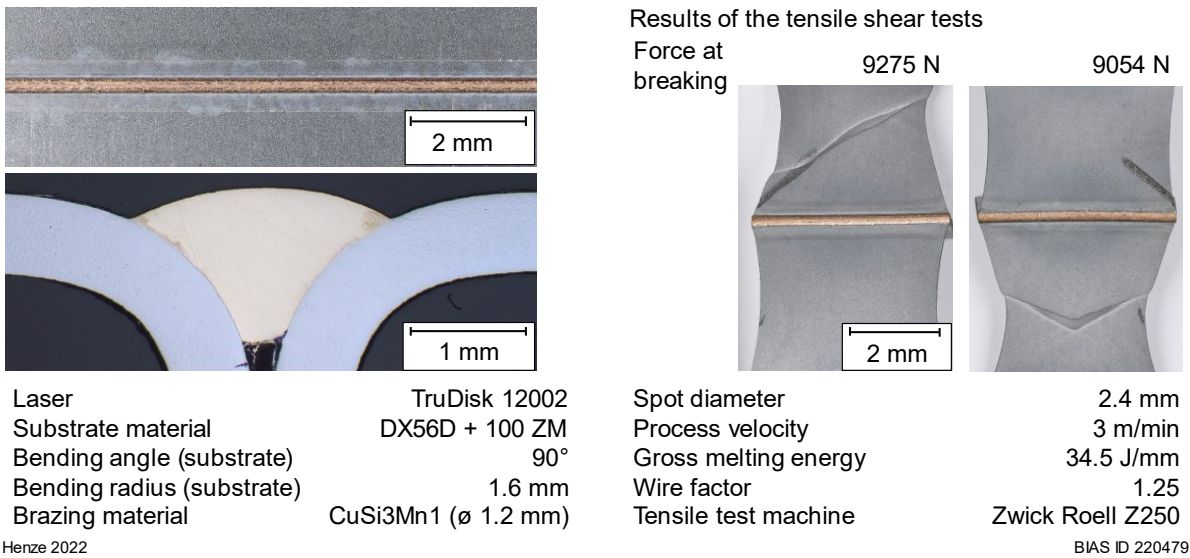


Fig. 2: Example for a brazing sample with the associated cross section and results of the shear strength test

Starting from the realization of a successful brazing process the boundaries of the process were evaluated. The investigations focused especially on the process velocity and the gross melting energy. Fig. 3 shows the dependence of the seam appearance on the process velocity and gross melting energy for flange joints with a bending radius of 1.6 mm. The samples with a bending radius of 2.0 mm showed a similar process window. The process window was limited due to significant defects such as insufficient wetting or balling (red dots) or an increased heat influence on the substrate material (yellow dots). The dots in the diagram represent the number of samples without and with defects for every parameter set. Small gross melting energies resulted in significant defects of the seam due to an insufficient preheating of the substrate material. High gross melting energies increased the intensity of the reflected laser beam on the substrate material which resulted in higher preheating of the substrate material up to an undesirable heat influence. A gross melting energy between 30 J/mm and 40 J/mm resulted in seams without defects or melting of the substrate material. Using a constant gross melting energy of 34.5 J/mm, small process velocities resulted in significant defects as insufficient wetting. Process velocities of at least 2 m/min were necessary. Higher process velocities of up to 6 m/min resulted in seams without defects for gross melting energies between 30 J/mm and 40 J/mm. The process showed a

similar tolerance towards variations of the gross melting energy for process velocities from 2 m/min to 6 m/min.

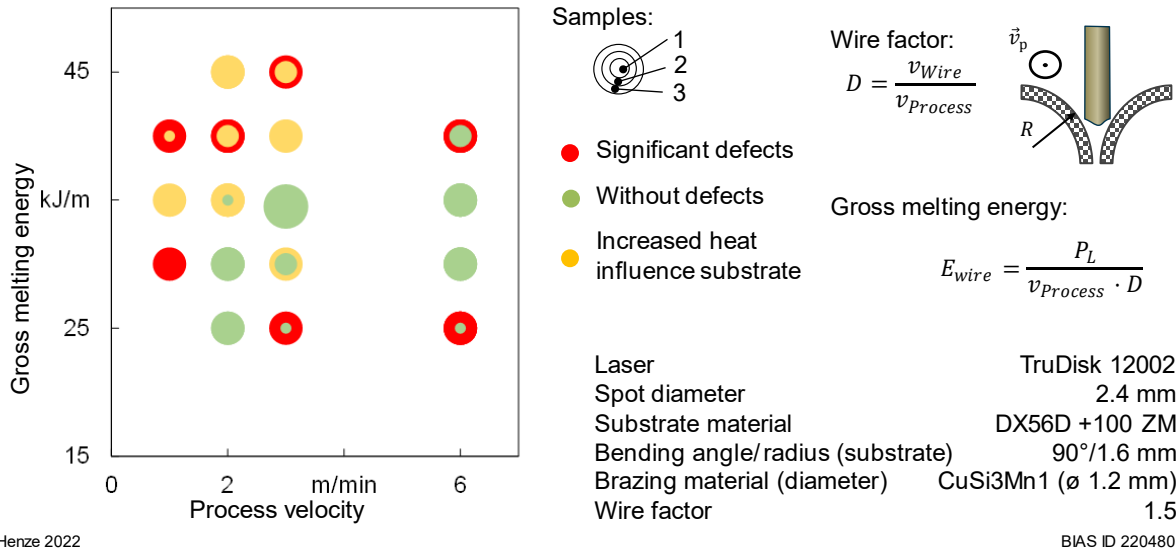


Fig. 3: Influence of the process velocity and specific gross energy for melting on the seam quality in laser brazing in laser leading configuration

To evaluate the influence of the process parameters on the wetting behavior the wetting length and depth were measured using microsections of the samples without visible surface defects. Three samples per parameter combination were examined. Both measurands were measured on the left and right side of each sample and the average value was calculated. Fig. 4 shows the results. The wetting length and depth increased with increasing gross melting energy and process velocity.

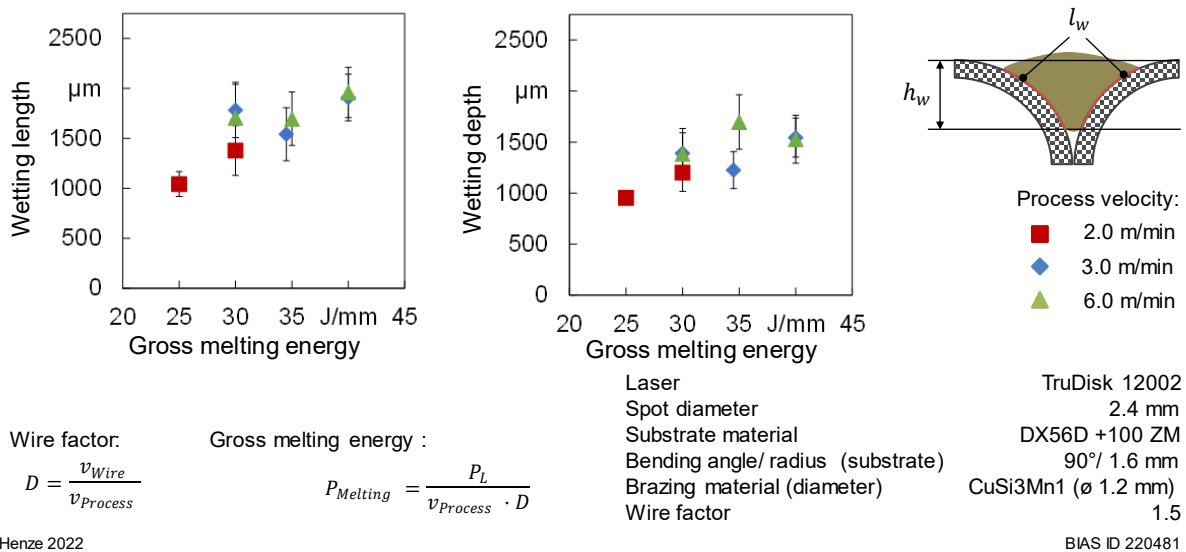


Fig. 4: Measurement of the wetting length and width as a function of the gross melting energy and process velocity

For the investigation of the influence of the joint gap and the lateral displacement a process velocity of 3 m/min and a gross melting energy of 34.5 J/mm were applied based on the previously determined process windows. The results were evaluated regarding the visual seam quality. Fig. 5 shows the results of the variation of the joint gap for flange joints with a bending angle of 90° and a bending radius of 1.6 mm. The samples brazed with the smallest used wire factor of 1 (process velocity = wire velocity) had significant defects for all tested gap widths. This could be related to the small amount of melted brazing material or an insufficient preheating. For the smallest gap width of 0 µm and therefore the “zero”-gap a wire factor of 1.25 was sufficient to join the substrate materials. For higher gap widths the process window was shifted to higher wire factors due to the higher gap bridgeability when feeding increased amounts of melted brazing material to the joint interface (accompanied by a higher preheating). Gap widths of up to 100 µm were joinable. The number of samples with

seam defects increased with the gap width which was associated with a smaller process stability at higher gap widths.

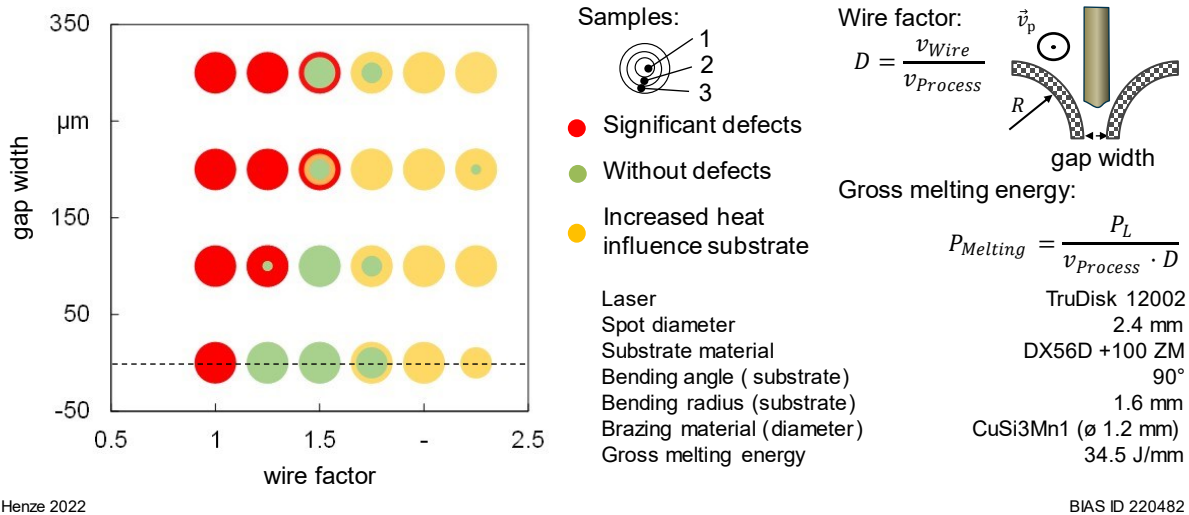


Fig. 5: Influence of the gap width and wire factor onto the visual seam quality

Fig. 6 shows the influence of the lateral offset of the TCP on the visual seam quality. The results show a dependence on the bending radius of the substrate material. For both bending radii tested, lateral offsets of up to 400 µm were allowable. Using smaller bending radii decreased the influence of the lateral offset.

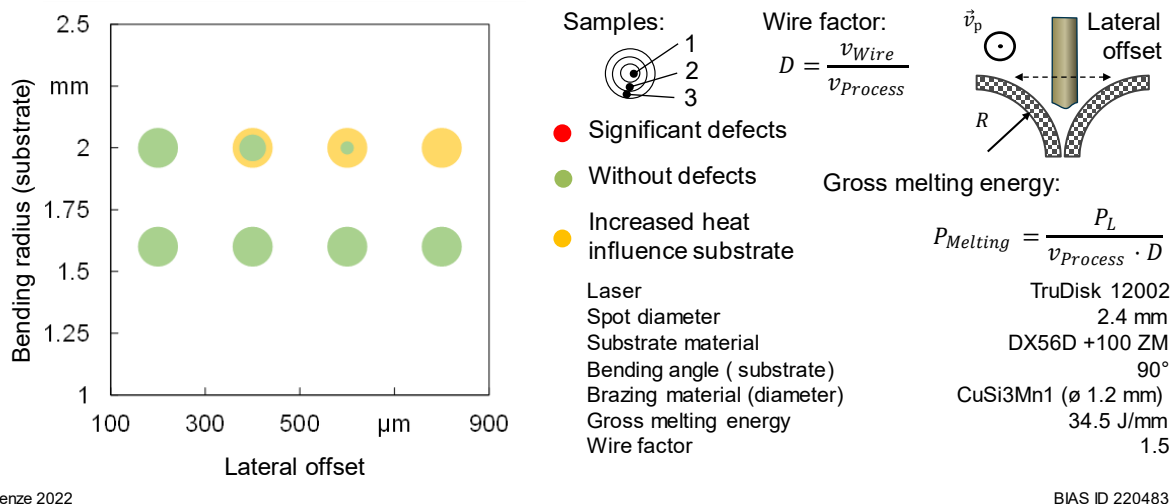


Fig. 6: Influence of the lateral offset depending on the bending radius of the substrate material onto the visual seam quality

The samples of the previously presented results for seams without defects were further investigated in tensile shear tests. The measured tensile shear force at breaking during the tensile shear strength tests for all tested process parameters was mainly between 9,000 N and 10,000 N. The samples broke in the substrate material, or the suspected heat affected zone of the substrate material or as a combination of both. Fig. 2 shows examples for tensile shear strength samples with breaking in the substrate material (right sample) and combined breaking initiated in the suspected heat affected zone of the reflected laser beam on the substrate material (left sample). The measured tensile shear strength was therefore that of the substrate material. The strength of the seam is higher. An influence of the tested process parameter on the tensile shear strength could therefore not be evaluated.

4 Summary

The investigation demonstrated the ability to join ZM-coated steel sheets in flange joint configuration with CuSi3Mn1 as brazing material using a laser brazing process in laser leading configuration without wetting defects. Thereby, process velocities of up to 6 m/min enabled defect free brazing seams. The tolerances of the joining process towards variations of the geometrical arrangement were identified. The process had a tolerance

towards joint gaps of up to 100 μm and towards a lateral displacement of the TCP of up to 400 μm . The tensile shear strength of the brazing seam was higher than the tensile shear strength of the used substrate material.

Acknowledgements

The ZIM-project number ZF 4587002FH9 was funded by the Federal Ministry for Economic Affairs and Energy (BMWi) via the German Federation of Industrial Research Associations (AiF) in accordance with the policy to support the Central Innovations of Medium-Sized Enterprises (ZIM) based on a decision by the German Bundestag. Furthermore, the authors gratefully acknowledge the collaboration with the members of the project affiliated committee regarding the support of knowledge, material and equipment over the course of the research. The “BIAS ID” numbers are part of the figures and allow the retraceability of the results with respect to the mandatory documentation required by the funding organization.

References

- [1] Volovitch P, Allely C, Ogle K (2009) Understanding corrosion via corrosion product characterization: I. Case study of the role of Mg alloying in Zn–Mg coating on steel. *Corrosion Science* 51:1251–1262. <https://doi.org/10.1016/j.corsci.2009.03.005>
- [2] Koltsov A, Bailly N, Cretteur L (2010) Wetting and laser brazing of Zn-coated steel products by Cu–Si filler metal. *J Mater Sci* 45:2118–2125. <https://doi.org/10.1007/s10853-009-3949-y>
- [3] Wachsmuth S, Nothdurft S, Reimann W et al. (2019) Laser brazing of zinc-aluminum-magnesium coated steel–influence of the joint geometry. In: Reisgen U, Zäh M, Schmidt MF et al. (eds) *Proceedings of Lasers in Manufacturing Conference 2019: LiM 2019*
- [4] Gatzen M, Radel T, Thomy C et al. (2016) Wetting and solidification characteristics of aluminium on zinc coated steel in laser welding and brazing. *Journal of Materials Processing Technology* 238:352–360. <https://doi.org/10.1016/j.jmatprotec.2016.07.026>
- [5] Mittelstädt C, Seefeld T, Vollertsen F (2016) Laser beam brazing of hot-dip galvanized thin sheet steel in laser leading process configuration. In: *Laser Institute of America (ed) International Congress on Applications of Lasers & Electro-Optics*. Laser Institute of America, p 1802
- [6] Scansonic MI GmbH (2022) ALO4 – Scansonic | Bearbeitungsoptiken für das Laserschweißen, Laserlöten, Laserhärten, Laserschneiden. <https://www.scansonic.de/products/alo4/>. Accessed 15 Aug 2022

Introducing an algorithm for the automatic detection of interface positions for flange joints based on laser triangulation measurements

Ronald Pordzik*¹ , Thorsten Mattulat¹ 

¹ BIAS – Bremer Institut für angewandte Strahltechnik GmbH, Klagenfurter Straße 5, 28359 Bremen, Germany

Abstract

Laser brazing is a joining technique widely applied in industrial manufacturing such as automotive production. In order to establish a stable brazing process free of defects, it is necessary to support the process with a track control. Whereas conventional laser brazing processes rely on tactile track control based on the mechanical interaction between the brazing wire and the substrate surface, new approaches like the reflection-assisted laser brazing require vision-based detection of the joining interface for track control as the brazing wire is already molten when contacting the substrate surface. Especially in the case of brazing flange joints the visual detection of the interface position is challenging given the limited visual accessibility of the joint interface. Therefore, in order to reliably detect the interface position, a semi-analytic algorithm is introduced based on the signals from a laser triangulation sensor scanning the joint geometry ahead of the process zone. Hereby information about the joint geometry is used to extrapolate the surface contours of the joining partners into areas that are not visible to the sensor. The algorithm was successfully tested on 90° and 45° flange joints resulting in an uncertainty in the determination of the interface position of less than ± 0.5 mm.

Keywords: laser brazing, joint interface detection, track control

1 Introduction

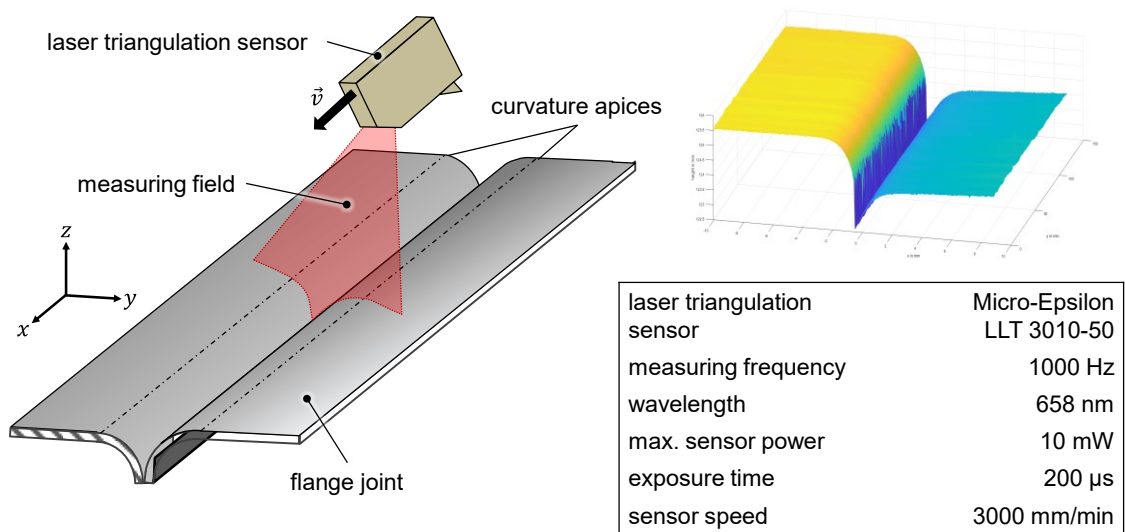
Automatic manufacturing such as welding and brazing is widely applied in nowadays industrial manufacturing and an integral part of industry 4.0. The automatization of processes is based on the programming of the process parameters and the teaching of the process path so that all necessary information for conducting the process is available in advance. The process path itself is determined by the shape of the workpieces. These contours in general are not ideal but rather affected by imperfections during previous machining and heat induced deformations during the automatic process. Therefore, the processing path must be controlled and adjusted during the ongoing process by feedback signals from the workpieces that can be either of visual or tactile quality. While some processes like for example conventional laser brazing processes rely on tactile track control, many other processes like laser welding or the reflection-assisted laser brazing processing approach, first introduced by Mittelstädt et al. [1], require vision-based solutions for determining and correcting the track position. Solutions for vision-based seam identification, detection and tracking were mainly researched in the application of welding processes. Previous research dealt with seam tracking of butt joints or V-grooves. Xue et al. [2] used the greyscale information of a crosshair laser to track the seam of a butt joint in a GTAW-process. Xu et al. [3] utilized the grey scale information of arc welding images by applying an edge detection algorithm on the front region between the melt pool and the seam. Kos et al. [4] calculated the position of a laser beam and the seam in 3D in real-time during laser welding with a camera and an additional illumination laser. Kiddee et al. [5] used a cross mark structured light to analyze the cross-section of a V-groove which was then matched with a template to detect the edges of the V-groove. Fan et al. [6] and Li et al. [7] were able to analyse the welding joint cross-section by a vector of the depth values, which was created by using a stripe laser. The vector of the cross-section then could be assigned to a welding joint type or profile by using the

RBF kernel function or a character string method. An algorithm which used the previous groove cross-section to locate the following one was developed and implanted by Ding et al. [8]. Thus, the seam tracking was not restricted to a certain joint type and could be applied on a free form groove.

While certain joints like for example overlap joints can be detected via rather simple algorithms, more complex joint geometries like flange joints require more sophisticated approaches to reliably detect the track position. Especially the relative position between the joint surfaces and the visual sensor is of crucial importance as it determines the number of blind spots inside the joint interface that are potentially necessary for the exact determination of the interface position. For the task of joint interface detection laser triangulation sensors have been proven as fast and reliable measuring systems [5] without the need for complex calibration while providing high data rates. During this study a semi-analytic approach for the automatized detection of joint interfaces on flange joints has been developed and tested on a set of experimental data of scanned flange joint geometries for validation.

2 Experimental setup

The joint interface profiles were measured with the laser triangulation sensor LLT 3010-50 from the manufacturer Micro-Epsilon operating at a wavelength of 658 nm with a maximum power of 10 mW. The sensor was attached to a robotic arm which was programmed to move linearly and with a constant velocity of 3000 mm/min along the joint interface. The flange joints consisted of ZnMg-coated steel sheets of the type DX56D + 100 ZnMg with an overall thickness of 0.8 mm and a coating thickness of 7 μm . The joints were set up in a clamping device with straight edges so that the joint interface positions in each cross section are expected to be arranged on a straight line. The clamping device also allows for the adjustment of the height difference between both joining partners which affects the accessibility of the joint interface by the sensor. A measuring frequency of 1000 Hz was applied resulting in a spatial resolution of 20 recorded profiles per mm in scanning direction. The exposure time used for scanning the highly reflective ZnMg-coated surfaces of the steel sheets was 200 μs . At this exposure time a sufficient illumination of the surfaces was achieved while the effects of overexposure due to the highly reflective surfaces were minimized. In the lateral direction the applied sensor provides a resolution of 2048 measuring points. At a given measuring distance of 125 mm at the top surface of the flange joint with a lateral scan field of 50 mm this results in a lateral spatial resolution of $\sim 24 \mu\text{m}$. With this setup two different joint geometries, a 90° flange joint with curvature radii of 2.0 mm and a 45° flange joint with radii of also 2.0 mm were scanned. In both configurations a height difference between the joining partners of 1.6 mm was applied and in all following illustrations the left metal sheet was the heightened one. Although the joint was set up in a rigid clamping device and the sensor path was programmed to follow the interface position parallelly, the height signal of the sensor is superimposed by oscillations of the robotic arm, disturbing the measuring signal. The oscillations of the robotic arm become visible in the waviness of the plane sections in the three-dimensional reconstruction of the scans as can be seen in Fig. 1 in the upper right picture.



Pordzik 2022

BIAS ID 220458

Fig. 1: Experimental setup and parameters for scanning flange joint surfaces by means of laser triangulation

3 Algorithm

The algorithm for the flange joint detection via measuring signals of a laser triangulation sensor is based on two crucial assumptions:

1. The curvatures on both sides of the flange joint can be reliably approximated by circular functions.
2. The curvature of the flange joints on both sides is preceded by an even section of arbitrary extent that serves as starting point of the calculation.

In the first step a linear regression is performed on the even sections on both sides of the flange joint starting with an initial number of points. The area of linear regression is extended iteratively on both ends of the even section until the coefficient of determination (CoD) further denoted a D surpasses a threshold defined by the CoD of the initial sample size N_{ini} following equation 1.

$$D_{thresh} = 2 \cdot D_{ini} \quad (1)$$

The measuring point of the laser triangulation sensor on the side of the joint interface that first surpasses the CoD threshold defines the apex of the adjacent curvature. In an analogous manner to the regression of the even section, a circular regression is performed on the curvature starting from the apex with an initial sample size of 50 measuring points.

The circular regression must fulfill the two conditions at the apex stating that itself as well as its derivative must exhibit a continuous transition with the preceding linear section.

$$z(y = y_0) = z_0 \quad (2)$$

$$\frac{dz}{dy} \Big|_{y=y_0} = s_i = \tan(\gamma_i) \quad (3)$$

Given these two conditions the number of parameters in the regression is reduced from three to just one parameter. As the number of measuring points on the curvature is rather big compared to the number of parameters that are to be determined during the regression the resulting system of linear equations, as expressed in equation 4, is highly overdetermined and solved with regard to minimizing the CoD.

$$R \cdot [s \cdot (\mathbf{y} - y_0) - (z - z_0)] = \pm \frac{\sqrt{1+s^2}}{2} \cdot [(\mathbf{y} - y_0)^2 + (z - z_0)^2] \quad (4)$$

$$y_c = y_0 \mp \frac{R}{\sqrt{1+s^2}} \quad z_c = z_0 \mp \frac{R}{\sqrt{1+s^2}} \quad (5)$$

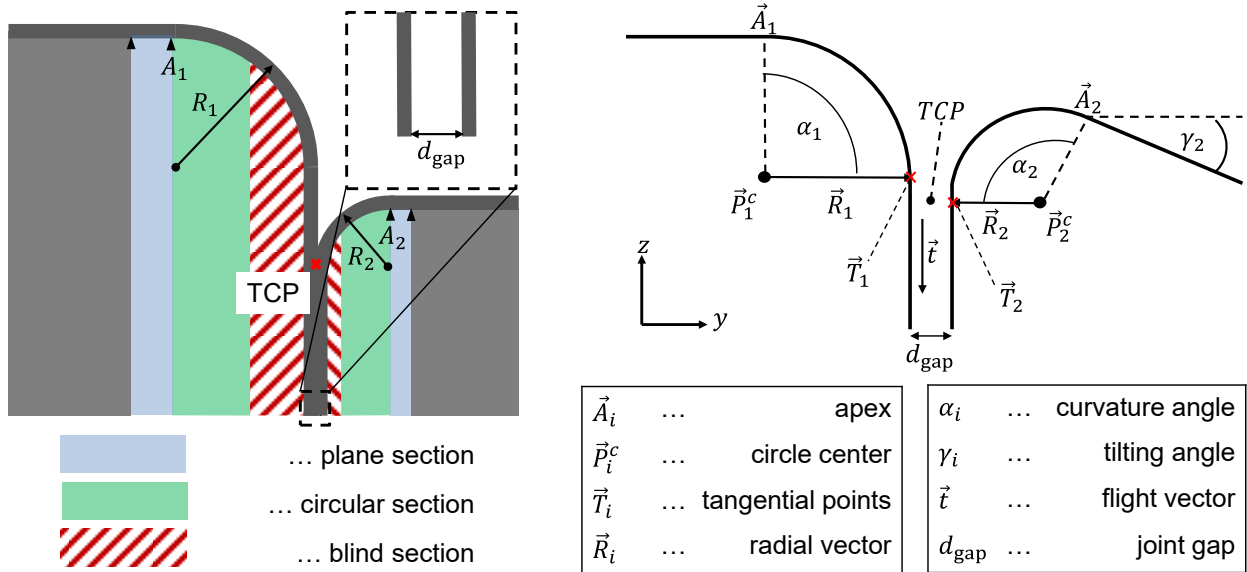


Fig. 2: Schematic of the analysis sections of the joint interface (left) and the relevant geometric properties (right)

In equation 4 the parameter s denotes the slope of the respective plane section with $s_i = \tan(\gamma_i)$ and $[y_0, z_0]$ represent the 2-D coordinates of the curvature's apices. In the same manner as for the even sections the regression terminates when its CoD surpasses the threshold defined based on the initial sample of measuring points. Also, an overlap between the regions of circular regression of both sides of the joint is forbidden. By performing two regressions on each side of the flange joint the most important geometric features are determined namely the radii of the curvatures on both sides denoted by R_i as well as their respective center points \vec{P}_i^0 and the tilting of the whole geometry γ_i as shown in the schematic sketch from Fig. 2. The shape of the joint is required as an input parameter so that the extrapolation of the joint geometry into the concealed areas can be performed. The curvatures are extended to the required angle and prolonged tangentially from there on.

$$d_{\text{gap}} = \left| \frac{(\vec{T}_1 - \vec{T}_2) \cdot \vec{R}_1}{R_1} \right| \quad (6)$$

Now it is possible to calculate the minimum distance d_{gap} between both joining partners according to equation 6. The point where the gap at the joint interface reaches its minimum for the first time starting from the outer edges of the recorded profile is defined as the TCP, that serves as the target value for any track control that is based on this joint detection algorithm.

$$TCP = \vec{T}_i + \vec{R}_i \cdot \frac{d_{\text{gap}}}{2R_i} \quad (7)$$

The recorded three-dimensional profile of the joint geometry is constituted out of several two-dimensional profiles representing the cross-sections perpendicular to the moving direction of the sensor along the work-piece. The TCP can therefore be calculated for each one of these two-dimensional profiles.

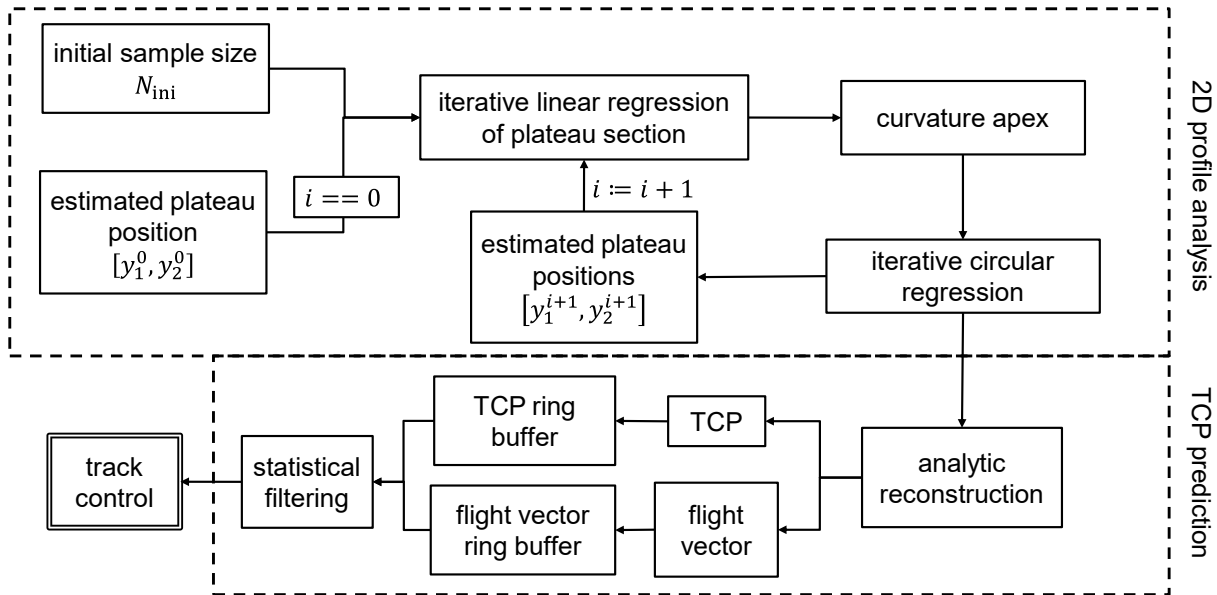
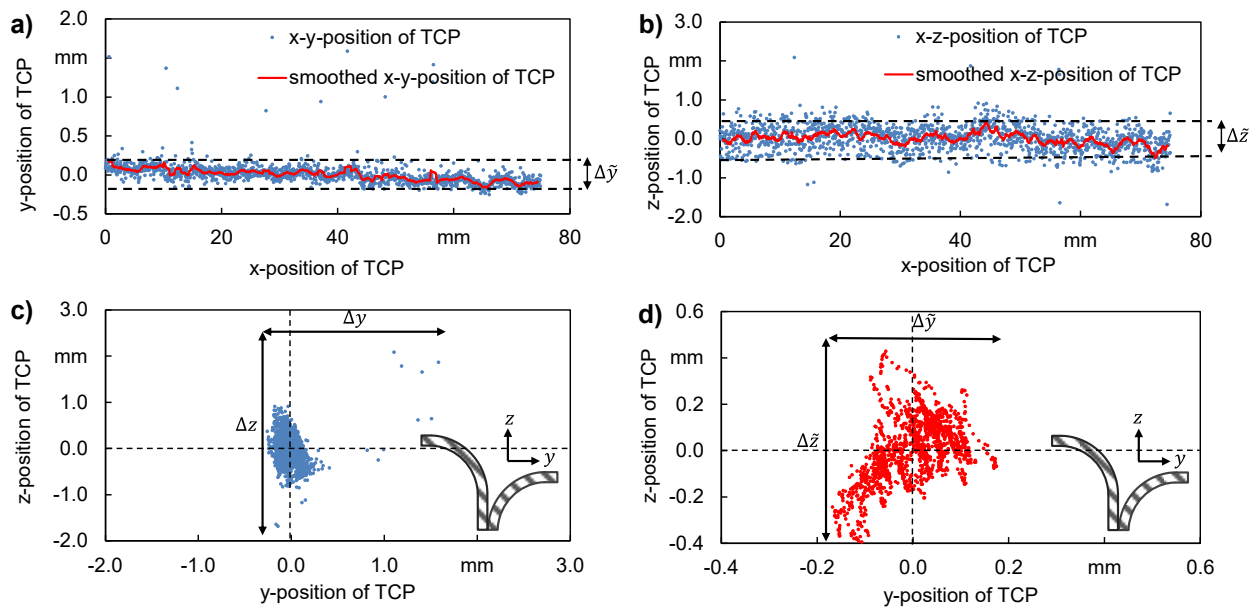


Fig. 3: Block diagram of the two-phased track control algorithm consisting of joint interface detection and TCP prediction

The measurements of the flange joint surfaces are affected by the surrounding conditions as well as the condition of the reflective surface of the metal sheets and the relative position between the sensor and the surface to be measured. Therefore, not every single measured profile will provide a valid result for the TCP when it is calculated by the algorithm described above and rather must be evaluated statistically in the context with neighboring 2-D profiles. This implies that, in order to ensure the algorithm to return reliable values for the TCP, a certain number of profiles has to be recorded in advance to filter out corrupted measurements. Furthermore, the initial guess for the position of the even sections is based on the previous profiles as the shape of joint geometry along the track is expected to change in a continuous manner. The overall structure of the algorithm for joint interface detection and TCP calculation is schematically summarized in Fig. 3.

4 Results and discussion

The algorithm described in chapter 3 was applied to the scans of the two flange joint configurations described in chapter 2. The results give the y- and z-coordinates of the TCP at each profile or x-position respectively. As already mentioned, the TCPs of each cross-sectional profile are expected to be arranged on a straight line based on the construction of the clamping device. The accuracy of the algorithm is therefore characterized based on the deviations of the y- and z-coordinates of the TCP throughout the whole scanning process. The reliability of the laser triangulation sensor is limited so that not every recorded profile necessarily represents an accurate scan of the real flange joint surface. This can be for example due to overexposure of the sensor at some positions or due to signal disturbances by process emissions in case of real welding or brazing processes. To account for these influences on the measurement quality for a stable application in track control the TCP-coordinates determined for each measured profile need to be filtered. A gliding window function with a width of 20 profile scans or time steps respectively was applied to smoothen the TCP-positions. The results for the 90° flange joint are shown in Fig. 4. While, due to outliers, the accuracy based on the unfiltered TCP-positions is rather low with values of $\Delta y = \pm 1.6$ mm and $\Delta z = \pm 2$ mm, the accuracy of the smoothed TCP-positions lies in the range of $\Delta \tilde{y} = \pm 0.2$ mm and $\Delta \tilde{z} = \pm 0.4$ mm.

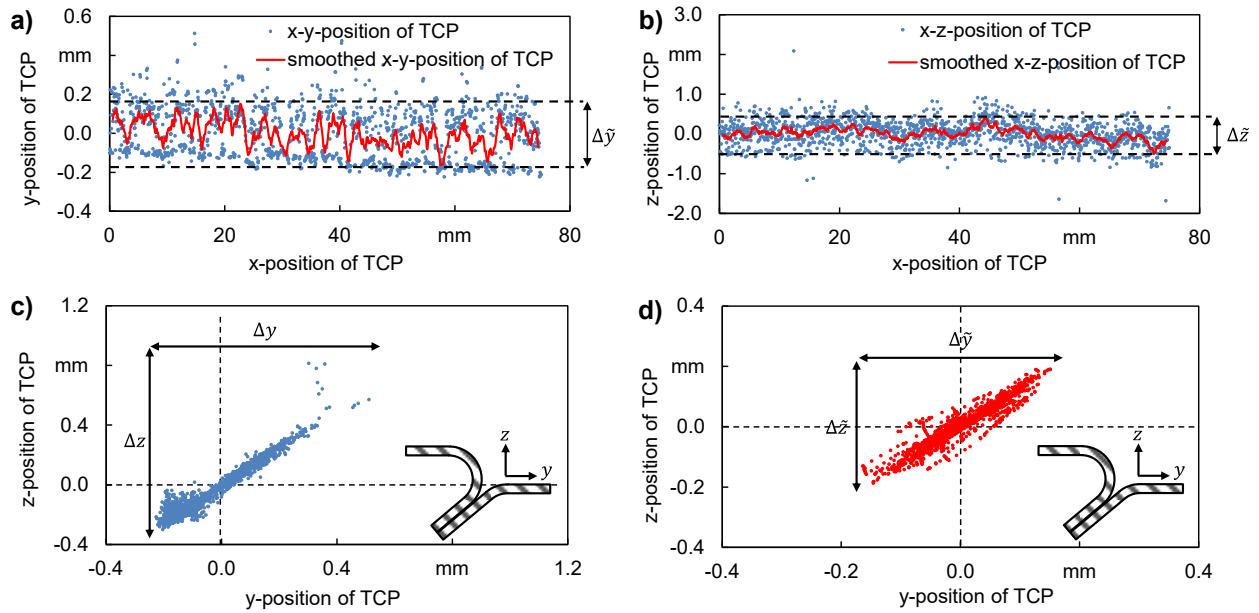


Pordzik 2022

BIAS ID 220461

Fig. 4: Results of joint interface analysis and accuracy of the interface position for the 90° flange joint: a) Scattering in the x-y-plane with and without filtering; b) Scattering in the x-z-plane with and without filtering; c) Scattering of the unfiltered interface positions in the y-z-plane; d) Scattering of the filtered interface positions in the y-z-plane

For the 45° flange joint overall higher accuracies were achieved with fewer statistical outliers diminishing the accuracy of the unfiltered TCP-positions which lie in the range of $\Delta y = \pm 0.5$ mm and $\Delta z = \pm 0.8$ mm respectively. After filtering the accuracies for the smoothed TCP-positions resulted in values of $\Delta \tilde{y} = \pm 0.2$ mm and $\Delta \tilde{z} = \pm 0.2$ mm. The corresponding results are shown in Fig. 5.

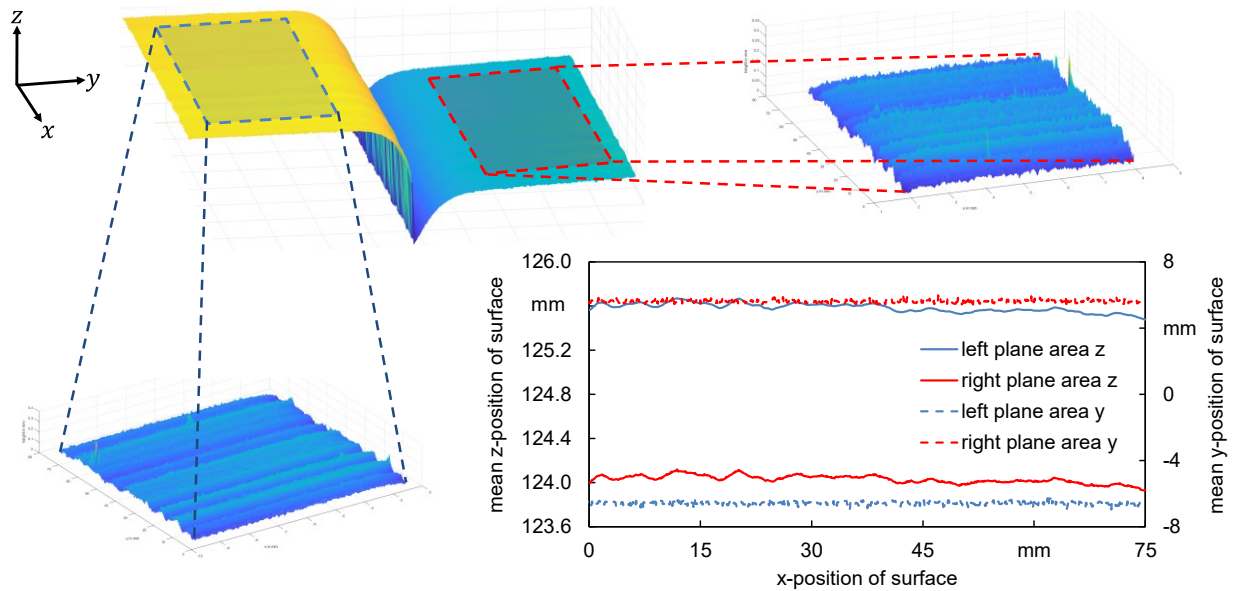


Pordzik 2022

BIAS ID 220462

Fig. 5: Results of joint interface analysis and accuracy of the interface position for the 45° flange joint: a) Scattering in the x-y-plane with and without filtering; b) Scattering in the x-z-plane with and without filtering; c) Scattering of the unfiltered interface positions in the y-z-plane; d) Scattering of the filtered interface positions in the y-z-plane

The achieved accuracies for the smoothed TCP-position are sufficient for implementation in track control of processes like reflection-assisted laser beam brazing according to the process characterization by Henze et al. [9]. Nonetheless, the oscillations of the robotic arm and therefore the position of the laser triangulation sensor must be considered in the evaluation of the presented results. To account for these oscillations superimposed on the linear track of the sensor, the scans of the plane sections on both sides of the joint interfaces were analyzed regarding their fluctuations as depicted within Fig. 6.



Pordzik 2022

BIAS ID 220463

Fig. 6: Characterization of oscillations in the sensor track

The analysis of the track oscillations yields values of ± 0.1 mm for the deviations from the center positions. As superpositions of track oscillations and algorithmic accuracy can lead to both amplification and attenuation of the resulting TCP-positions the resulting accuracy of the algorithms should improve by the value of the track oscillations.

5 Summary and outlook

A semi-analytic algorithm for detecting the interface positions of flange joints and adjusting the TCP has been derived and tested on experimental data. The experimental data consisted of scans of 90° and 45° flange joints recorded by a laser triangulation sensor. The joints were set up in a clamping device with straight edges, thus the joint interface positions would be arranged on a straight line which is important in order to obtain a reference for the measured interface positions. The analysis of the recorded scans resulted in fluctuations of ± 2 mm for the unfiltered positions of the 90° flange joint and fluctuations of ± 0.8 mm for those of the 45° flange joints. Smoothing the TCP-positions with a gliding window function and therefore reducing the effect of outliers representing corrupted measurements, much lower fluctuations of the TCP-position in the range of ± 0.5 mm could be achieved for both types of joints. An analysis of the accuracy of the sensor track showed that the motion of the robotic arm is oscillating with an amplitude of ~ 0.1 mm around its defined center position, therefore negatively affecting the determined accuracy of the algorithm. By that the calculated accuracies of the determination of the joint interface positions must be regarded as upper limits.

Further tests of the algorithm on extended data sets are required to evaluate the potential of the algorithm for application in track control. For example, investigating the influence of lateral inclination between the sensor and the joint interface with a resulting increased blind area is necessary to assess the applicability of the method. Despite the experimental qualification of the algorithm the runtime and efficiency need to be improved to make the algorithm a suitable option for real-time track control. Yet the presented algorithm shows an accuracy in the detection of the joint interfaces sufficiently high for application in reflection-assisted laser brazing processes and therefore can be considered as a promising approach for vision-based track control for flange joint interfaces.

Acknowledgements

The ZIM-project number ZF 4587002FH9 was funded by the Federal Ministry for Economic Affairs and Energy (BMWi) via the German Federation of Industrial Research Associations (AiF) in accordance with the policy to support the Central Innovations of Medium-Sized Enterprises (ZIM) based on a decision by the German Bundestag. Furthermore, the authors gratefully acknowledge the collaboration with the members of the project affiliated committee regarding the support of knowledge, material and equipment over the course of the research. The “BIAS ID” numbers are part of the figures and allow the retraceability of the results with respect to the mandatory documentation required by the funding organization.

References

- [1] C. Mittelstädt, T. Seefeld, F. Vollertsen: Laser beam brazing of hot-dip galvanized thin sheet steel in laser leading process configuration. *International Congress on Applications of Lasers & Electro-Optics* (2016) 1802
- [2] B. Xue, B. Chang, G. Peng, Y. Gao, Z. Tian, D. Du, G. Wang: A Vision Based Detection Method for Narrow Butt Joints and a Robotic Seam Tracking. *Sensors* 19 (2019)
- [3] Y. Xu, G. Fang, N. Lv, S. Chen, J. Zou: Computer vision technology for seam tracking in robotic GTAW and GMAW. *Robotics and Computer-Integrated Manufacturing* 32 (2015) 25-36
- [4] M. Kos, E. Arko, H. Kosler, M. Jezeršek: Remote-laser welding system with in-line adaptive 3D seam tracking and power control. *Procedia CIRP* 81 (2019) 1189-1194
- [5] P. Kiddee, Z. Fang, M. Tan: An automated weld seam tracking system for thick plate using cross mark structured light. *The International Journal of Advanced Manufacturing Technology* 87 (2016) 3589-3603
- [6] J. Fan, F. Jing, Z. Fang, M. Tan: Automatic recognition system of welding seam type based on SVM method. *The International Journal of Advanced Manufacturing Technology* 92 (2017) 989-999
- [7] X. Li, X. Li, S. Ge, M. Khyam, C. Luo: Automatic Welding Seam Tracking and Identification. *IEEE Transactions on Industrial Electronics* 64 (2017) 7261-7271
- [8] Y. Ding, W. Huang, R. Kovacevic: An on-line shape-matching weld seam tracking system. *Robotics and Computer-Integrated Manufacturing* 42 (2016) 103-112
- [9] I. Henze, R. Pordzik, P. Marben, T. Mattulat: Industrial applicability of reflection-assisted laser beam brazing of ZnMg-coated steel sheets. *Proceedings of the 12th Laser Applications Forum* (2022)

Reihe Strahltechnik im BIAS Verlag

Bisher erschienen:

Herausgegeben von Frank Vollertsen, Ralf Bergmann

Sandro Eckert

Laser-Induced Thermochemical Polishing of Metals

Strahltechnik Bd.75, Bremen, 2022, ISBN 978-3-933762-69-6

Tobias Valentino

Nutzung laserinduzierter Stoßwellen zur Hochdurchsatz Werkstoffprüfung

Strahltechnik Bd. 74, Bremen, 2021, ISBN 978-3-933762-68-9

Hannes Freiße

Hartpartikelverstärkte Oberfläche für das Trockentiefziehen eines hochlegierten Stahls

Strahltechnik Bd. 72, Bremen, 2020, ISBN 978-3-933762-66-5

Markus Prieske

Eignung von CVD-Diamantschichten für die Trockenumformung von Aluminium

Strahltechnik Bd. 71, Bremen, 2020, ISBN 978-3-933762-65-8

Hamza Messaoudi

Thermal conditions for laser chemical micro processing of metals

Strahltechnik Band 70, Bremen 2020, ISBN 978-3-933762-64-1

Tim Radel

Laserstrahlschweißen von Aluminiumlegierungen mit Schwingungsüberlagerung

Strahltechnik Band 69, Bremen 2020, ISBN 978-3-933762-63-4

Silke Huferath-von Lüpke

Produktionsbegleitende Messeinrichtung basierend auf digitaler Holografie

Strahltechnik Band 68, Bremen 2019, ISBN 978-3-933762-62-7

Salar Mehrafsun

Dynamisches Prozessverhalten bei der laserinduzierten thermochemischen Mikrostrukturierung von Metallen

Strahltechnik Band 67, Bremen 2018, ISBN 978-3-933762-61-0

Vijay V. Parsi Sreenivas

Material modifications due to nonlinear effects created by multiphoton absorption in single crystalline silicon

Strahltechnik Band 66, Bremen 2017, ISBN 978-3-933762-60-3

Peer Woizeschke

Eigenschaften laserstrahlgefügter Mischverbindungen aus Aluminium und Titan in Abhängigkeit der Kantengeometrie und Halbzeugstruktur

Strahltechnik Band 65, Bremen 2017, ISBN 978-3-933762-59-7

Henry Köhler

Schwingfestigkeit laserauftragsgeschweißter legierter Stähle

Strahltechnik Band 64, Bremen 2017, ISBN 978-3-933762-58-0

Jörg Volpp

Dynamik und Stabilität der Dampfkapillare beim Laserstrahl-tiefschweißen

Strahltechnik Band 63, Bremen 2017, ISBN 978-3-933762-57-3

Colin Dankwart

High resolution of wave fields from measurements with unknown sensor positions and unknown phase shifts of the object wave

Strahltechnik Band 61, Bremen 2017, ISBN 978-3-933762-55-9

Edwin N. Kamau

Dynamic wave field synthesis: enabling the generation of field distributions with a large space-bandwidth product

Strahltechnik Band 60, Bremen 2016, ISBN 978-3-933762-54-2

Felix Möller

Wechselwirkung zwischen Lichtbogen und Laserstrahl beim Fügen von Aluminium

Strahltechnik Band 59, Bremen 2016, ISBN 978-3-933762-53-3

Simon Kibben

UV-laserbasierte Oberflächenfluorierung von Polymeren

Strahltechnik Band 58, Bremen 2016, ISBN 978-3-933762-52-8

Heiko Brüning

Prozesscharakteristiken des thermischen Stoffanhäufens in der Mikrofertigung

Strahltechnik Band 57, Bremen 2017, ISBN 978-3-933762-51-1

Michael Schwander

Lokale Diamantsynthese durch einen laserbasierten atmosphärischen CVD-PVD-Prozess

Strahltechnik Band 56, Bremen 2016, ISBN 978-3-933762-50-4

Marius Gatzen

Durchmischung beim Laserstrahl-tiefschweißen unter dem Einfluss niederfrequenter Magnetfelder

Strahltechnik Band 55, Bremen 2015, ISBN 978-3-933762-49-8

Frank Vollertsen, Hendrik Tetzl (Hrsg.)

Thermal Forming and Welding Distortion, Proceedings of the IWOTE'14

Strahltechnik Band 54, Bremen 2014, ISBN 978-3-933762-48-1

Zhuo Tang

Heißrissvermeidung beim Schweißen von Aluminiumlegierungen mit einem Scheibenlaser

Strahltechnik Band 53, Bremen 2014, ISBN 978-3-933762-47-4

Martin Grden

Simulation thermischen Biegens mittels Gebietszerlegung

Strahltechnik Band 52, Bremen 2014, ISBN 978-3-933762-46-7

Jens Sakkietitbutra

Modellierung thermisch bedingter Formänderungen und Eigenspannungen von Stählen zum Aufbau von geregelten Prozessen

Strahltechnik Band 51, Bremen 2013, ISBN 978-3-933762-45-0

Frank Buschenhenke

Prozesskettenübergreifende Verzugsbeherrschung beim Laserstrahlschweißen am Beispiel einer Welle-Nabe-Verbindung

Strahltechnik Band 50, Bremen 2013, ISBN 978-3-933762-44-3

Daniel Reitemeyer

Stabilisierung der Fokusslage beim Schweißen mit Faser- und Scheibenlasern

Strahltechnik Band 49, Bremen 2013, ISBN 978-3-933762-43-6

Steffen Neumann

Einflussanalyse beim single mode Faserlaserschweißen zur Vermeidung des Humping-Phänomens

Strahltechnik Band 48, Bremen 2012, ISBN 978-3-933762-42-9

Mostafa Agour

Determination of the complex amplitude of monochromatic light from a set of intensity observations

Strahltechnik Band 47, Bremen 2011, ISBN 978-3-933762-41-2

Andreas Stephen

Elektrochemisches Laser-Jet-Verfahren zur Mikrostrukturierung von Metallen

Strahltechnik Band 46, Bremen 2011, ISBN 978-3-933762-40-5

Michael Koerdt

Herstellung von integriert-optischen Sensorstrukturen in Polymersubstraten basierend auf Brechzahländerungen durch ultraviolette Laserstrahlung

Strahltechnik Band 45, Bremen 2011, ISBN 978-3-933762-39-9

Hanna Wielage

Hochgeschwindigkeitsumformen durch laserinduzierte Schockwellen

Strahltechnik Band 44, Bremen 2011, ISBN 978-3-933762-38-2

Claus Thomy

Dynamisches Prozessverhalten beim Laserstrahl-MSG-Hybridschweißen

Strahltechnik Band 43, Bremen 2011, ISBN 978-3-933762-37-5

Thomas Seefeld

Laser-Randschichtschmelzen mit erhöhter Prozessgeschwindigkeit am Beispiel von Aluminium-Zylinderlaufbahnen

Strahltechnik Band 42, Bremen 2011, ISBN 978-3-933762-36-8

Frank Vollertsen (Hrsg.)

Thermal Forming and Welding Distortion

Strahltechnik Band 41, Bremen 2011, ISBN 978-3-933762-35-1

Frank Vollertsen, Daniel Reitemeyer (Hrsg.)

Laserstrahlfügen: Prozesse, Systeme, Anwendungen, Trends

Strahltechnik Band 40, Bremen 2010, ISBN 978-3-933762-34-4

Claas Falldorf

Bestimmung der komplexwertigen Amplitude von Wellenfeldern auf Basis des Prinzips der Selbstreferenz

Strahltechnik Band 39, Bremen 2010, ISBN 978-3-933762-33-7

Marc Baumeister

Dynamische Laser-Mikroperforation mit single-mode Faserlaser

Strahltechnik Band 38, Bremen 2009, ISBN 978-3-933762-31-3

Zhenyu Hu

Analyse des tribologischen Größeneffekts beim Blechumformen

Strahltechnik Band 37, Bremen 2009, ISBN 978-3-933762-30-6

Frank Vollertsen, Thomas Seefeld (Eds.)
Laserbearbeitung: Prozesse, Systeme, Anwendungen, Trends
Strahltechnik Band 36, Bremen 2008, ISBN 978-3-933762-28-3

Torsten Baumbach
Untersuchungen zur vergleichenden, digitalen Holografie mit aktiver Wellenfrontmodifikation
Strahltechnik Band 35, Bremen 2008, ISBN 978-3-933762-27-6

Knut Partes
Hochgeschwindigkeitsbeschichten mit dem Laserstrahl
Strahltechnik Band 34, Bremen 2008, ISBN 978-3-933762-26-9

Hendrik Schulze Niehoff
Entwicklung einer hochdynamischen, zweifachwirkenden Mikroumformpresse
Strahltechnik Band 33, Bremen 2008, ISBN 978-3-933762-25-2

Thorsten Bothe
Grundlegende Untersuchungen zur Formerfassung mit einem neuartigen Prinzip der Streifenprojektion und Realisierung in einer kompakten 3D-Kamera
Strahltechnik Band 32, Bremen 2008, ISBN 978-3-933762-24-5

Frank Vollertsen, Jens Sakkietitubtra (Hrsg.)
Thermal Forming and Welding Distortion
Strahltechnik Band 31, Bremen 2008, ISBN 978-3-933762-23-8

Herausgegeben von Frank Vollertsen

Michael Kreimeyer
Verfahrenstechnische Voraussetzungen zur Integration von Aluminium-Stahl-Mischbauweisen in den Kraftfahrzeugbau
Strahltechnik Band 30, Bremen 2007, ISBN 978-3-933762-20-7

Carsten Wochnowski
UV-laser-basierte Erzeugung von planaren, polymeren Bragg-Multiplexer-Strukturen
Strahltechnik Band 29, Bremen 2007, ISBN 978-3-933762-19-1

Herausgegeben von Frank Vollertsen, Werner Jüptner

Frank Vollertsen, Thomas Seefeld (Hrsg.)
Laserstrahlfügen: Prozesse, Systeme, Anwendungen, Trends
Strahltechnik Band 28, Bremen 2006, ISBN 978-3-933762-18-4

Frank Vollertsen (Hrsg.)
Prozessskalierung
Strahltechnik Band 27, Bremen 2005, ISBN 978-3-933762-17-7

Frank Vollertsen, Thomas Seefeld (Hrsg.)
Thermal Forming
Strahltechnik Band 26, Bremen 2005, ISBN 978-3-933762-16-0

Volker Kebbel

Untersuchung zur Erzeugung und Propagation ultrakurzer optischer Bessel-Impulse

Strahltechnik Band 25, Bremen 2004, ISBN 978-3-933762-15-3

Frank Vollertsen, Ferdinand Hollmann (Ed.)

Process Scaling

Strahltechnik Band 24, Bremen 2003, ISBN 978-3-933762-14-6

Emil Schubert

Untersuchungen zum Leichtbau mit Hilfe lasergestützter Mischbauweise

Strahltechnik Band 23, Bremen 2003, ISBN 978-3-933762-13-9

Christoph von Kopylow

Durchstimmbare Mikrokristall-Laser für die absolute Distanzinterferometrie

Strahltechnik Band 22, Bremen 2003, ISBN 978-3-933762-12-2

Carmen Theiler

Aufbau gradierter Nickelbasis-Chromkarbid-Verbundwerkstoffe durch Laserstrahlpulverbeschichten

Strahltechnik Band 21, Bremen 2003, ISBN 978-3-933762-11-5

Herausgegeben von Gerd Sepold, Werner Jüptner

Thomas Kreis (Hrsg.)

Werkzeug Laser – Industrieller Fortschritt durch wissenschaftliche Forschung

Strahltechnik Band 20, Bremen 2002, ISBN 978-3-933762-10-8

Gerd Sepold, Thomas Seefeld (Hrsg.)

Laserstrahlfügen: Prozesse, Systeme, Anwendungen, Trends

Strahltechnik Band 19, Bremen 2002, ISBN 978-3-933762-09-2

Gerd Sepold, Florian Wagner, Jürgen Tobolski

Kurzzeitmetallurgie

Strahltechnik Band 18, Bremen 2002, ISBN 978-3-933762-08-5 (vergriffen)

Frank Elandaloussi

Modellgestützte Detektion und Analyse von Materialfehlern an technischen Objekten

nach dem Prinzip „Erkennung durch Synthese“

Strahltechnik Band 17, Bremen 2002, ISBN 978-3-933762-07-8

Ingo Zerner

Prozessstabilisierung und Ergebnisse für das Laserstrahlfügen von Aluminium-Stahl-Verbindungen

Strahltechnik Band 16, Bremen 2001, ISBN 978-3-933762-05-4

Daniel Holstein

Ortsaufgelöste Charakterisierung von mechanischen Eigenschaften

laserstrahlgeschweißter Verbindungen

Strahltechnik Band 15, Bremen 2001, ISBN 978-3-933762-04-7

Bernd Grubert

Untersuchung neuartiger Resonatorkonzepte für koaxiale Wellenleiterlaser

Strahltechnik Band 14, Bremen 2001, ISBN 978-3-933762-03-0

Martin Klassen

Prozessdynamik und resultierende Prozessinstabilitäten beim Laserstrahlschweißen von Aluminiumlegierungen

Strahltechnik Band 13, Bremen 2000, ISBN 978-3-933762-02-3

Ingo Engler

Verfahrenskombination Laserstrahlschweißen und -richten am Beispiel einer Titan-Leichtbaustruktur

Strahltechnik Band 12, Bremen 1999, ISBN 978-3-933762-01-6

Ulrike Mieth

Erscheinungsbild von Materialfehlern in holografischen Interferogrammen

Strahltechnik Band 11, Bremen 1998, ISBN 978-3-933762-00-9

Werner Jüptner (Hrsg.)

Laser von der Wissenschaft zur Anwendung

Strahltechnik Band 10, Bremen 1997, ISBN 978-3-9805011-4-9

Peter Andrä

Ein verallgemeinertes Geometriemodell für das Streifenprojektionsverfahren zur optischen 3D-Koordinatenmessung

Strahltechnik Band 9, Bremen 1998, ISBN 978-3-9805011-9-4

Thomas Franz

Laserstrahlschweißen mit Nd:YAG-Laser unter Wasser

Strahltechnik Band 8, Bremen 1998, ISBN 978-3-9805011-8-7

Sigurd Weise

Heißrissbildung beim Laserstrahlschweißen von Baustählen

Strahltechnik Band 7, Bremen 1998, ISBN 978-3-9805011-7-0

Gerd Sepold, Manfred Geiger (Hrsg.)

Strahl-Stoff-Wechselwirkung bei der Laserstrahlbearbeitung 2

Strahltechnik Band 6, Bremen 1998, ISBN 978-3-9805011-6-3

Werner Jüptner, Gerd Sepold (Hrsg.)

Lasermaterialbearbeitung im Transportwesen

Strahltechnik Band 5, Bremen 1997, ISBN 978-3-9805011-5-6

Carolin Renate Radscheit

Laserstrahlfügen von Aluminium mit Stahl

Strahltechnik Band 4, Bremen 1997, ISBN 978-9805011-3-2

Jürgen Breuer

UV-lasergestütztes Vorbehandlungsverfahren zur gezielten Modifizierung der Oberflächen von Polypropylen

Strahltechnik Band 3, Bremen 1996, ISBN 978-3-9805011-2-5

Bernd Heidenreich

Beitrag zum Laserstrahlbrennschneiden von großen Stahlblechen

Strahltechnik Band 2, Bremen 1995, ISBN 978-3-9805011-1-8

Christian Binroth

Beitrag zur Prozessstabilität beim CO₂-Laserstrahlschweißen von Aluminium mit Zusatzwerkstoffen

Strahltechnik Band 1, Bremen 1995, ISBN 978-3-9805011-0-1